OPTIMAL RAILROAD RAIL GRINDING FOR FATIGUE MITIGATION

A Dissertation

by

POTCHARA TANGTRAGULWONG

Submitted to the Office of Graduate Studies of
Texas A&M University
in partial fulfillment of the requirements for the degree of

DOCTOR OF PHILOSOPHY

December 2010

Major Subject: Civil Engineering

Optimal Railroad Rail Grinding For Fatigue Mitigation

OPTIMAL RAILROAD RAIL GRINDING FOR FATIGUE MITIGATION

A Dissertation

by

POTCHARA TANGTRAGULWONG

Submitted to the Office of Graduate Studies of
Texas A&M University
in partial fulfillment of the requirements for the degree of

DOCTOR OF PHILOSOPHY

Approved by:

Chair of Committee,	Gary T. Fry
Committee Members,	Harry L. Jones
	Stefan Hurlebaus
	Terry S. Creasy
Head of Department,	John M. Niedzwecki

December 2010

Major Subject: Civil Engineering

ABSTRACT

Optimal Railroad Rail Grinding for Fatigue Mitigation. (December 2010)

Potchara Tangtragulwong, B.Eng., Chulalongkorn University;

M.En., Texas A&M University

Chair of Advisory Committee: Dr. Gary T. Fry

This dissertation aims to study the benefit of rail grinding on service life of railroad rails, focusing on failures due to rolling contact fatigue (RCF) at the rail head. Assuming a tangent rail with one-point contact at the running surface, a finite element analysis of a full-scale wheel-rail rolling contact with a nonlinear isotropic kinematic hardening material model is performed to simulate the accumulation of residual stresses and strains in the rail head. Using rolling stress and strain results from the sixth loading cycle, in which residual stresses and strains are at their steady-state, as input, two critical plane fatigue criteria are proposed for fatigue analyses. The first fatigue criterion is the stress-based approach—namely the Findley fatigue criterion. It suggests an important role of tensile residual stresses on subsurface crack nucleation and early growth in the rail head, but applications of the criterion to the near-running-surface region are limited because of plastic deformation from wheel-rail contact. The second fatigue criterion is the strain-based approach—namely the Fatemi-Socie fatigue criterion. Contributed mainly from shear strain amplitudes and factorized by normal stress components, the criterion also predicts fatigue crack nucleation at the subsurface as a possible failure

mode as well as fatigue crack nucleation at the near-surface, while maintaining its validity in both regions. A collection of fatigue test data of various types of rail steel from literature is analyzed to determine a relationship between fatigue damages and number of cycles to failure. Considering a set of wheel loads with their corresponding number of rolling passage as a loading unit (LU), optimizations of grinding schedules with genetic algorithm (GA) show that fatigue life of rail increases by varying amount when compared against that from the no-grinding case. Results show that the proposed grinding schedules, optimized with the exploratory and local-search genetic algorithms, can increase fatigue life of rail by 240%. The optimization framework is designed to be able to determine a set of optimal grinding schedules for different types of rail steel and different contact configurations, i.e. two-point contact occurred when cornering.

To My Late Grandmother, ใจฮวย แซ่โค้ว; My Late Aunt, อี๊เหมียว; and My Beloved Family

ACKNOWLEDGEMENTS

I would like to thank my mentor, Dr. Gary Fry, for his valuable guidance throughout the course of my doctoral study/training on both academic and personal life. The teaching and working philosophy he has passed to me will live to the coming generations.

Support and guidance from other committee members, Dr. Harry Jones, Dr. Stefan Hurlebaus, and Dr. Terry Creasy, are gratefully appreciated. My appreciation is also to colleagues in the research group for their support and friendship.

My deepest gratitude goes to my parents, Siriwan and Surapong Tangtragulwong, whose love and caring have raised and shaped me as I am today. I am also thankful for my sister, Patthara Tangtragulwong, my brother, Nat Tangtragulwong, and Puncharas Piriyathanasak for their endless support.

This project was conducted under the auspices of the Association of American Railroad which provided technical and financial support. Texas Transportation Institute and Texas A&M Supercomputing Facility are acknowledged for their generous allocation of facilities and computational resources.

TABLE OF CONTENTS

CHAPTER Page

CHAPTER Page

CHAPTER Page

LIST OF FIGURES

FIGURE Page

FIGURE Page

FIGURE Page

FIGURE Page

FIGURE Page

LIST OF TABLES

TABLE Page

TABLE Page

CHAPTER I

INTRODUCTION

1.1 Introduction

As axle load and train speed continuously increase to serve growing demands in North America and worldwide, rail maintenance planning becomes one of the most crucial components to provide safety and economical revenue. These two goals are inter-related and must be considered concurrently when planning. The weight of train or truck is measured in term of axle loads, which is distributed through track structures, from wheel-rail interface to sleepers, to ballast, and eventually to subgrade (Esveld [1]). Due to a relatively small non-conformal contact, the interface between wheel and rail head is where influences from rolling contact, i.e. stresses, strains, material hardening, and etc., are largest; therefore, it is most prone to failure than the web and base of rails, and other track components. A classification of types of defect in rails is presented in a Rail Defect Manual (Sperry Rail Service [2]).

With an application of repeating wheel loads onto the rail head, fatigue cracks form at both surface and subsurface regions within the rail head as a result of rolling contact fatigue (RCF), assisted by material imperfections from poor manufacturing and residual stresses from operation (Fry [3]). These incipient fatigue cracks could propagate and eventually cause rail failures, which may lead to catastrophic accidents.

This dissertation follows the style of *International Journal of Fatigue.*

In order to prevent unexpected failures from RCF, routine rail inspections and maintenances are firstly assigned to correct the problems. Rail grinding, surface lubrication, and rail replacement are three common rail maintenance practices that serve different purposes. Rail replacement is the least cost effective and usually used when the limit of surface grinding is reached or internal defects (subsurface fatigue cracks) are found, whereas surface lubrication is used to mitigate surface defects (surface fatigue cracks) by decreasing friction coefficient of wheel-rail interfaces. Rail grinding, in this case, in 'corrective' sense, is used to eliminate or shorten surface fatigue cracks that would propagate beyond critical limit by removing relatively large amount of material at running surface.

Originally introduced as a tool to mitigate rail corrugation problems, rail grinding is now a key approach to improve service life of rails in railroad industry. In contrast to the 'corrective' rail grinding, the 'preventive' rail grinding aims to minimize the formation of surface fatigue cracks, instead of eliminating visible surface fatigue cracks. The preventive rail grinding is currently planned solely based on intuitive, experience, or historical data, and, nevertheless, it is found to be able to prolong rail fatigue life in many corridors (Sroba et al. [4]) by removing relatively small amount of material at running surface for every specific cumulative amount of wheel load throughout the service life of rails. At present, there is yet no conclusive agreement on the amount of grinding and grinding frequency, which is one of the areas to be investigated in this study. The main contribution of this study is to develop a framework, consisting of: 1) the rolling contact fatigue analysis based on rolling stress-strain results from a wheel-rail

finite element simulation to predict the initiations of fatigue crack in rail heads , and 2) the optimization of grinding schedules that not only mitigate the surface fatigue defects, but also the subsurface ones.

1.2 Objectives and Organization

The objective of this study is to develop a framework to determine a set of optimal grinding schedules that maximize the service life of rail while maintaining material integrity of rail heads. Fatigue cracks, occurred at both surface and subsurface, will be taken into consideration of the optimization algorithm. The organization of this dissertation is given below.

Chapter II presents a full-scale finite element analysis of wheel-rail contact with a non-linear isotropic/kinematic hardening material. Chapters III and IV present multi-axial fatigue analyses of a rail head section as a result of rolling contact using stress-based and strain-based critical plane criteria respectively to predict life-to-crack-initiation of rails. Chapter V presents: 1) a development of the optimization framework for rail grinding, and 2) analyses of benefits of rail grinding in term of fatigue life. Chapter VI presents the overall conclusions of this study.

CHAPTER II

FINITE ELEMENT ANALYSIS OF WHEEL-RAIL CONTACT

2.1 Introduction

Rolling contact fatigue (RCF) has been considered as one of the root causes of many derailment accidents (Grassie et al. [5] and Smith [6]) and can be generally categorized into 2 classes: surface and subsurface types. Surface cracks, i.e. shelling and spalling, are due to localized plastic deformation of material closing to wheel-rail interface. Kapoor et al. [7] suggest that either low-cycle fatigue (LCF) or ratcheting is the failure mode of material in this region, e.g. their failure mechanisms are independent from each other. Other types of deformation and material shakedown that may occur at near running surface will be discussed later in this chapter. In contrast to surface cracks, subsurface cracks nucleate at some depth below running surface where material deforms elastically; typically, accompanying with a presence of material imperfections or discontinuities that may act as a stress riser. Therefore, the mode of failure of subsurface cracks is the high-cycle fatigue (HCF). Cannon et al. [8] note that this type of fatigue crack can be found in heavy-axle load lines more often than in passenger railways, due to larger accumulation of tensile residual stresses in the heavy-axle load case. Taken from Jablonski and Pelloux [9] and Sperry Rail Service [2], Fig. 2.1 presents examples of transverse and horizontal fatigue cracks nucleated below running surface within rail heads.

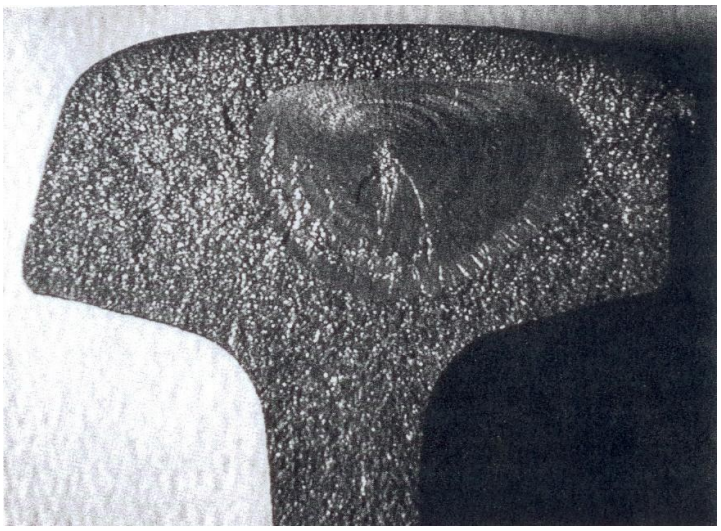

a)

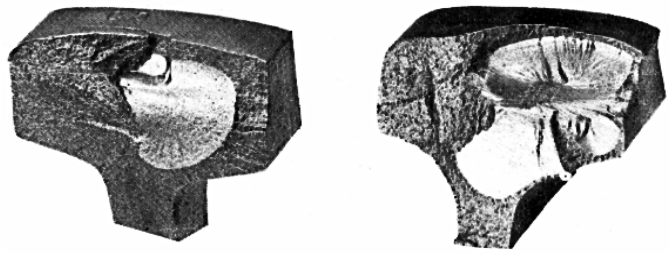

b)

Fig. 2.1. Rail head defects. (a) A subsurface crack from field test (Jablonski and Pelloux [9]), and (b) Transverse and horizontal fatigue cracks in rail heads (Sperry Rail Service [2]).

When a visible RCF surface crack is detected, it can be eliminated by a conventional corrective surface grinding to avoid further crack propagation, which could result in rail failures. Unlikely to be detected by a visual inspection, Tunna et al. [10], Ekberg and Kabo [11], and Smith [6] report that RCF subsurface cracks can cause abrupt failures in rails. Non-destructive methods, i.e. ultrasonic or induction methods,

must be used to detect the subsurface cracks instead with some limitations on resolution and reliability. Focusing on subsurface crack nucleation in the head of a thermite welded rail, Fry et al. [12] determine an approximated rolling stress result as a combination of elastic rolling stresses—derived from an analytical elasticity method—and residual stresses measured in a used rail. Assuming no discontinuities in the rail head, they show that if the measured residual stress is included in analyses, fatigue damage increases significantly at the region located 15-20 mm below the running surface. Not surprisingly, larger fatigue damage is observed when effects from both the residual stresses and discontinuities are included. This implies an important role of residual stresses on subsurface fatigue crack nucleation in rail head, which will be focused in this study.

The objectives of this chapter are: 1) to develop a full-scale finite element model of wheel-rail rolling contact with a nonlinear isotropic kinematic hardening material model that is able to predict the residual stresses in rail head effectively, 2) to provide an in-depth understanding of the state of stress from wheel-rail contact phenomena, including the corresponding strains and ratcheting behavior, 3) to discuss the capability of the material model used to simulate material hardening in rolling contact by comparing results against those from experiments, and 4) to study the influence of residual stresses on rolling stresses in term of fatigue damage. The finite element analysis (FEA) of wheel-rail contact should overcome limitations found in traditional analytical methods and two-dimensional FEA. It should be noted that effects from

thermal-mechanical coupling due to braking or heat transfer during service are not considered in this study.

2.2 Background

2.2.1 Rolling Contact Fatigue in Wheel-Rail Contact

Ekberg and Kabo [11] give an overview of RCF, specifically, in wheel-rail contacts with an emphasis on surface and subsurface crack nucleation and propagation. They suggest that RCF differs from the 'classical' fatigue analysis (i.e. uni-axial and bi-axial fatigue analyses) because of the following reasons: 1) the state of stresses due to rolling contact is multi-axial and non-proportional—principal stress directions change as rolling progresses, and 2) rolling contacts involve mainly with compressive loads. Experiments on various metallic specimens show that non-proportional load tends to activate a large number of slip planes as a result of the rotation of principal directions, which may create additional material hardening called non-proportional hardening. Hence, the non-proportional load could be more damaging than the proportional one. This non-proportional hardening effect is found to be material-dependent. It shows significant effect in 304 stainless steel (Itoh et al. [13]), and minimal effect in 1045 steel (Socie [14]) and carbon rail steel (McDowell [15] and Kang and Gao [16]).

Analytical solutions of contact stresses between two elastic bodies, derived from the *Hertzian contact* theory by Johnson [17], suggest that contact stresses are localized and limited to some distance from the contact area. However, large wheel loads used in heavy-hauled locomotive—around 150 – 250 kN—usually causes plastic deformation at

contact region such that the elastic solution is no longer valid. In order to accurately predict rolling stresses, a material model with plasticity and hardening rule must be incorporated into calculations. Sehitoglu and Jiang [18] develop an analytical approach based on an elastic analysis with a stress and strain relaxation method and a two-surface model of Mroz type hardening rule to simulate rolling and sliding contacts of the 1070 steel. Residual stress and strain results are comparable to those from finite element analyses; however, deviations from experiments are still observed. Jiang and Sehitoglu [19] further develop a semi-analytical approach based on the Armstrong and Frederick plasticity model [20], and are able to predict the decaying rate of ratcheting of material near running surface as observed in experiments. Other than LCF, ratcheting is considered to be one of the root causes of surface crack nucleation (Kapoor [7]), and the finding of plasticity model that is able to predict ratcheting rate accurately is still an active research topic. Also formulated based on the Armstrong and Frederick plasticity model, but with simpler form, the Chaboche plasticity model (Lemaitre and Chaboche [21], and Chaboche [22]) is able to predict the multi-axial hardening and decreasing rate of ratcheting. It is used in the FEA of wheel-rail rolling contact in this chapter and will be discussed in greater details in the next section.

At greater depth into the rail head, plastic deformation and ratcheting are no longer observed. However, the state of stress at this region is still non-proportional, with mean stress, as shown in analytical elastic analyses by Johnson [17] and Fry et al. [12]. A measurement of residual stresses in a used rail section by Steele and Joerms [23] shows compressive residual stresses at near contact region and tensile residual stresses at

depth greater than 7 mm below the running surface. From a measurement with sectioning method, Bower and Cheesewright [24] report similar compressive-to-tensile residual stress profiles of all normal components in a heavy-haul line. These tensile residual stresses are pointed out by Fry et al. [12] to be a potential root cause of subsurface crack nucleation and early growth, found at 15-20 mm below the running surface, in rolling contact. Assuming a perfect rail steel with no imperfections or discontinuities, fatigue damage increases by 60% when residual stress is included into the analysis. When accounting for both the residual stresses and discontinuities, fatigue damage increases up to 200% compared to one calculated from a pure elastic analysis. The capability of the FEA of wheel-rail rolling contact and the Chaboche plasticity model to predict residual stresses will be studied by comparing the simulated residual stresses against ones reported in Steele and Joerms [23].

2.2.2 Finite Element Analysis of Wheel-Rail Contact

In analytical and semi-analytical methods for wheel-rail rolling contact, various assumptions of plasticity models and the nonlinearity of wheel-rail geometry are made to determine the approximated solution as seen in Fry et al. [12], Sehitoglu and Jiang [18], and Jiang and Sehitoglu [19]. The analyses are typically limited to two-dimensional models for simplicity. To overcome these limitations, finite element method (FEM) has been adopted by many researchers to determine the numerical solutions of wheel-rail contact problems. Several variations of nonlinear kinematic plasticity model are written as material subroutines for implementing in commercial FEA software, i.e.

ABAQUS® and ANSYS®, to simulate multi-axial hardening and ratcheting of rail steels (Johansson and Thorberntsson [25], Ekh et al. [26], and Jiang et al. [27]). In literatures, FEA of wheel-rail contact can be classified into two approaches. In the first approach, an assumed Hertzian pressure distribution is applied onto the running surface of a rail model, without actual contact between wheel and rail models. In the second approach, rail and wheel models are made into contact to simulate the more realistic contact phenomena, giving the situation closer to reality, but with higher computational cost. The advantages of the first approach are simplicity and its relatively low computational cost; however, models may not be able to capture real contact phenomena. The model developed in this study is considered as one in the second approach, with an addition of an axle component to represent an un-symmetric vertical load from a train truck.

The followings are examples of research done based on the first simplified approach. Focusing on fatigue damage in rails, Ringsberg et al. [28] simulate a wheel-rail contact through an application of Hertzian contact pressure on a FEM of a section of rail for 16 loading cycles. Elements of the rail model near contact region are modeled with a nonlinear isotropic kinematic hardening material behavior proposed by Chaboche [22] such that the material is strain-hardened and the accumulation of plastic strain increases in the direction of mean stress with decaying rate. They suggest a significant contribution of the first wheel passage on the accumulation of residual stresses. A similar finite element analysis is done by Ringsberg and Josefson [29] and Jiang et al. [27] with the Jiang plasticity model (Jiang and Sehitoglu [30, 31]). Kulkarni et al. [32]

and Bhargava et al. [33] study a FEA of rolling contact with a linear kinematic hardening plasticity model and report that residual stresses reach a steady state after just one cycle of a 149 kN wheel load.

There is much less literatures available on the FEA of full-scale wheel-rail contact. Liu et al. [34] apply a sub-modeling technique with a bi-linear kinematic hardening plasticity model to determine rolling stresses, which afterward are used to calculate the life to fatigue crack nucleation of a railroad wheel. They show that the predicted contact stress contours deviate from traditional Hertzian contact theory, and there are multiple contact points at the wheel-rail interface, suggesting a non-Hertzian contact condition. Similar numerical results of the non-Hertzian contact condition are reported by Telliskivi and Olofsson [35].

2.2.3 Material Model for Cyclic Loading

2.2.3.1 Response of Material Subjected to Cyclic Loading

An elastic-plastic structure can respond to cyclic loading with non-zero mean load in four different ways: elastic, elastic shakedown, plastic shakedown, and ratcheting as shown in Fig. 2.2. First, a structure behaves elastically when loaded below its elastic limit. As the load level increases beyond the elastic limit, a plastic flow, which takes place on the first overloading cycle, will create residual stresses and strain-harden the material. This hardening process will help resisting plastic flow that occurs in subsequent loading cycles and enable the structure to *shakedown* to perfectly elastic state again: so called the *elastic shakedow*n. As the structure is loaded further beyond

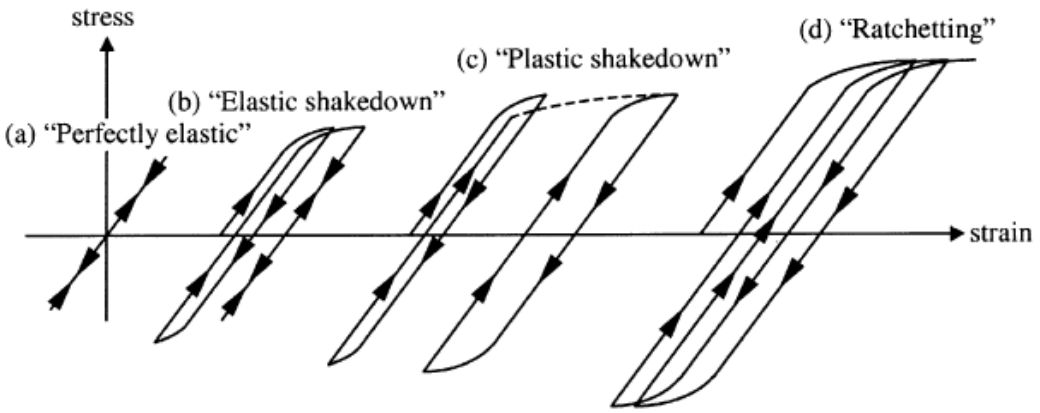

Fig. 2.2. Illustration of different material responses that may occur for a material subjected to cyclic loading with non-zero mean load (Ringsberg et al. [28]).

the elastic shakedown limit, *plastic shakedown* is obtained if its corresponding stress-strain path forms a closed loop. In contrast, the structure is considered to be *ratcheting* if the accumulation of plastic strain progresses in the direction of mean stress—with a constant or decaying rate, depending on type of material—is observed.

Bower [36] performs a load-controlled tension/compression test with mean stresses, both proportional and non-proportional, on cylindrical specimens of carbon rail steel to mimic the state of stress in rolling contact. A non-proportional stress state is induced by a combination of three loading configurations: tension, shear, and compression. He makes an important observation on ratcheting behavior of the rail steel that plastic strains accumulate in the direction of mean stresses with decreasing rate, when material ratchets. Another effect that should be considered in rolling contact is an additional hardening from the non-proportional state of stresses as numbers of slip planes could be activated. However, results from non-proportional cyclic tests by

McDowell [15], and Kang and Gao [16] show that rail steels exhibit negligible amount of this type of material hardening. As a result, in order to predict rolling stresses and strains of a rail steel in rolling contact accurately, the plasticity model must accommodate the accumulation of residual stresses and decaying rate of ratcheting, while the material hardening due to loading non-proportionality may be disregarded.

2.2.3.2 Plasticity Model for Strain Hardening and Ratcheting Predictions

Due to heavy axle loads in locomotive industry, localized plastic deformation occurs at the wheel-rail contact interface (Bower and Johnson [37]). Such a compressive deformation at running surface is balanced by tensile residual stresses at subsurface, which is found to play an important role in fatigue crack nucleation, as described in previous section. In order to determine rolling stress results of wheel-rail contact phenomena with heavy axle loads correctly, a plasticity model should be able to capture two important characteristics of cyclic rolling contact: 1) residual stresses in rail head, and 2) decaying rate of ratcheting of materials. The variations of isotropic and/or kinematic hardening are presented by Khan and Huang [38], and Lemaitre and Chaboche [21]. Using *von-Mises* yield surface, a kinematic hardening model proposed by Frederick and Armstrong [17], has been widely used by researchers as a basis to simulate strain-hardening and ratcheting behavior in general multi-axial applications. Comprehensive reviews of the topic are given by Chaboche [39], Jiang and Kurath [40], and Ohno [41].

In general, isotropic and kinematic hardening rules are coupled in plasticity models. The isotropic hardening rule predicts change of the size of yield surface as plastic deformation evolves, while the kinematic hardening rule is responsible for the translation of yield surfaces—called *Bauschinger effect*—due to cyclic load. The kinematic hardening rule also controls the ratcheting behavior of material; as a result, the modifications of plasticity model are mainly focused on this kinematic part. Since the linear kinematic hardening rule predicts a close-loop stress-strain response with no ratcheting, Frederick and Armstrong [20] introduce a nonlinear kinematic hardening rule with an internal variable called the *recall term*, which is able to predict ratcheting strain. However, the ratcheting strain is still overpredicted and deviates significantly from experiments. Chaboche [22] refines the Frederick and Armstrong plasticity model by decomposing the recall term into several components and including a *threshold term* to control ratcheting rate. He also suggests an addition of isotropic hardening model to the main nonlinear kinematic hardening model and shows that the proposed plasticity model reproduces very well stress results for monotonic, cyclic, and ratcheting cases. This plasticity model is known among researchers as the Chaboche plasticity model. Bari and Hassan [42] investigate the Chaboche plasticity model and report that the model satisfactorily predicts ratcheting strains under non-symmetrical loading in carbon steels. Further modification of the recall term is done by Ohno and Wang [43] by including a *critical state* and nonlinearities into the recall term of the Frederick and Armstrong plasticity model. Based on the Ohno and Wang plasticity model, Jiang and Sehitoglu [30, 31] modify the exponent of the recall term. Bari and Hassan [44] notes that all three

plasticity models: the Chaboche, Ohno and Wang, and Jiang and Sehitoglu models, generally overpredict multi-axial ratcheting when parameters are determined from cyclic uni-axial cases. An implementation of the Chaboche plasticity model and Jiang and Sehitoglu plasticity model to rolling contact are done by Ringsberg [28] and Ringsberg and Josefson [29] respectively, and will be discussed later in details.

2.2.4 Implementation of Frederick and Armstrong Based Plasticity Models to Rolling Contact

Bower and Johnson [37] perform an analytical study of rolling/sliding contact with the nonlinear kinematic hardening model proposed by Frederick and Armstrong [20]. The parameters in the model are determined from experimental results of a cyclic tension/compression test on rail steels, expecting that they are able to predict plasticity behavior for both proportional and non-proportional loading cases. However, a significant error is observed for the residual stress prediction (see also Bower [36]).

Using test results on rail steels available from Bower [36], Johansson and Thorberntsson [25] develop an optimization algorithm to calibrate parameters for the Chaboche plasticity model to results from cyclic uni-axial tests with mean stress. Four parameters, excluding the initial yield stress, of the Chaboche plasticity model: e.g. the kinematic hardening modulus, the decreasing rate of the kinematic hardening modulus, the maximum increased value of yield stress, and the yield surface development rate, are determined. The optimization result shows a correct ratcheting rate prediction, but with some deviation of the shape of stress-strain plots. Using stress-strain profiles of specific

loading cycles, Ringsberg et al. [28] later apply this optimization approach to determine parameters for the Chaboche plasticity model and implement it into the material library of ABAQUS 6.7® to study a FEA of rolling contact. A similar optimization and calibration procedure for the Jiang and Sehitoglu plasticity model is performed by Ekh et al. [26]. The predicted stress-strain profiles show a good agreement with those from experiments. The Jiang and Sehitoglu plasticity model is implemented as a material subroutine in ABAQUS® to study the FEA of rolling contact by Ringsberg and Josefson [29] and Jiang [27]. In this study, the Chaboche plasticity model is used for its less complexity, which is more suitable to the study of a FEA of a computationally intensive full-scale wheel rail contact.

2.3. Finite Element Analysis of Wheel-Rail Contact

2.3.1 Wheel-Rail Finite Element Model

HYPERMESH 8® and ABAQUS 6.7® software are used as a pre/post processing software and a finite element solver respectively. Since the wheel-rail contact model has both geometric and material nonlinearities, which require extensive computational resources, input files of the model, created on a personal computer with HYPERMESH 7®, are uploaded to supercomputers, provided by the Texas A&M Supercomputing Facility, to perform analyses. Results are then transferred back to the personal computer again for post-processing.

The wheel-rail model consists of three main parts in full-scale: axle, wheel, and rail. Wheel and rail profiles provided by the Association of American Railroads (AAR)

are meshed with variable elemental densities as shown in Fig. 2.3. In order to capture accurate contact phenomena, very fine elements are needed at the wheel-rail contact region; widths of the elements of wheel and rail model made into a contact are 4 mm and 2 mm respectively. For the wheel model, element size is gradually increased as moving away from the contact region to avoid excessive computational time. In the rail model, size of elements in rail head region—the area of interest in this study—is approximately uniform, and the rail head is divided into 7 regions for convenience in model preparation and data processing.

Fig. 2.4 shows the two-dimensional mesh of a rail head. Three different parts (in pink, blue, and yellow) located at the center under the contact area, from 0 – 40 mm below running surface, are the areas of interest in this study. Width of each section is 40 mm, covering region affected by the contact. Elements are uniform with size of 2x1 mm^2 (width x height). Element height of 1 mm is intended to agree with the proposed resolution of grinding thickness, which is 1 mm as well.

A three-dimensional wheel-rail model is shown in Fig. 2.5. The rail is sub-modeled into 2 parts: rail head and rail base. The inner part of the rail head—where fatigue damages due to rolling contact tend to occur (see Fig. 2.6)—is longitudinally extruded with 2 mm increment for 120 mm. The outer parts of the rail head are extruded further from both sides of the inner part with 10 mm increment for 240 mm; therefore, the total length of the rail model is 600 mm, which represents a distance between two adjacent ties. The rail base is created separately with 10 mm increment for 600 mm throughout the rail section. Elemental mismatches where the rail head and the rail base

are connected are controlled by an ABAQUS subroutine—TIE—to guarantee compatible displacement of nodes at the boundaries.

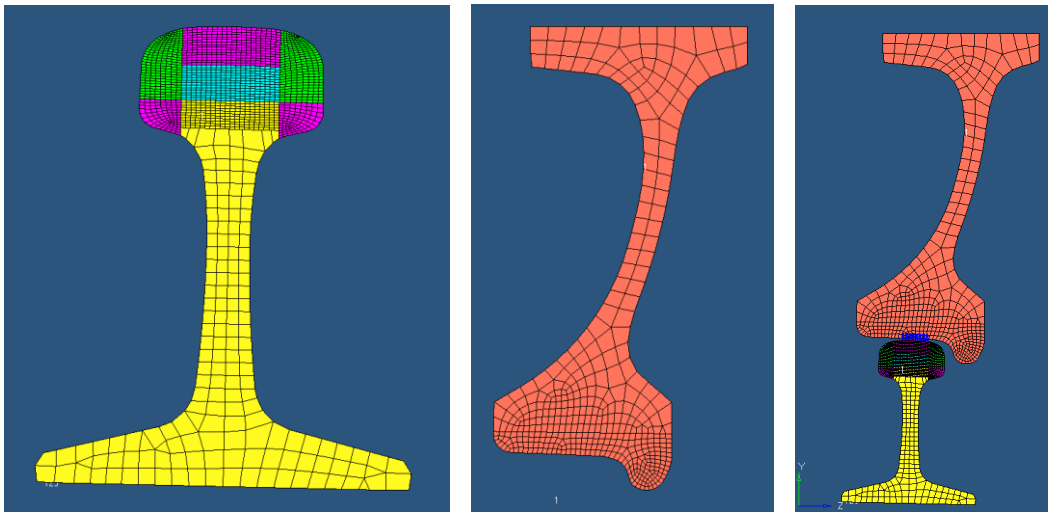

(a) (b) (c)

Fig. 2.3. Two-dimensional meshes of (a) the rail; (b) the wheel; and (c) 2-D mesh of both wheel and rail.

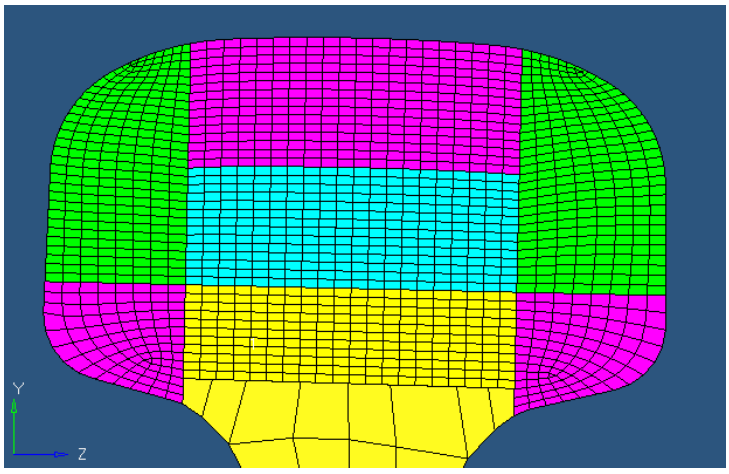

Fig. 2.4. Two-dimensional mesh of the rail head.

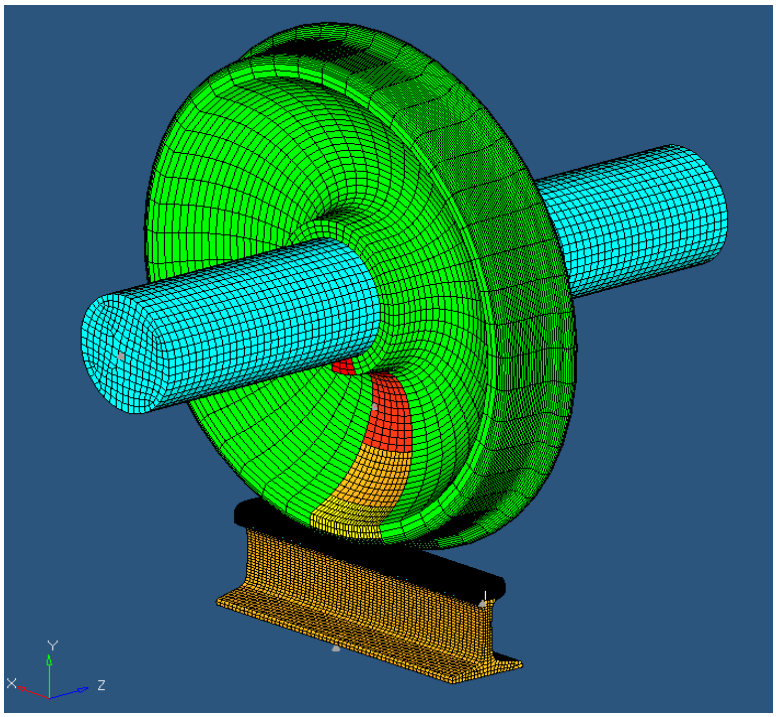

Fig. 2.5. Finite element model of wheel-rail contact.

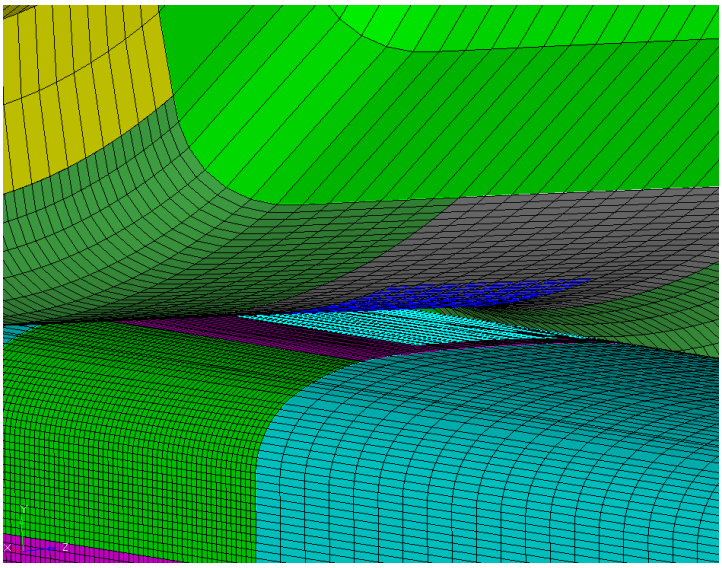

Fig. 2.6. Wheel-rail contact interface.

The axle is extruded as a cylinder, which its elements in both the axial and circumferential directions are designed to match with those of the wheel hub; so that the connectivity between elements of axle and wheel hub is well defined, making the axle and wheel models behaving as a single unit. The wheel model consists of two main parts. One, which is the region expected to make contact, is revolved for 24 degree about the axle's center line with the finest elements at contact region (0.5 degree-per-element). As moving toward wheel's center, element size gradually increases up to 8 degree-per-element at the wheel hub. For the part with no contact, a uniform element size of 8 degree-per-element is used throughout the rest 336 degree of the wheel model. Similarly, elemental mismatches found in the axle-wheel unit are controlled by the ABAQUS subroutine—TIE—to guarantee compatible displacement of nodes at the interface.

An eight-node brick element with reduced integration (C3D8R) is used in all parts for two main reasons. First, the first-order element will give more accurate pressure distribution in contact problem; the second reason is to reduce computational time with relatively small trade-off of the accuracy. The contact in wheel-rail interface is the element-to-element type with strict master-slave relationship and the finite sliding algorithm. Surfaces of wheel and rail expected to make contact are defined as a master and a slave surface respectively, as shown in Figure 2.6. Size of elements of the master surface (wheel) is designed to be at least twice as large as that of the slave surface (rail) to avoid possible nodal penetrations between the master and slave surfaces, which could lead to numerical errors. In this finite element model, the sizes of elements on the master

and slave surfaces are 4x4 mm^2 and 2x1 mm^2 respectively. The characteristic length of the wheel-rail model is 5.78 mm. Contact algorithm used in this study is the Lagrange multiplier method with hard contact to avoid errors from excessive penetrations between nodes in contact. Only in the rolling step, a friction coefficient of 0.3 is applied to the contact definition to nucleate rolling action of wheel in driven condition as a result of the translation of the axle-wheel unit in longitudinal direction as shown in Fig. 2.7. Because stiffness matrices in finite element analysis are unsymmetric due to the presence of surface friction, the unsymmetric solver is set to be active. Note that the forward motion of the driving wheel is from the applied torque that gives a reaction force acting on rail surface in backward direction; while the forward motion of the driven wheel is from the translation which is resisted by friction forces at wheel-rail interface, giving a reaction force that acting on rail surface in forward direction. Driven wheel configuration can be found in trucks, following the leading trucks where engines operate.

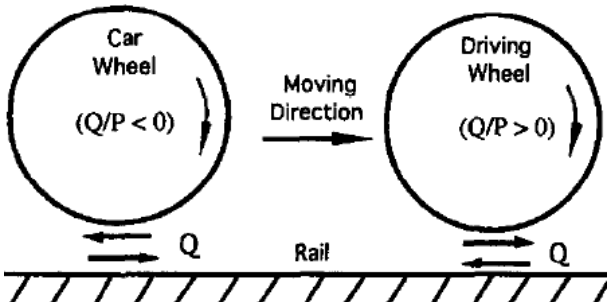

Fig. 2.7. A schematic shows the driven wheel (left) and driving wheel (right) (From Jiang and Sehitoglu [19]).

To reduce computational time, only elements near the region expected to make contact, i.e. the elements located 0 – 20 mm from running surface of the inner part of the rail head and the elements with 0.5 degree-per-element of the wheel, are defined with the nonlinear isotropic/kinematic hardening material behavior. The elastic material behavior is used in the rest of the model. The rail model is 1.3 degree inwardly inclined about the longitudinal axis as in actual configuration. Due to symmetry, half of the axle-wheel unit is modeled with a symmetric boundary condition at the mid-length of the axle by preventing the lateral displacement of the axle-wheel unit. Varied amount of wheel loads is imposed on a node of the axle on field-side through a mass element with gravity, so that a resultant force due to wheel load remain in the vertical direction as wheel rotates. At both ends of the rail model, the end cross sections are prevented from moving in the longitudinal direction, and the nodes at the rail base, located at 0–10 mm from both rail ends, are prevented from moving in the vertical direction as they are supported by ties. This will allow the effects from global bending to be included in the rolling contact.

In summary, the axle-wheel model has approximately 54500 nodes and 48100 elements, and the rail model has approximately 178000 nodes and 166000 elements.

2.3.2. Plasticity Model and Mechanical Properties of a Pearlitic Rail Steel

Three ingredients of a typical plasticity model are: yield criterion, flow rule, and hardening rule. Given a state of stress, yield criterion determines whether plasticity occur in a structure. As plasticity is observed, the direction of plastic flow and amount of

material hardening must be defined by flow rule and hardening rule respectively. For the Chaboche plasticity model, the von-Mises equivalent stress is the yield criterion, which is defined as:

$$\sqrt{\frac{3}{2}(S-\alpha^{dev}):(S-\alpha^{dev})}-\sigma^{0}=0 \qquad (1)$$

where S is the deviatoric stress tensor

α^{dev} is the deviatoric component of the *backstress tensor*

σ^{0} is the yield stress

As for typical metallic materials, the associative flow rule defines that plastic flow direction coincides with the normals of a yield surface. The nonlinear isotropic kinematic hardening rule proposed by Chaboche [22] with one backstress term consists of two components. The first component is the nonlinear kinematic hardening part, which describes a translation of yield surface in stress space, observed as the *Bauschinger effect* in cyclic loading tests, through the backstress tensor (α). The second component is the isotropic hardening part, which describes the uniform change of a yield surface as a function of plastic deformation. These two hardening components together will predict a cyclic material hardening, and a ratcheting and its decaying rate.

The isotropic hardening rule of the plasticity model defines evolution of the yield surface size (σ^{0}) as a function of the equivalent plastic strain ($\bar{\varepsilon}^{pl}$). This evolution can be defined by a simple exponential law as follows (Abaqus [45]).

$$\sigma^{0}=\sigma|_{0}+Q_{\infty}(1-e^{-b\bar{\varepsilon}^{pl}}) \qquad (2)$$

where $\sigma|_0$ is the yield stress at zero plastic strain

Q_∞ is the maximum change in size of the yield surface

b is the rate at which size of the yield surface changes as the plastic straining develops

The nonlinearity of the kinematic hardening component is introduced through a recall term, which is added to a purely kinematic term (the linear *Ziegler hardening law*). The nonlinear kinematic hardening rule with a back stress term in temperature-independent condition is:

$$\dot{\alpha} = C\frac{1}{\sigma^0}(\sigma - \alpha)\dot{\bar{\varepsilon}}^{pl} - \gamma\alpha\dot{\bar{\varepsilon}}^{pl} \tag{3}$$

where C is the initial *kinematic hardening modulus*

γ is the rate at which the kinematic hardening modulus decreases as plastic deformation increases

$\dot{\alpha}$ is the rate of change of the back stress tensor

$\dot{\bar{\varepsilon}}^{pl}$ is the plastic strain rate

The parameters Q_∞, b, C, and γ in isotropic and non linear kinematic hardening rules must be calibrated against results from a cyclic test with mean stress. Ringsberg et al. [28] optimize the parameters in the Chaboche plasticity model with stress-strain data, given by Bower [36], from cycles 1, 2, 15, 50, 100, 200, 400, and 600

of a uni-axial cyclic test with mean stress on rail steels. The material properties and hardening parameters for a pearlitic rail steel used in this analysis are given below.

- Young's modulus $E = 209$ GPa
- Poisson's ratio $\upsilon = 0.29$
- Initial yield stress $\sigma_y = 406$ MPa
- Kinematic hardening modulus $C = 13.2$ GPa
- Kinematic hardening modulus decreasing rate $\gamma = 3.12$
- Maximum increase in elastic range $Q_\infty = 152$ MPa
- Yield surface development rate $b = 3.97$

For the case without material hardening, only Young's modulus and Poisson's ratio are specified in the model.

2.4 Analysis Steps

2.4.1 FEA of Wheel-Rail Contact with an Elastic Material

First, the finite element model with elastic material behavior is investigated so that the rolling stress results can be compared against those with the plasticity model. Only the section at mid-length of rail is studied as combined effects from global bending and rolling contact is greater than other regions. Initially, the bottom surface of wheel and the top surface of rail expected to make contact are vertically 0.05 mm apart. The simulations represent the rolling state in a tangent track with one point contact, where the contact between the wheel rim and gage-sided of rail head found when negotiating curves is not considered. Based on the results from preliminary work, the author finds

that as contact occurs, the change of rolling stresses is observed only the region within 35 mm to the left and right of the contact point. This implies that if only the center cross-section of rail is interested, it will need only 70 mm of total rolling distance. As a result, in this study, the axle-wheel unit is located at 35 mm to the left of the center section of rail at the beginning, and it will roll to the point located at 35 mm to the right of the center section of rail to complete a cycle of 70 mm rolling distance, as the schematic shown in Fig. 2.8. The following steps are exploited for the 162 kN wheel load.

- Step 1: Apply a vertical displacement of 0.1 mm to the axle node to nucleate a firm contact between wheel and rail surfaces.
- Step 2: Activate gravity to make the mass element active.
- Step 3: Deactivate the vertical displacement applied in step 1. Keep only the effect from the mass element.
- Step 4: Activate friction and nucleate rolling contact by displacing the axle node in the longitudinal direction for 70 mm.
- Step 5: Deactivate the gravity and move the axle-wheel unit up for 1 mm to eliminate contact.

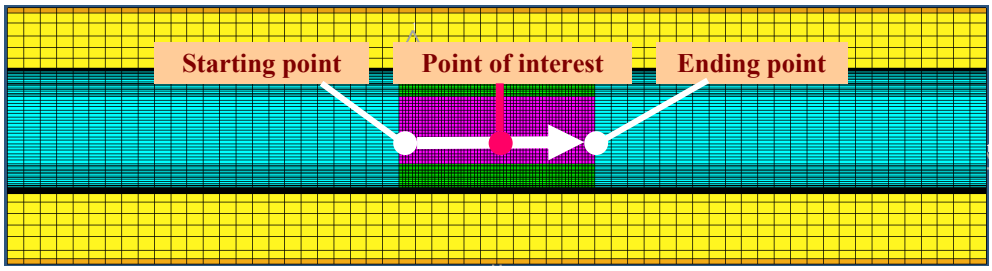

(a)

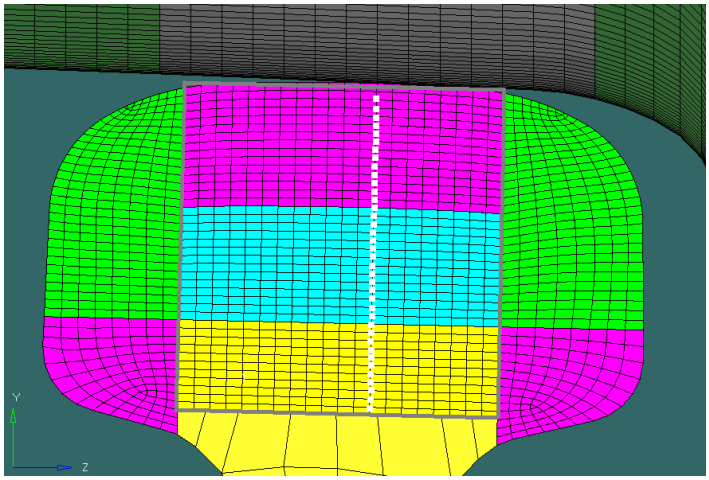

(b)

Fig. 2.8. (a) The schematic presents the simulation of the rolling contact, and (b) cross-section of interest (cropped) and a line of nodes right under the wheel-rail contact (white dotted).

2.4.2 FEA of Wheel-Rail Contact with Plasticity Model

In this model, the accumulation of residual stresses is studied as a repeating wheel-rail rolling contact progresses. After each loading step, the state of stresses and material hardening variables in the rail head will be imported to the subsequent simulation as a predefined state, while maintaining the same global coordinate; hence allow residual stresses to build-up as the number of wheel passage increases. Note that

the IMPORT command in ABAQUS® is used for this purpose. Two FEMs of wheel-rail with different meshing densities are used in this study. The first model of a wheel-rail contact with 162 kN wheel load and smaller element density is to study the rate of residual stress accumulation in rail head. The key question of this simulation is: for this Chaboche plasticity model, how many rolling cycles is required for residual stresses to reach the steady-state? Results will be used as a guideline to perform analyses with finer elements of the 162 kN and 233 kN wheel loads to study the influence of wheel loads on residual stresses. Similar to the one with an elastic material, all simulations with material hardening are performed as the following.

- Step 1-5: As same as those in the simulation with an elastic material.
- Step 6: Import the state of stresses and material hardening variables in the rail head at the end of present step to the subsequent step.
- Step 7: Repeat steps 1 to 6 until residual stresses reach the steady-state.

2.5 Results and Discussion

A typical 162 kN wheel load is selected as a benchmark to study the variation of various parameters, e.g. amount of wheel loads and mechanical behavior of rail steel, on rolling stresses/strains and development of residual stresses. In order to depict influence of residual stresses on rolling stresses, majority of the results are reported as comparisons between the cases with an elastic material and a hardening material. Three principal axes of interest of a rail are the vertical, longitudinal, and transverse axes as defined in Fig. 2.9. The normal stress directions are defined according to these three

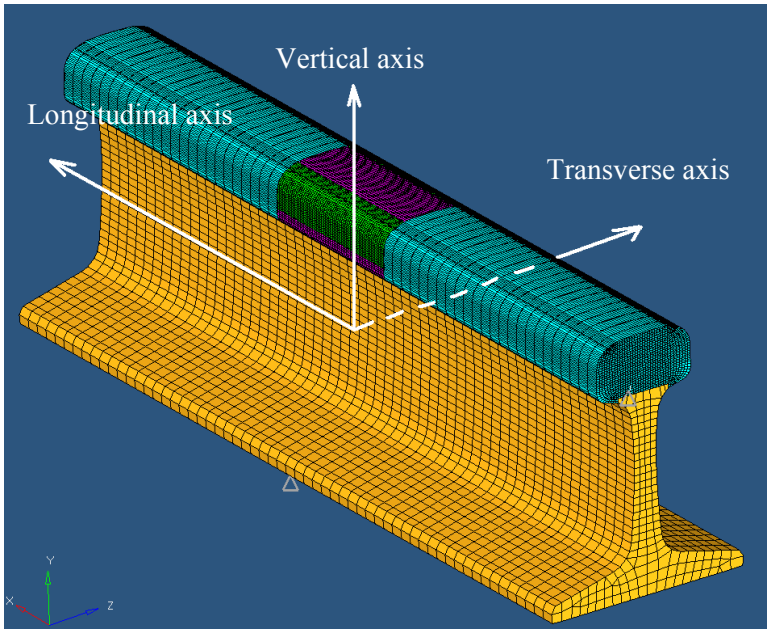

(a)

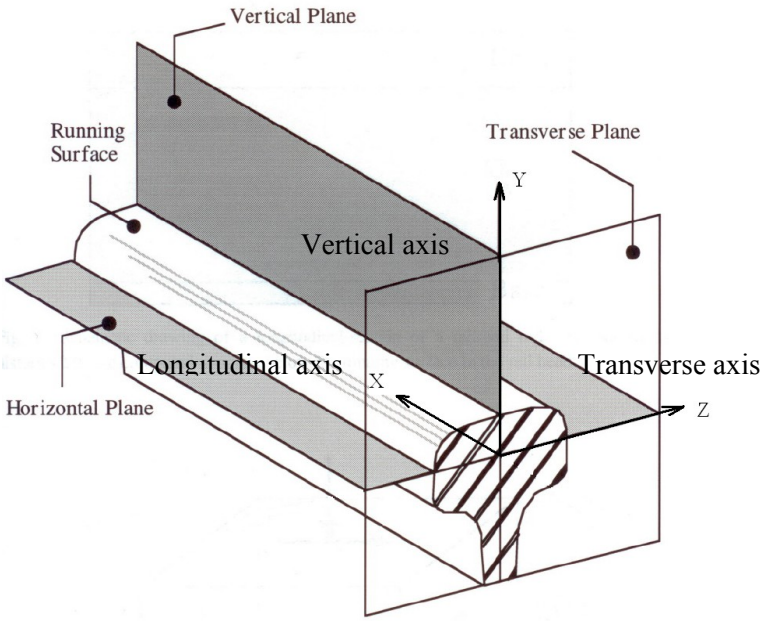

(b)

Fig. 2.9. (a) Principal axes of interest in a rail model, and (b) Three orthogonal planes of interest (Adapted from Fry [3]).

principal axes. The cross section of interest is located at the middle—35 mm from the starting point—of the 70 mm-long rolling path, right under the point of contact as in a schematic shown in Fig. 2.8. Note that throughout this study, this cross section will be an area of interest, unless specified otherwise. Results will be reported for the rectangular cross-section at center or sometimes only for the vertical line of nodes right under the wheel-rail contact, as shown in Fig. 2.8 (b), as appropriate.

2.5.1 The Steady State of Residual Stresses

Fig. 2.10 shows the accumulations of residual normal stresses of a node located at 15 mm below running surface—an area where large accumulation of residual stresses is expected—from cycle#1 to cycle#9. Rail cross-section of interest is located at the middle of the running path as indicated earlier. Using the defined nonlinear isotopic kinematic hardening rule—Chaboche plasticity model, result suggests that the accumulation of residual normal stresses will reach steady-state after four to five cycles of rolling contact. This preliminary result suggests that, for the refined model, only approximately five passages of wheel is required for residual stresses to reach the steady-state; therefore, the rolling stresses of the sixth loading cycle can be used in further analyses to account for effects from stabilized residual stresses.

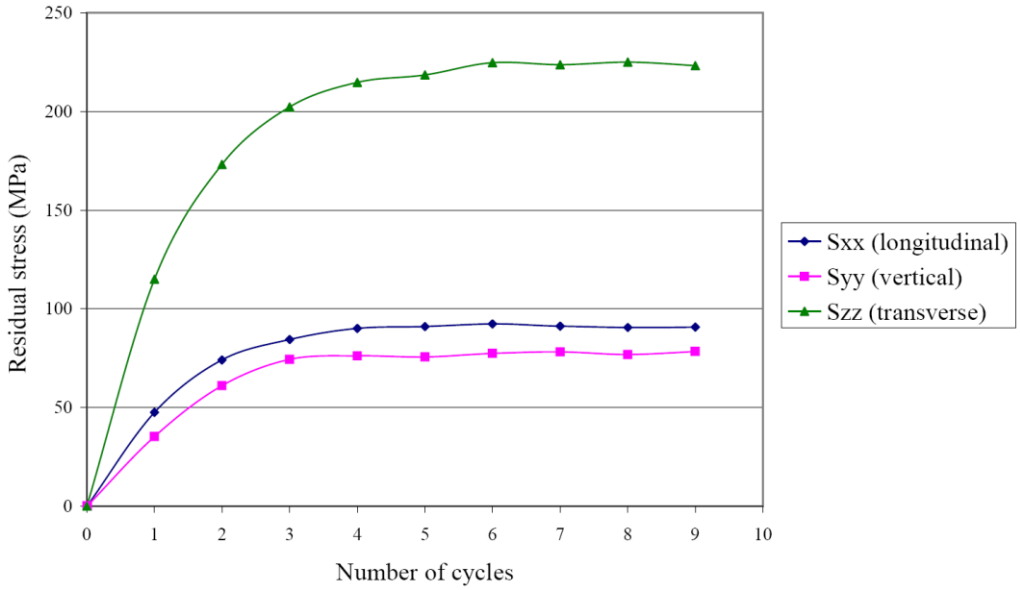

Fig. 2.10. Accumulation of the residual normal stresses of a node located at 15 mm below running surface from the preliminary model with coarser elements (162 kN wheel load).

2.5.2 Accumulation of Residual Stresses in Rolling Contact

At the same cross-section of interest, for the model with finer elements, residual stress results are collected for all nodes vertically located right under the point of contact from depth of 0 to 40 mm. Fig. 2.11 shows residual stress profiles accumulated along those nodes at after five loading cycles with the 162 kN wheel load. In this figure, 'y = 0' represents the running surface level and negative value of 'y' represents the depth from the running surface. It shows that, at all depths, the accumulation of residual shear stresses is much less significant when compared to those of residual normal stresses, as also reported by Bower and Cheesewright [24] for a measurement of residual shear stresses in a used rail steel. This justifies the use of the normal component of residual stresses for finding the number of cycles to their steady-state. The normal components of

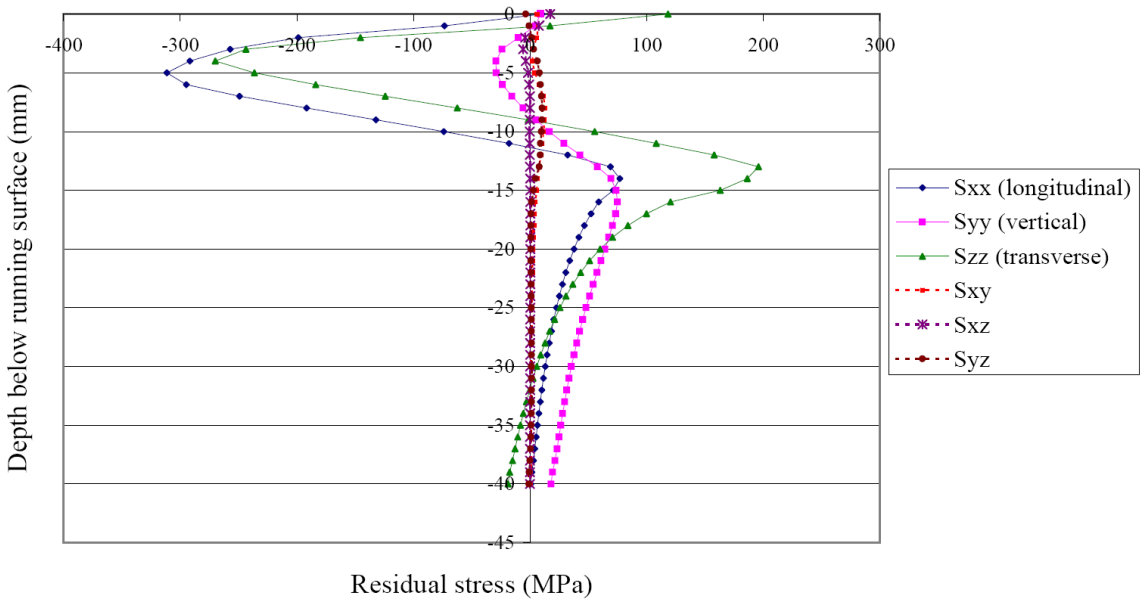

Fig. 2.11. Residual stress profiles accumulated in nodes located vertically from the point of contact after five loading cycles of the 162 kN wheel load.

residual stresses from the 162 kN and 233 kN wheel loads are compared against ones from a measurement (Steele and Joerms [23]) as shown in Fig. 2.12.

In general, the residual stress profiles from simulations—of both the 162 kN and 233 kN wheel loads after five loading cycles—agree with those from the measurement and can be classified into three regions. Note that the 162 kN wheel load (Fig. 2.12 (a)) is chosen for the followings discussion. First, at near running surface from 0-10 mm below the running surface, there are compressive residual stresses as a result of severe plastic deformation from concentrated load. The longitudinal and transverse residual stresses from the simulation are more compressive than those from the measurement with peak stresses at approximately -300 MPa. However, in contrast to the measured profiles, where largest compressive stresses are observed on running surface, the

predicted longitudinal and transverse compressive residual stresses gradually develop from running surface and reach their maximum at 5 mm below running surface. This discrepancy could be a result of numerical approximations of the Lagrange multiplier method used in contact, especially for the case of non-conformal wheel-rail contact. For vertical residual stress, while the stress profiles are similar, the predicted one is less compressive than the measured one. But since information about wheel loads of the used rail in measurement is not available, discussions on the differences of stress magnitude is inconclusive.

Until the depth of 10 mm below running surface, there locates the second region. Residual stresses reverse to tension and reach peak values at depth of 13-20 mm, depending on amount of wheel load. Predictions of residual normal stress profiles—in tensile—agree well with those from measurement, with relatively small discrepancy in magnitude. Residual stresses eventually go back to neutral or compressive state at the third region, where the depth below running surface is greater than 30 mm. Compared to the measurement, results from the simulations tend to reverse to compressive state at greater depth. Profiles of residual stresses from the 162 and 233 kN wheel loads are similar. The differences of the residual stresses at near running surface in both wheel loads are small, while tensile residual stresses in region 2 will grow deeper with greater magnitude as wheel load increases. Note that as wheel load increases from the 162 to 223 kN, the increase of the peak value of accumulated compressive residual stresses is less than that of the accumulated tensile residual stresses. This will be shown to have an

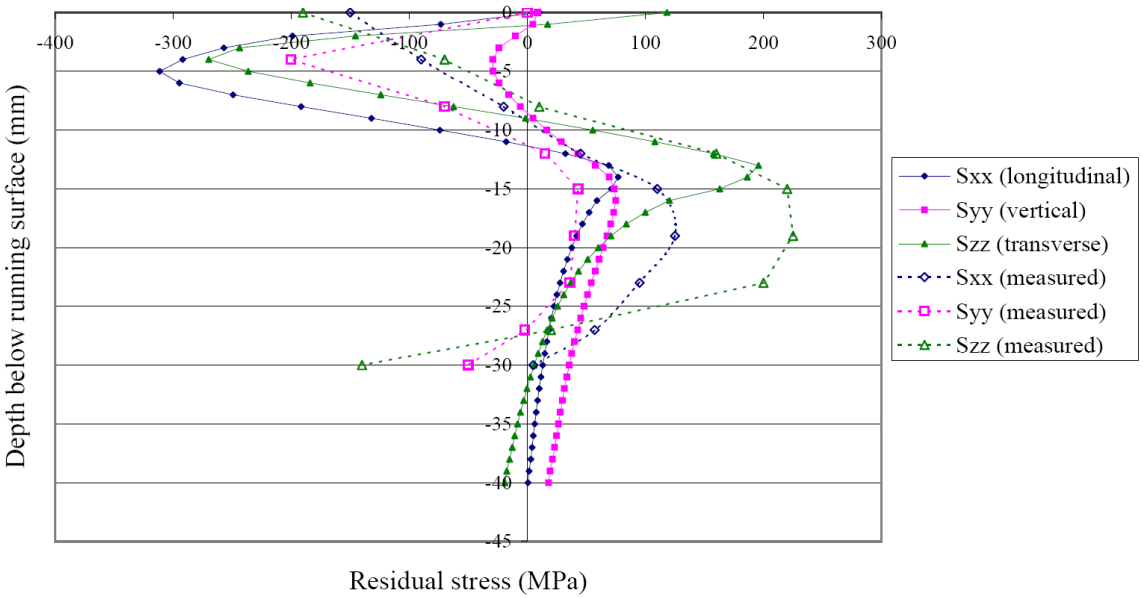

(a)

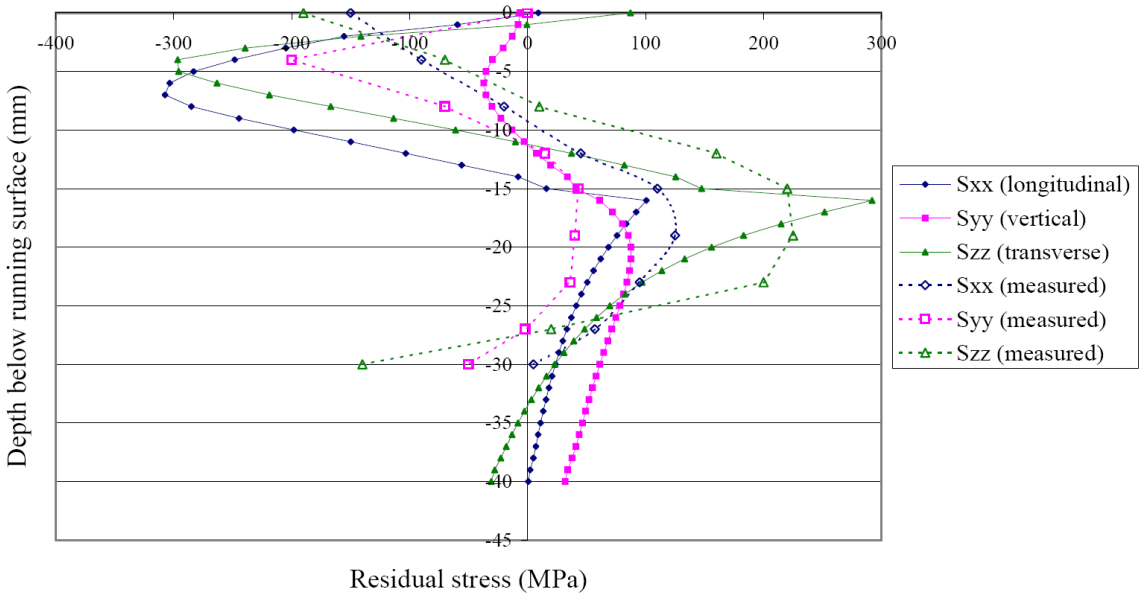

(b)

Fig. 2.12. A comparison between residual stress profiles from simulations and the measurement (Steele and Joerms [23]) of a line of nodes located vertically below the contact path for: (a) 162 kN wheel load, and (b) 233 kN wheel load.

effect on behavior of subsurface fatigue crack nucleation in fatigue damage analysis in Chapter III.

To study an influence that residual stresses have on rolling stresses in the 162 kN wheel load, the analyses in the next section are undertaken for four levels of depth from running surface as the following.

1. At 5 mm below running surface, where severe plastic deformation occurs and the maximum compressive residual stresses are found.
2. At 13 mm below running surface, where the maximum tensile residual stresses are found.
3. At 20 mm below running surface, where mild tensile residual stresses are found.
4. At 40 mm below running surface, where relatively low tensile or compressive residual stresses are found.

For completeness, it should be useful to present all three normal components of residual stresses of the whole representative cross-section as shown in Fig. 2.13. The residual stress contours show that residual accumulations are localized within 10–15 mm radius from the contact point and 0-40 mm below running surface, justifying the use of the proposed 40x40 mm^2 representative cross-section and the vertical line of nodes located inside for further analyses.

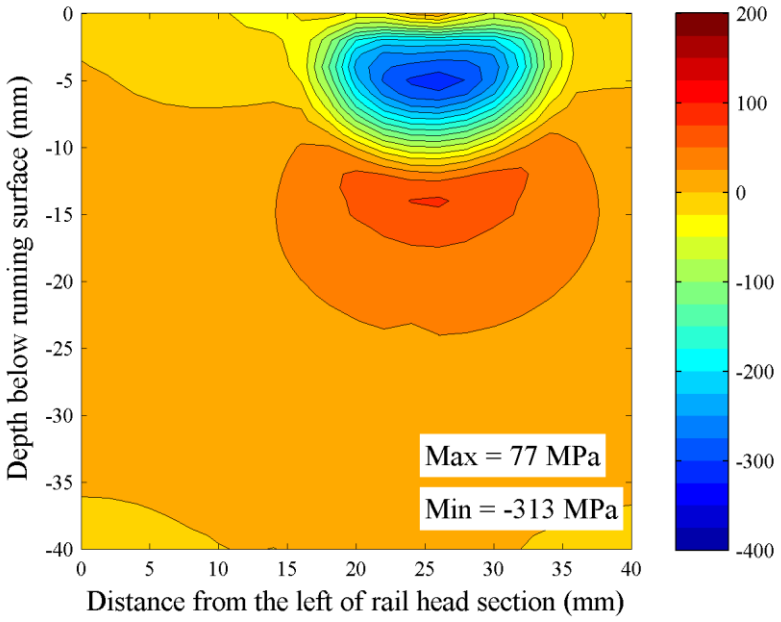

(a)

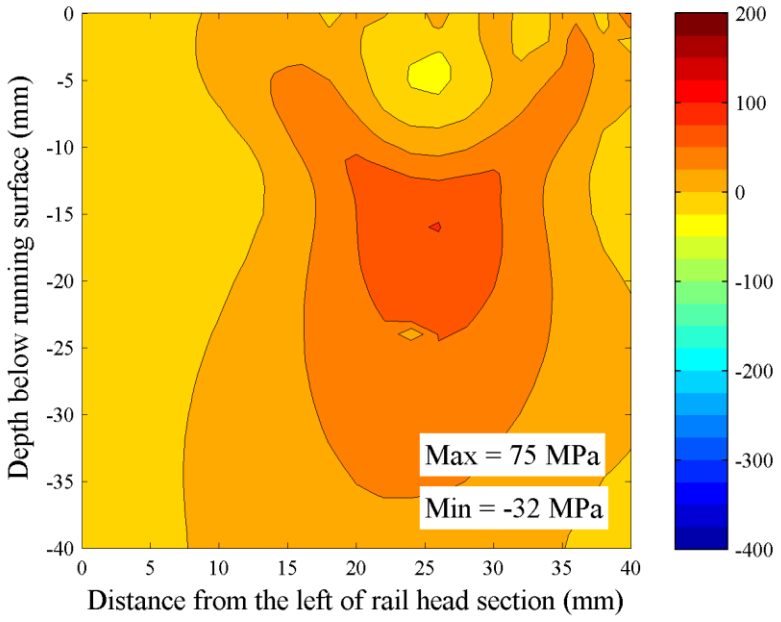

(b)

Fig. 2.13. Residual stress contours after five loading cycles with a 162 kN wheel load in: (a) longitudinal direction (Sxx), (b) vertical direction (Syy), and (c) transverse direction (Szz).

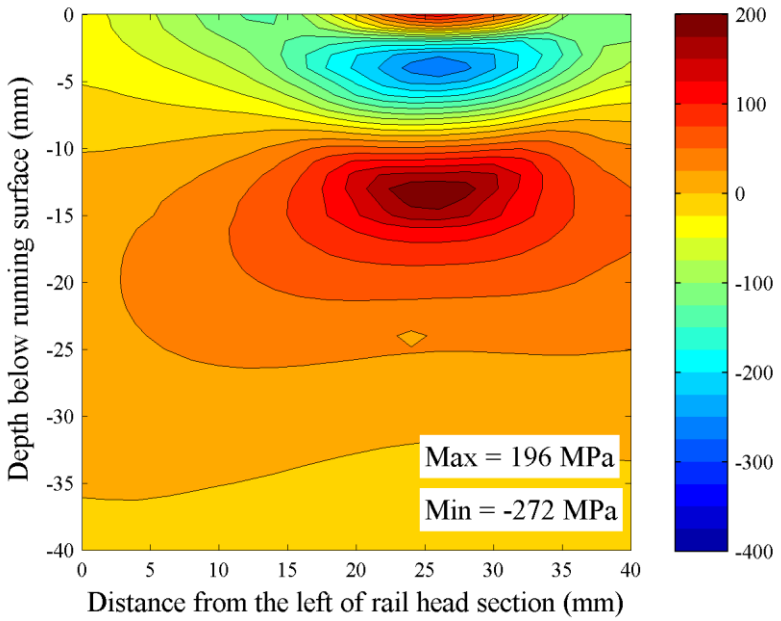

(c)

Fig. 2.13. Continued.

2.5.3 Comparisons between the Equivalent Rolling Stresses of Elastic and Hardening Materials

A comparison of von-Mises rolling stress contours at the cross section of interest in rail head, when the contact point is just right above, between the simulations with an elastic material and a hardening material at sixth loading cycle is shown in Fig. 2.14, in different scales. The equivalent rolling stress is localized near running surface with a peak value of 873 MPa for the elastic material. Stress gradually decreases as moving down further from running surface until stress diminishes to 100 MPa at 20 mm below running surface.

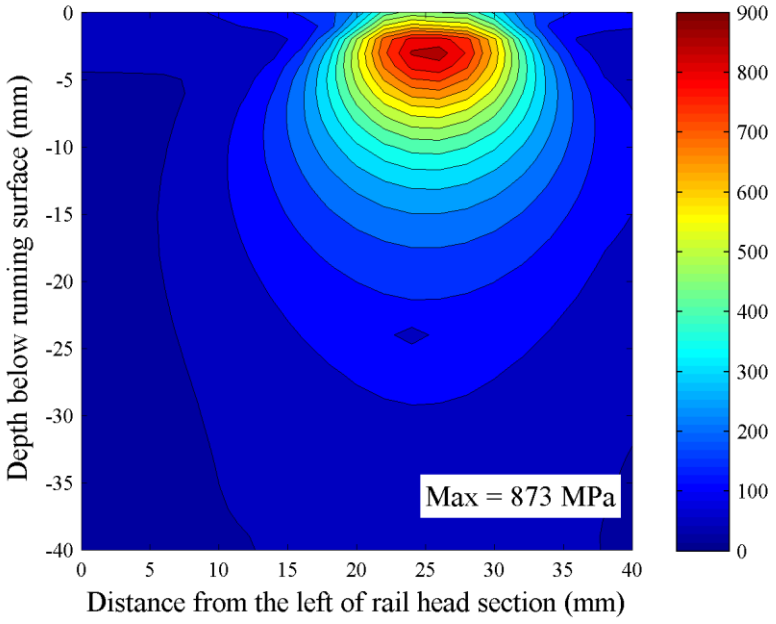

(a)

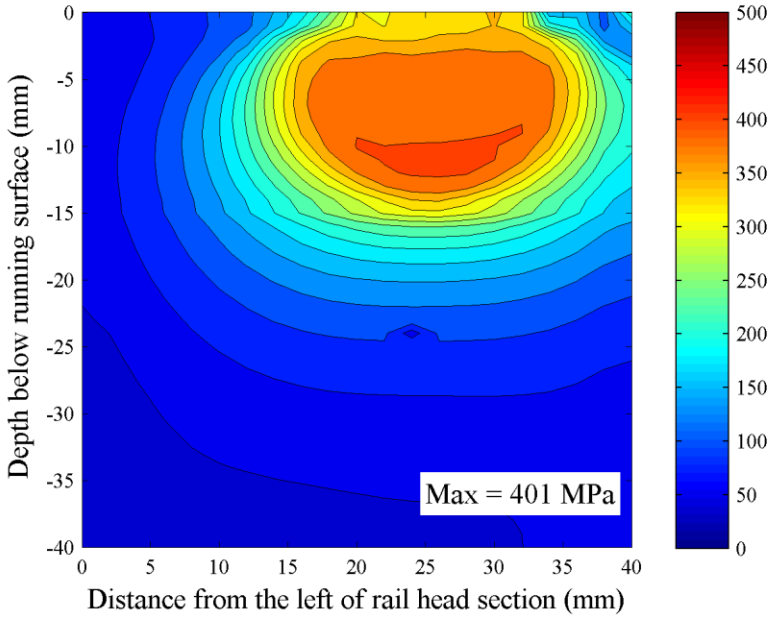

(b)

Fig. 2.14. von-Mises rolling stress contours (shown in different scales) for: (a) elastic material, and (b) hardening material at cycle#6.

With the Chaboche plasticity model, as the material near contact region is strain-hardened due to plastic deformation, residual stresses are built up throughout the rail head until reaching the steady state. Peak equivalent stress is observed at greater depth, about 12 mm from running surface with a smaller magnitude of 401 MPa. Another observation is that these residual stresses somehow help extend the region experiencing large equivalent rolling stress (350–400 MPa) to the depth of 15 mm below running surface throughout the center of rail head. This indicates less-localized state of damage in rail head, compared to the case with an elastic material.

From a simplified fatigue point of view, if von-Mises stress is regarded as a fatigue criterion, one can conclude that greater amount of material is found to experience damage when residual stresses are considered; therefore, there are greater tendency for subsurface fatigue cracks to nucleate. However, since von-Mises fatigue criterion tends to over-estimate fatigue life in non-proportional loading cases, it is preferable to use the critical plane fatigue criteria—stress-based or strain-based approaches—that account for failure mechanisms observed in fatigue tests of several types of steel. This will be studied in details in Chapters III and IV.

2.5.4 Comparisons between the Rolling Stresses of Elastic and Hardening Materials

Figures 2.15, 2.16, 2.17, and 2.18 present comparisons of rolling stresses—both normal and shear components— between the elastic and hardening cases, at four different depths: at 5 mm (node#235056), 13 mm (node#235083), 20 mm (node#234934), and 40 mm (node#235116) below running surface. Influences of

residual stresses in hardening material case are observed and will be discussed as that follows.

For the elastic material case, profiles of rolling stresses at various depths, in general, are similar, but different in magnitudes. Relatively large normal stress in the vertical direction and reversal of shear stress in the vertical plane are found in all levels of depth as predicted by an analytical solution from the Hertzian contact theory (Johnson [17]). Comments and observations are noted as that follows.

1. The longitudinal stress (Sxx) is highly compressive at near running surface. As moving further from the running surface, it is less compressive and is eventually tensile at depth of 40 mm.
2. The transverse stress (Szz) is compressive at 5 mm below running surface. It then turns to be tensile at depth greater than 13 mm with small changes in magnitude.
3. Most of normal stresses are compressive or little tensile; therefore, this elastic result suggests low chance of fatigue crack nucleation, which is encouraged by mean tensile stresses.

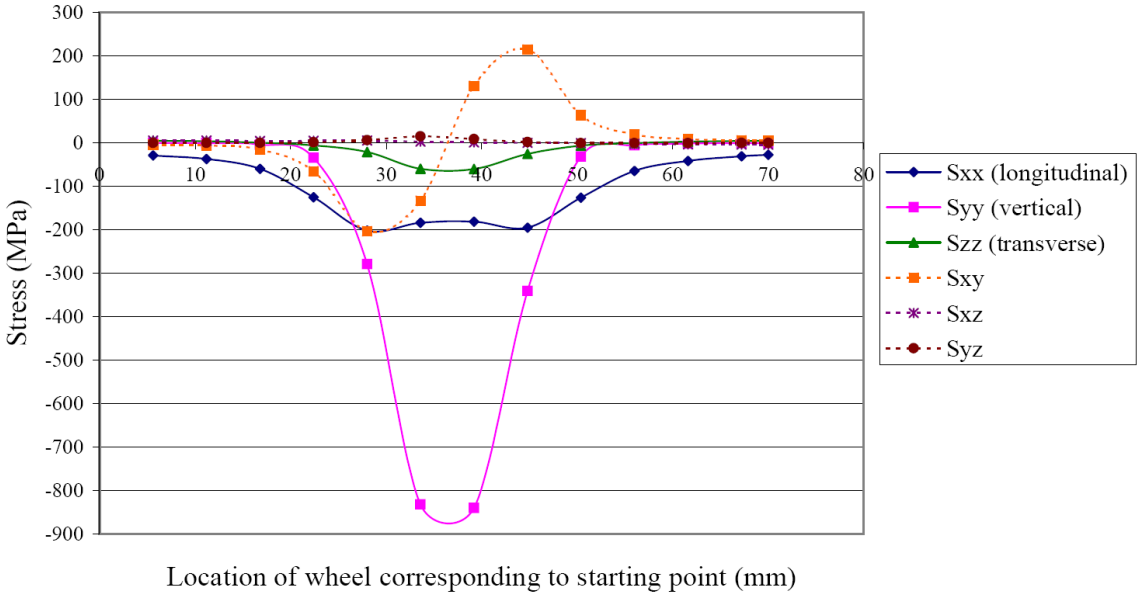

(a)

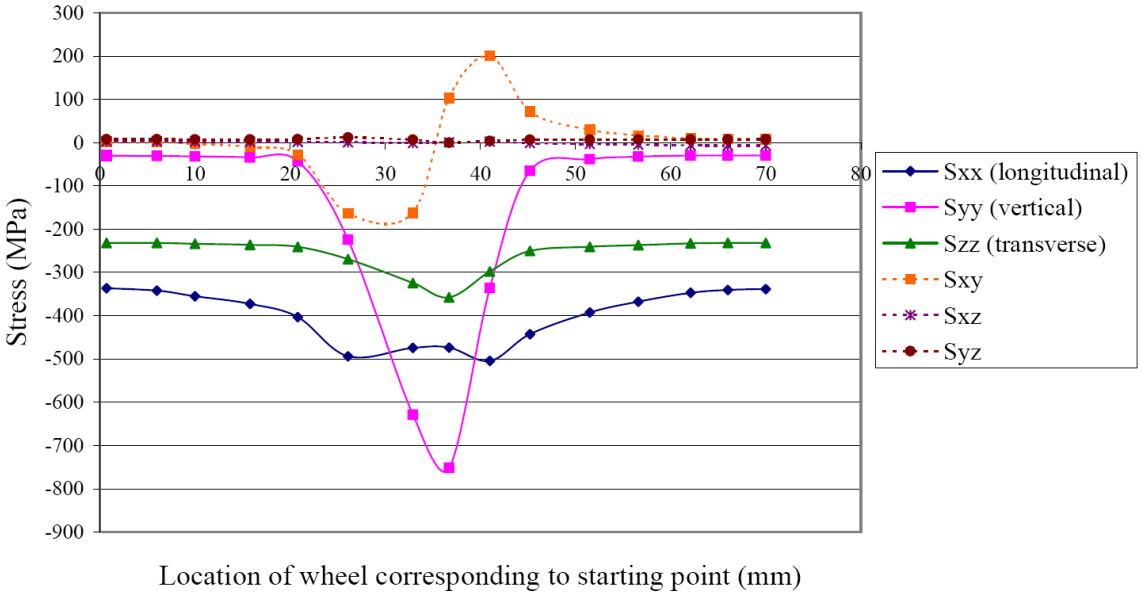

(b)

Fig. 2.15. Rolling stresses of a node located at 5 mm below running surface for: (a) elastic material, and (b) hardening material.

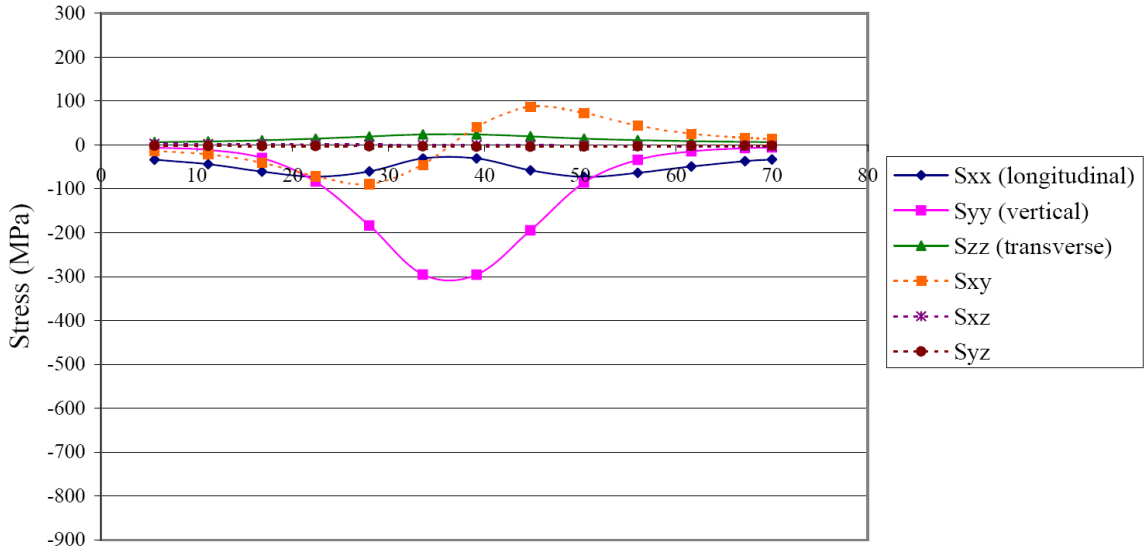

(a)

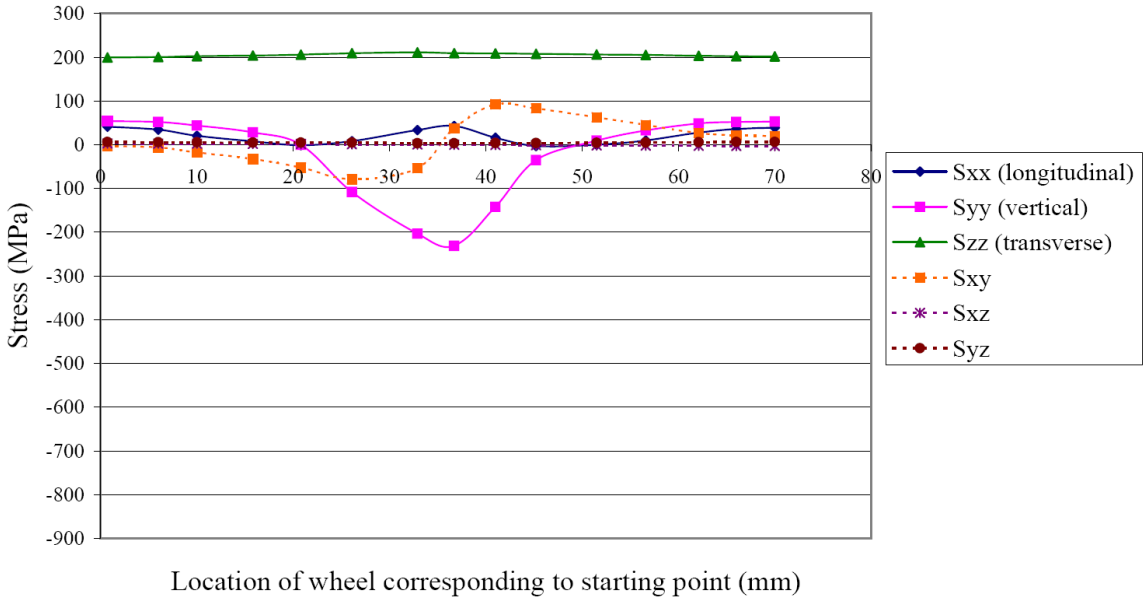

(b)

Fig. 2.16. Rolling stresses of a node located at 13 mm below running surface for: (a) elastic material, and (b) hardening material.

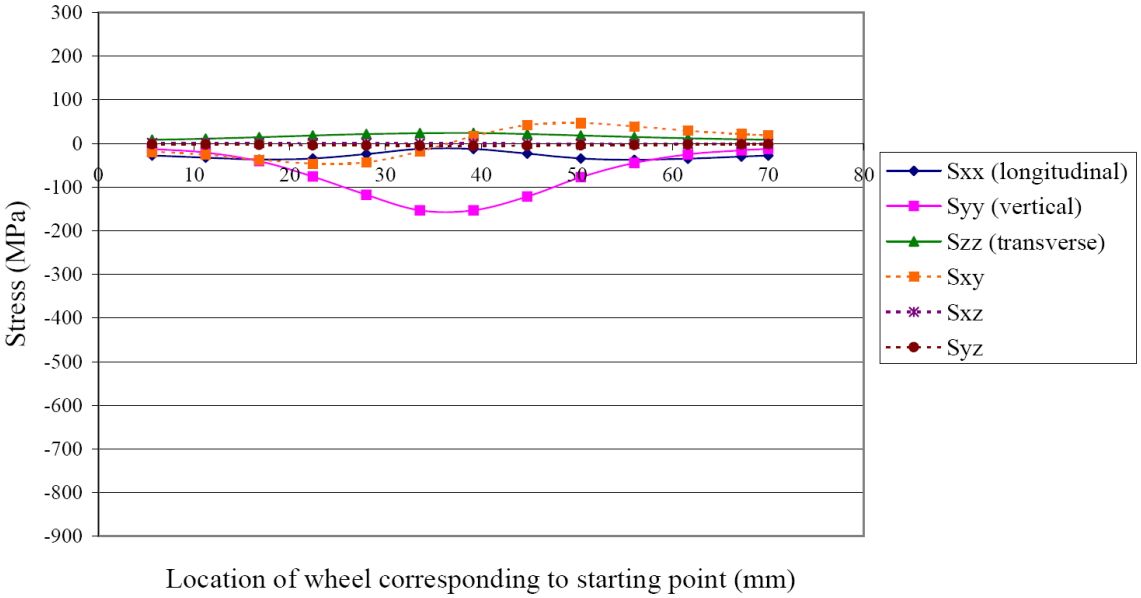

(a)

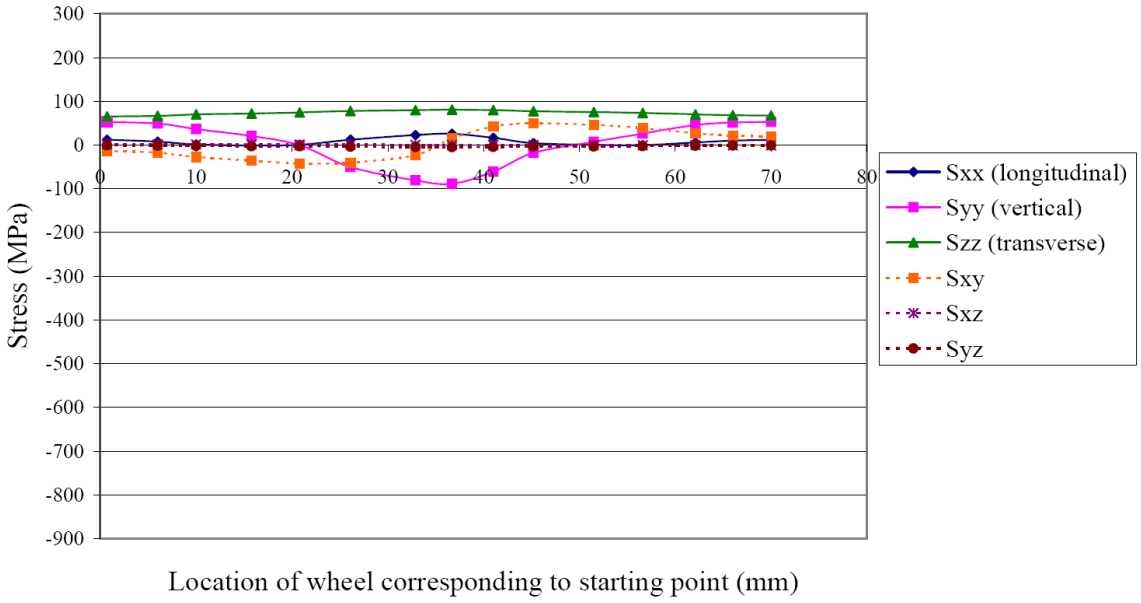

(b)

Fig. 2.17. Rolling stresses of a node located at 20 mm below running surface for: (a) elastic material, and (b) hardening material.

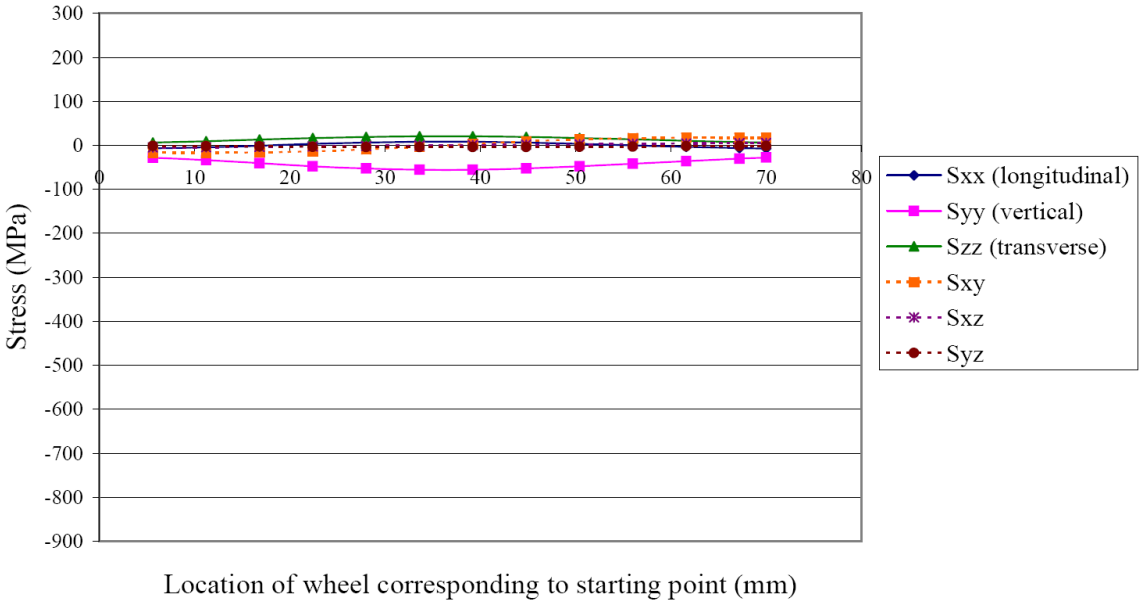

(a)

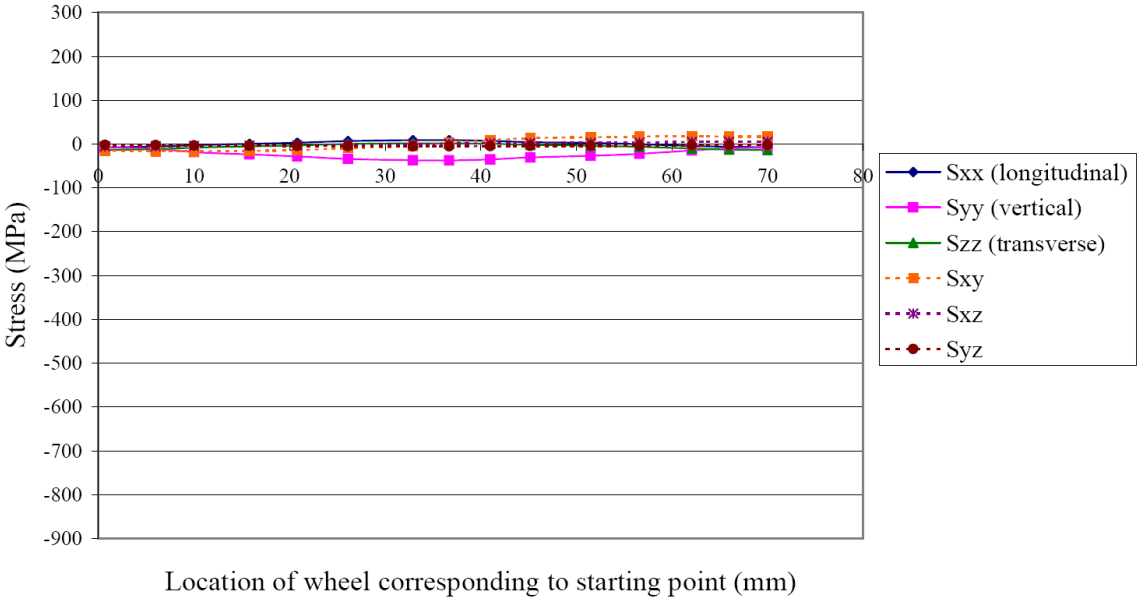

(b)

Fig. 2.18. Rolling stresses of a node located at 40 mm below running surface for: (a) elastic material, and (b) hardening material.

Observations on rolling stresses from a FEA of wheel-rail contact with hardening material compared against the result from the elastic material case are that follows.

- At 5 mm below running surface, the longitudinal (Sxx) and transverse (Szz) stresses are more compressive: changing from -200 to -500 MPa, and from -80 to -350 MPa respectively, due to the influence from the compressive residual stresses.
- At 13 mm below running surface, the transverse stress (Szz) is more tensile: changing from 20 to 200 MPa. The longitudinal stress (Sxx) and vertical stress (Syy) change from compression to tension during the rolling step. These make this region more susceptible to failure from high-cycle or low-cycle fatigue.
- At 20 mm below running surface, all normal stresses are more tensile, but the changes are not as much as those observed at lower depth.
- No significant changes of rolling stress at 40 mm below running surface.
- No significant changes of rolling shear stresses at all depths of interest.

2.5.5 Accumulation of Residual Strains in Rolling Contact

Other than low-cycle fatigue and high-cycle fatigue, at near running surface where material heavily deforms, ratcheting is also considered as a potential mode of damage in rolling contact. Ratcheting is defined as a continuous accumulation of strain in the direction of applied mean stress. As ratcheting progresses, it exhausts the ductility of material, leading to failure of that structure when total strain accumulation reaches critical limit. The nonlinear isotopic kinematic hardening rule—Chaboche plasticity

model—used in this study are optimized against results from a set of torsion- tension fatigue tests with mean stress in a rail steel that exhibits ratcheting with decaying rate.

For the 162 kN wheel load, Fig. 2.19 shows residual strains after five loading cycles of nodes vertically located right under the point of contact from depth of 0 to 40 mm. There are three components of residual strains: transverse (Strain-zz) and vertical (Strain-yy) components, and shear strain in the vertical plane (Strain-xy) that show significant accumulations at 0-10 mm below running surface. The vertical residual strain is compressive due to concentrated wheel load, as can be easily observed in field tests, and it is proportional to the amount of wheel load. As the top layer of rail is plastically deformed in compression by a vertically applied wheel load, this material layer tend to expand in lateral and longitudinal directions as a result of the Poission's effect. Constrained by boundary conditions at both rail ends, deformation in longitudinal direction is limited. In contrast, rail head is not restrained in the lateral direction; therefore, larger material expansion is found as observed in form of an accumulation of transverse residual strain.

As a driven wheel translates and rolls with friction to –x direction, the negative shear strain in the vertical plane (strain-xy) implies forward flow of material near running surface, meaning the material flow in the rolling direction. This qualitatively agrees with the results from rolling contact experiments done by Shima et al. [46] and Hamilton [47], and agrees with the semi-analytical solution done by Jiang and Sehitoglu [19].

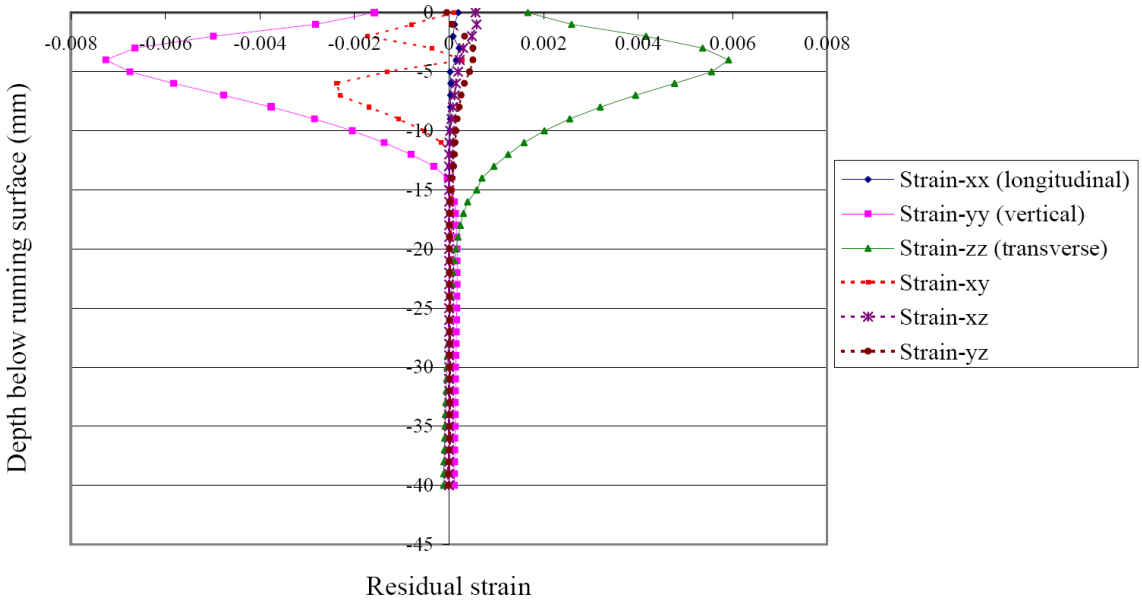

Fig. 2.19. Residual strain profiles accumulated in the nodes located vertically from the point of contact after five loading cycles for the 162 kN wheel load.

Fig. 2.20 shows the accumulation of vertical and transverse strains of the same node set as number of loading cycle increases from 1 to 5 for the 162 kN wheel load. Similar to the accumulation of residual stresses, though the parameters of the Chaboche plasticity model are optimized to a set of test data in which strain accumulation is still ongoing after 600 loading cycles, the change of vertical and transverse residual strains and shear residual strain in the vertical plane (strain-xy) from the simulation is found to be very small after 4 loading cycles. This implies a limitation of current plasticity model on the study of ratcheting in contact problems with compressive mean stresses. However, it is not known that the limitation is due to material model, optimization algorithm, or fatigue experiments. Further investigations should be done separately for this issue and will not be included in this study. Because ratcheting behavior could not

be predicted from this wheel-rail simulation, only high-cycle and low-cycle fatigue will be considered as the possible failure modes in fatigue analyses to be presented in the following chapters.

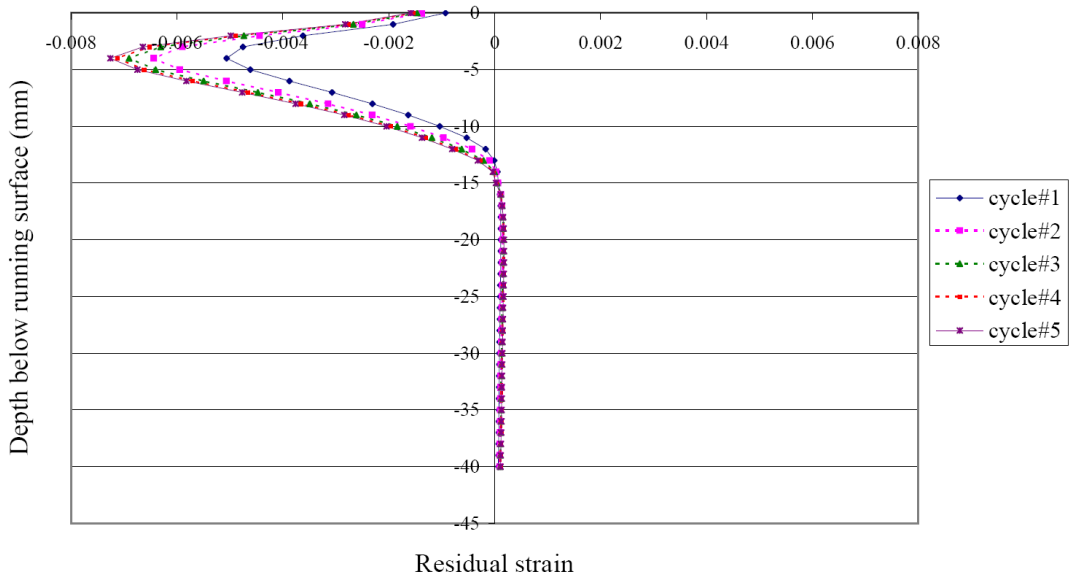

(a)

Fig. 2.20. Accumulation of strains from cycle#1 to 5 at the rail head due to a 162 kN wheel load for: (a) vertical residual strain, (b) transverse residual strain, and (c) shear residual strain in longitudinal plane.

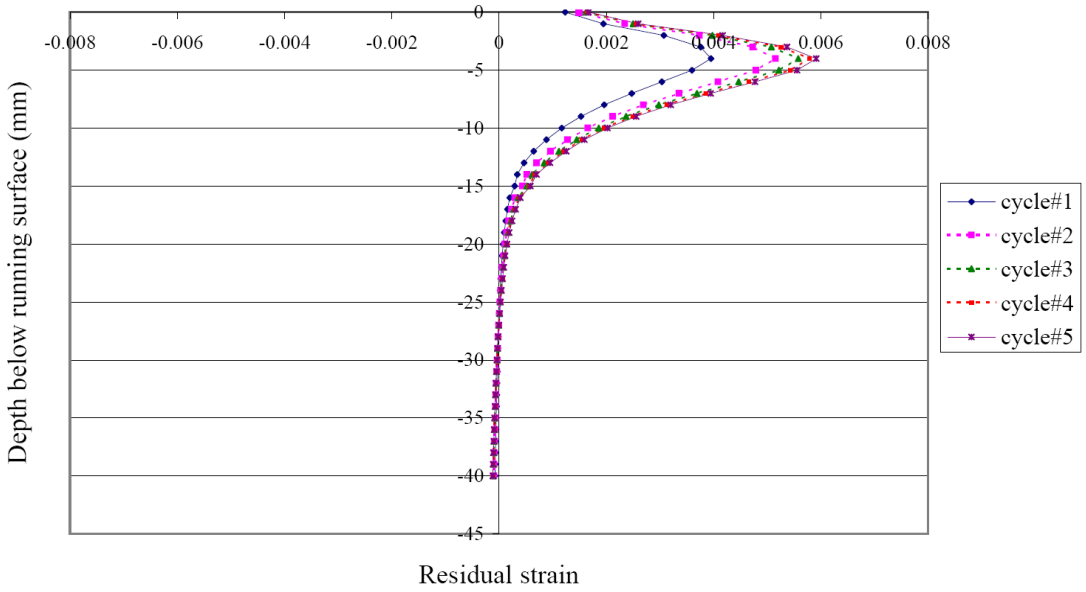

(b)

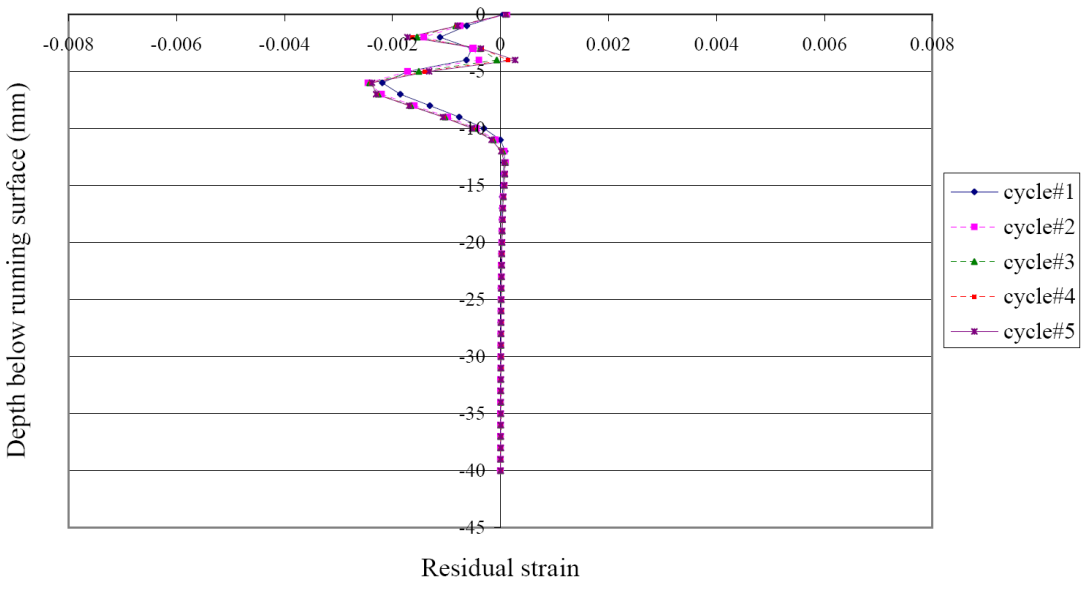

(c)

Fig. 2.20. Continued.

2.6 Conclusions

- Residual stresses reach the steady-state after five loading cycles, showing that the normal components of the residual stresses are compressive at 0-10 mm below running surface, while they are tensile at 10-40 mm below running surface. The accumulation of the residual shear stresses is relatively small.
- Profiles of the residual stresses predicted by the Chaboche plasticity model agree well with those from the measurement.
- If considering von-Mises equivalent stress as a fatigue criterion, fatigue damage in rail head is less localized and distributed to greater depth, suggesting possible fatigue crack nucleation sites at subsurface.
- Tensile residual stresses observed at subsurface tend to increase mean stress during rolling step; thus, provide better environment for cyclic fatigue.
- With current material hardening model, material ratcheting from rolling contact is not predicted. Only low-cycle and high-cycle fatigue are considered as possible modes of fatigue failure.

CHAPTER III

A STUDY OF RAIL HEAD FATIGUE DAMAGE WITH A STRESS-BASED CRITICAL PLANE CRITERION

3.1 Introduction

Presented in Chapter II for the 162 and 233 kN wheel load cases, the numerical results from a finite element model (FEM) of wheel-rail contact with the Chaboche plasticity model, show: 1) accumulation of compressive residual stresses at near running surface, 2) accumulation of residual strains at near running surface, 3) accumulation of tensile residual stresses and strains at 10 – 30 mm below the running surface, and 4) accumulation of residual stresses reaching the steady state after 5 loading cycles. These rolling stress and strain result will be used as an input for fatigue damage analyses in this chapter.

In general, rolling contact creates two types of fatigue cracks: surface and subsurface cracks. Surface cracks nucleate as a result of severe plastic deformation, strain accumulation, and high tractions near running surface, whereas the root cause of subsurface cracks, known to occur at 10 to 20 mm below running surface, are yet not clearly defined. Fry et al. [12] report a detrimental role of residual stresses on subsurface fatigue damages in the head of a thermite welded rail—for both one in perfect condition and one with imperfections. Compared to the case not considering effects from residual stresses, fatigue damage increases significantly at 15 – 20 mm below running surface when the residual stresses are included, which can be used to explain the subsurface

fatigue crack nucleation observed in field tests. Because strength and hardness of rail steels has been increased to meet the demand of heavy axle loads, railroad rails are more prone to behave in more brittle manner. As a result, as soon as subsurface cracks nucleate, it may take just a short period of time for the cracks to propagate and eventually break the rail. With fewer amounts of discontinuities or imperfections in typical pearlitic rail steels, a method to predict the nucleation of subsurface cracks in a rail head is essential for preventing unexpected failures that could result in derailments.

There are various methods to quantify fatigue damages in structures that experience multi-axial stress state, e.g. equivalent stress criteria and critical-plane criteria. The equivalent stress criteria, formulated the same way with von-Mises equivalent stress, are the simplest, but provide no information about the plane of crack nucleation. The critical-plane criteria, on the other hand, are formulated according to failure mechanisms observed in experiments that fatigue cracks tend to nucleate on a specific plane, depending on the type of materials. In this chapter, a stress-based critical plane fatigue criterion is chosen in order to study an influence of residual stresses on fatigue damage in a rail head due to rolling contact in term of *fatigue index*. The possible failure mechanisms will be discussed in term of the orientation of cracks: transverse, vertical, or horizontal planes, as previously defined in Fig. 2.9(b).

How deep from running surface should be investigated? The study of wheel-rail contact with a nonlinear isotropic kinematic hardening rule in Chapter II suggests that, with a typical 162 kN wheel load, the accumulation of residual stresses in the rail head due to rolling contacts is observed from 0– 40 mm below running surface. Therefore,

this study will focus on the rail head region at the depth of 0 to 40 mm below running surface. The rolling stresses at the sixth loading cycle in a tangent track, considering effects from residual stresses at the steady state, are used as an input for fatigue analyses of a pearlitic rail steel. Using a critical plane criterion, fatigue index varies among different planes. By searching over all planes, the location and plane of crack nucleation is the one that possesses largest damage.

3.2 Multi-axial Fatigue Criteria

3.2.1 Overview of Multi-axial Fatigue Criteria

Generally, fatigue damage phenomena consist of two main consecutive events: crack nucleation and early crack growth, and crack propagation (Bannantine et al. [48]). As a result, the total fatigue life of a component is the combination of life to crack nucleation and early crack growth, and life during crack propagation period, depending on type of loading and how material behaves. For high strength pearlitic rail steels, which are relatively brittle and usually resists large axle loads, crack nucleation and early crack growth period is considered to consume most of the service life of rails (Fry [3]), and it will be investigated through multi-axial fatigue criteria in this study. The life in crack propagation stage, which could be analyzed by fracture mechanics, is assumed to be minimal.

Due to multi-axial stress state of rolling contact, multi-axial fatigue criteria are proposed to determine fatigue life of components. Multi-axial fatigue criteria can be classified into three main approaches: stress-based, strain-based, and energy-based.

Garud [49] presents an extensive survey of history and early development of multi-axial fatigue criteria, covering all the three aforementioned approaches. He notes that the equivalent stress approach is convenient to apply, but it tends to overestimate fatigue life of components under non-proportional loading. More up-to-date reviews on multi-axial fatigue criteria are presentd by Socie and Marquis [50], Meggiolaro et al. [51], and Balthazar and Malcher [52]. A review, focusing on critical plane criteria, is also given by Karolczuk and Macha [53].

Another way to classify multi-axial fatigue criteria is by how fatigue damage—in term of fatigue index—is presented: as a scalar format or critical plane format. For the scalar format, stress or strain tensor histories are substituted in to fatigue criteria for a single number that represents equivalent fatigue damage, without providing information on crack orientations. The energy-based and equivalent stress/strain criteria are two examples of the scalar type. The critical plane format can be both the stress-based and strain-based types, depending on the behavior of materials of interest. Fatigue index is determined by transforming stress or strain histories into normal and shear components for all possible planes. The plane where fatigue index is largest is the critical plane, which indicates the direction that a crack would propagate to. The stress-based critical plane criterion, which is applied to study fatigue damage in rail head in this chapter, is reviewed in the next section.

3.2.2 Stress-Based Critical Plane Criteria

There are two major goals that a critical plane criterion is expected to perform: predicting the location and plane where cracks would nucleate, and predicting fatigue life of structures. The accuracy of critical plane determination relies mainly on how well a fatigue criterion is formulated according to crack nucleation and failure mechanisms, which could vary for different type of materials. For example, crack nucleation in brittle materials is more sensitive to normal stress than that in ductile materials. Hence, it is quite common that a fatigue criterion is more suitable to one material than another. At the same time, the proposed fatigue criteria must be able to correlate fatigue damage and fatigue life from a set of experiments that are performed with different loading configurations—uni-axial, biaxial, torsional, or bending—or with different state of stresses—proportional or non-proportional. Jiang et al. [54] present a study on the capability of some critical plane approaches to predict planes of failure and fatigue life in a structural steel (S460N). They show that even though those critical plane criteria are able to predict fatigue life accurately, the critical plane predictions from all methods deviate from experimental results in varying degrees. As material behavior and fatigue phenomena are stochastic by themselves, an application of critical plane criteria to different type of materials must be used with caution.

Based on observations from experimental results with typical structural steels, fatigue cracks tend to nucleate on the plane of maximum alternating shear stress, suggesting fatigue crack nucleation as a planar process. Findley [55] presents that tensile normal stress also has a damaging role on fatigue crack nucleation process, as it induces

separation of surfaces under alternating shear stress; thus, ease the movement of dislocations on that plane and promote early crack growth. In the same article, he introduces a stress-based critical plane criterion, in which the damage will occur on a plane where the combination of the shear stress amplitude and the factorized normal stress is largest. Note that in the Findley critical plane criterion, positive normal stresses (tensile) will assist crack nucleation process, while negative normal stresses (compressive) will do the opposite (Bannantine et al. [48] and Socie [14]).

The coefficient term used to factorize the influence of normal stress on the Findley fatigue criterion is called *normal coefficient* (κ) in this study. It is material-dependent and must be determined by a regression analysis of fatigue-life data from uni-axial and torsional fatigue tests, or from at least two tests with different type of loading. The normal coefficient reflects damage mechanism for different types of materials. For example, the case with $\kappa = 0$ (lower bound) implies a ductile failure mode, where the shear stress amplitude term is dominant. As the coefficient increases, the normal stress increasingly involves in crack nucleation and early growth; therefore, the Findley fatigue criterion represents failure in more brittle manner. Kaufman and Topper [56] suggest imposing an upper-bound of the influence of tensile normal stress; such that when a limit is reached, indicating full separation of surfaces under alternating shear stress amplitude, a further increase of tensile stress will have no effect on fatigue life.

Using a stress tensor history from wheel-rail simulation as an input for critical plane criteria, each plane of interest will possesses different amount of fatigue damage. The critical plane is where the fatigue index is largest. Crack nucleation is expected at

this location if the same loading configuration repeats. However, if loading configuration changes by times, the summation of fatigue index for each plane among different loading configurations will instead determine the crack nucleation and early growth. Based on experimental results by Hayhurst et al. [57] and McDowell et al. [58], Socie [14] reports no interaction between different damaged planes and suggests that fatigue index should be tracked for each plane independently for fatigue damage accumulation.

An application of Findley fatigue criterion on standing contact application is presented by Alfredsson and Olsson [59]. Among various multi-axial fatigue criteria, in overall, they find the Findley fatigue criterion to most agree with experimental results from standing contact tests. The normal coefficient (κ) is extracted from rotating-bending and torsion fatigue tests with case-hardened steel specimens, yielding the value of 0.675. Proper normal coefficient for Findley fatigue criterion in this study will be extracted from uni-axial, torsion-axial, and bending of various types of rail steel.

3.3 Fatigue Index Calculation

In rolling fatigue damage analyses, due to non-proportional loading behavior, it is preferable to describe the phenomena with multi-axial fatigue criteria, which consider effects of changing in direction of principal stresses. Findley fatigue criterion is the critical-plane-based and can be represented by the following equation.

$$f_{FIN} = \frac{\Delta \tau_{\max}}{2} + \kappa \sigma_n \tag{4}$$

where $\Delta\tau_{\max}$ is the maximum shear stress range during rolling step on the plane with largest Findley fatigue index

σ_n is the maximum normal stress during rolling step on the plane with largest Findley fatigue index

κ is the normal coefficient, which is an empirical material constant

f_{FIN} is the Findley fatigue index

The unit of Findley fatigue index is MPa, as is a stress. There is no conclusive agreement on proper value of κ, which could vary from 0.3 for ductile steels to 0.7 for brittle steels. In this study, fatigue index results for different values of κ will be investigated and checked against field results. The κ will be empirically determined later from various sources of fatigue test data of rail steels.

In order to find a plane where Findley fatigue index is largest, an exhaustive plane search using a spherical coordinate, shown in Fig. 3.1, is performed. However, to avoid an excessive computational time in both data processing and optimization of grinding schedules, plane search is done with 10 degree increment of theta (θ) and phi (φ). The normal vector that defines a plane can be written as follows.

$$\text{Normal vector: } \bar{n} = \begin{Bmatrix} n_1 \\ n_2 \\ n_3 \end{Bmatrix} = \begin{Bmatrix} \sin\theta\cos\varphi \\ \sin\theta\sin\varphi \\ \cos\theta \end{Bmatrix} \tag{5}$$

A stress tensor history at the sixth loading cycles, where residual stresses and strains are at steady-state, from Chapter II is used as an input for the fatigue analysis. Analyses of rolling contact consist of many consecutive time increments such that the

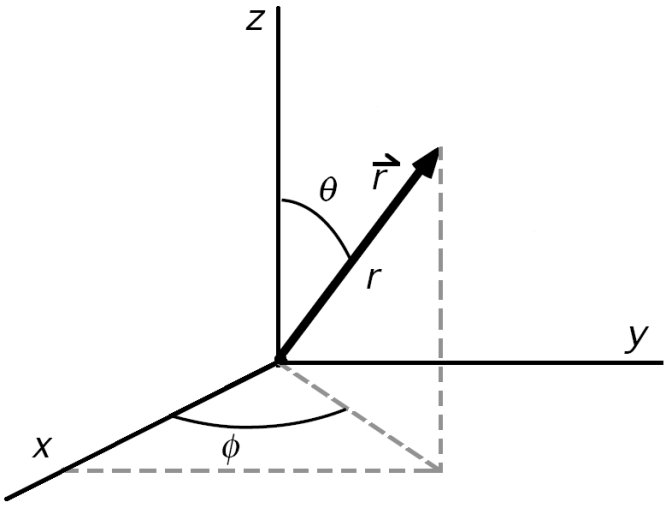

Fig. 3.1. The spherical coordinate.

state of stresses gradually changes while a wheel rolls over running surface of rail. Stress tensors at each node of interest are tracked and transformed into a stress vector $\overline{T}$, acting on the oblique plane of interest by the following transformation relations.

$$\overline{T} = n_1 T^1 + n_2 T^2 + n_3 T^3 \tag{6}$$

$$\overline{T} = n_1(\sigma_{11}e_1 + \sigma_{12}e_2 + \sigma_{13}e_3) + n_2(\sigma_{21}e_1 + \sigma_{22}e_2 + \sigma_{23}e_3) + n_3(\sigma_{31}e_1 + \sigma_{32}e_2 + \sigma_{33}e_3) \tag{7}$$

$$\overline{T} = e_1(\sigma_{11}n_1 + \sigma_{21}n_2 + \sigma_{31}n_3) + e_2(\sigma_{12}n_1 + \sigma_{22}n_2 + \sigma_{32}n_3) + e_3(\sigma_{13}n_1 + \sigma_{23}n_2 + \sigma_{33}n_3) \tag{8}$$

$$\overline{T} = e_1 T_1 + e_2 T_2 + e_3 T_3 \tag{9}$$

The stress vector is resolved into normal stress ($\overline{\sigma_n}$) and shear stress ($\bar{\tau}$) components by the following relations.

$$\left|\overline{\sigma_n}\right| = \bar{n} \bullet \overline{T} \tag{10}$$

$$\left|\overline{\sigma_n}\right| = n_1{}^2\sigma_{11} + n_2{}^2\sigma_{22} + n_3{}^2\sigma_{33} + 2n_1n_2\sigma_{12} + 2n_1n_3\sigma_{13} + 2n_2n_3\sigma_{23} \tag{11}$$

$$\overline{\sigma_n} = \left|\overline{\sigma_n}\right| \begin{Bmatrix} \sin\theta\cos\varphi \\ \sin\theta\sin\varphi \\ \cos\theta \end{Bmatrix} \tag{12}$$

$$\bar{\tau} = \overline{T} - \overline{\sigma_n} = \begin{Bmatrix} T_1 \\ T_2 \\ T_3 \end{Bmatrix} - \begin{Bmatrix} \sigma_n^1 \\ \sigma_n^2 \\ \sigma_n^3 \end{Bmatrix} \tag{13}$$

These stress transformations of the nodes of interest are performed for all time increments and all selected planes by a code written in Matlab®. The same procedure is also applicable to a transformation of strains when a strain-based critical plane criterion is used.

Parametric studies of the influence of wheel loads (162 and 233 kN) and normal coefficient (κ = 0 – 0.7) on fatigue index and location and critical plane of crack nucleation is reported for the representative cross-section of interest, located at the middle—35 mm from the starting point—of the 70 mm-long rolling path, as shown in Fig. 2.8(b). This is where a combined effect from global bending and rolling expected to be largest.

3.4 Results and Discussion

3.4.1 Fatigue Index of the 162 kN Wheel Load with Material Hardening

For each node on the cross-section of interest, Findley fatigue index is calculated from a stress tensor history at the sixth loading cycles for all possible planes. Among those planes, the largest indexes are reported in Fig. 3.2 to 3.5, with different κ for the

162 kN wheel load, as a fatigue index contour. As a result, it is not necessary that critical planes have to be the same for different nodes. The maximum and minimum fatigue indexes are reported within figures, when applicable. Note that, in this study, fatigue crack nucleation that occur within 0 - 5 mm below running surface is defined as a surface-type, while ones that locate at the depth greater than 5 mm are defined as a subsurface-type.

A site of crack nucleation is where Findley fatigue index is the largest. For $\kappa = 0$ (Fig. 3.2), meaning cracks are nucleated solely by shear stress amplitude component, the fatigue index contour is localized within 0-10 mm below running surface with the largest index of 212 MPa at about 3 mm below running surface. This suggests a possibility of surface fatigue crack nucleation. When the participation of normal stress on damage mechanism increases, as κ increases from 0 to 0.3, 0.5, and 0.7, Fig. 3.3, 3.4, and 3.5 show the corresponding fatigue index contours. Another possible crack nucleation site is predicted at 13 mm below running surface, where tensile residual stresses from rolling contact, shown in Fig. 2.11, is the largest. This implies an important role of normal stress, strongly influenced by residual stresses, on subsurface fatigue crack nucleation.

Accounting for residual stresses, the more the participation of normal stress on fatigue damage mechanism, the more damaging the rail head at greater depth below running surface is. For example, in the case of $\kappa = 0.3$, the fatigue index at near surface is twice as much as that found at subsurface; whereas in the case of $\kappa = 0.7$, the fatigue indexes found at near running surface and subsurface are comparable. It should be noted that peak value of fatigue index at near surface slightly decreases as κ increases.

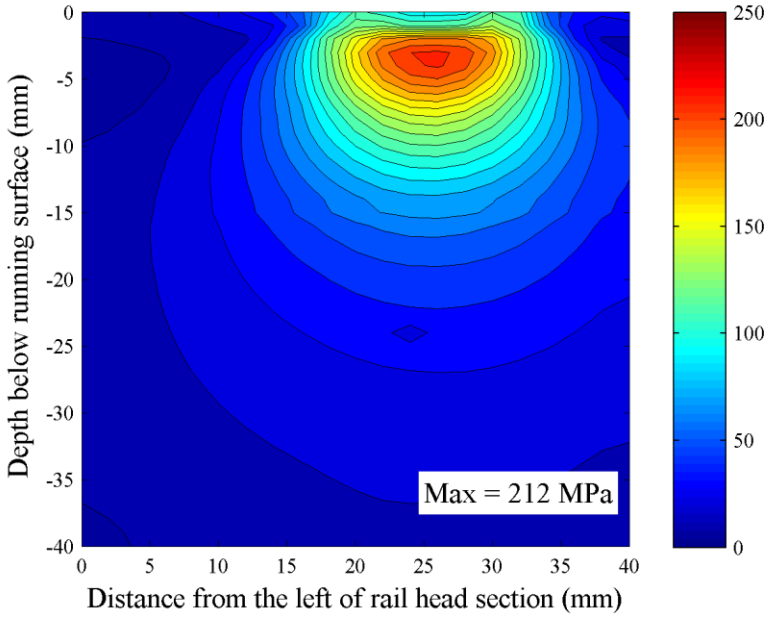

Fig. 3.2. Maximum Findley fatigue index contour ($\kappa = 0$) of the 162 kN wheel load at the sixth loading cycle by searching selected plane at all nodes.

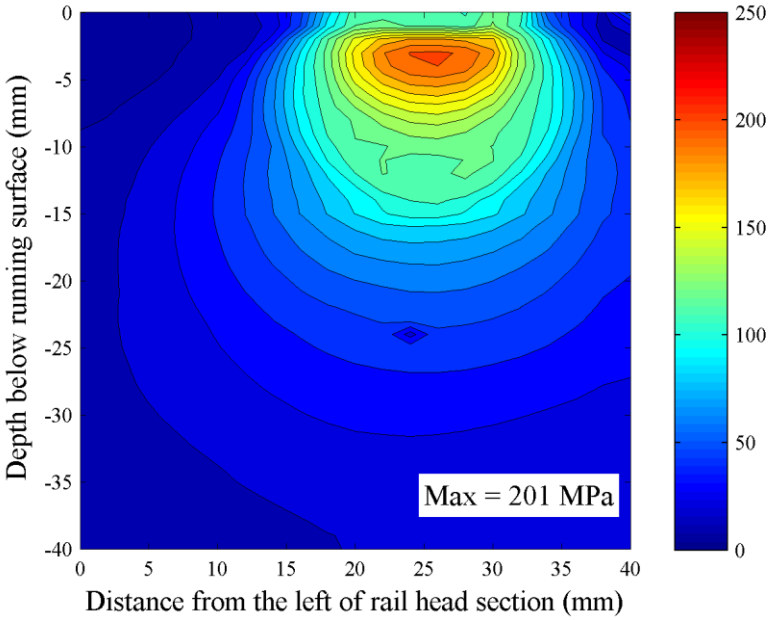

Fig. 3.3. Maximum Findley fatigue index contour ($\kappa = 0.3$) of the 162 kN wheel load at the sixth loading cycle by searching selected plane at all nodes.

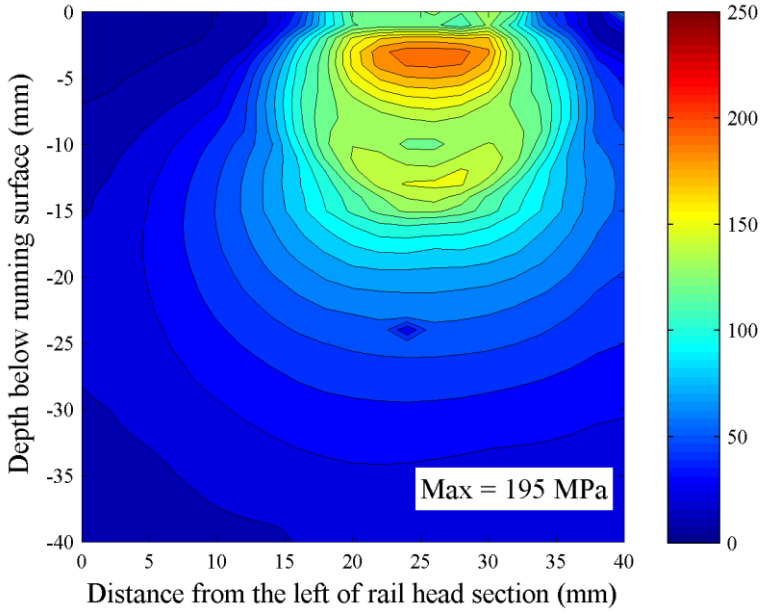

Fig. 3.4. Maximum Findley fatigue index contour (κ = 0.5) of the 162 kN wheel load at the sixth loading cycle by searching selected plane at all nodes.

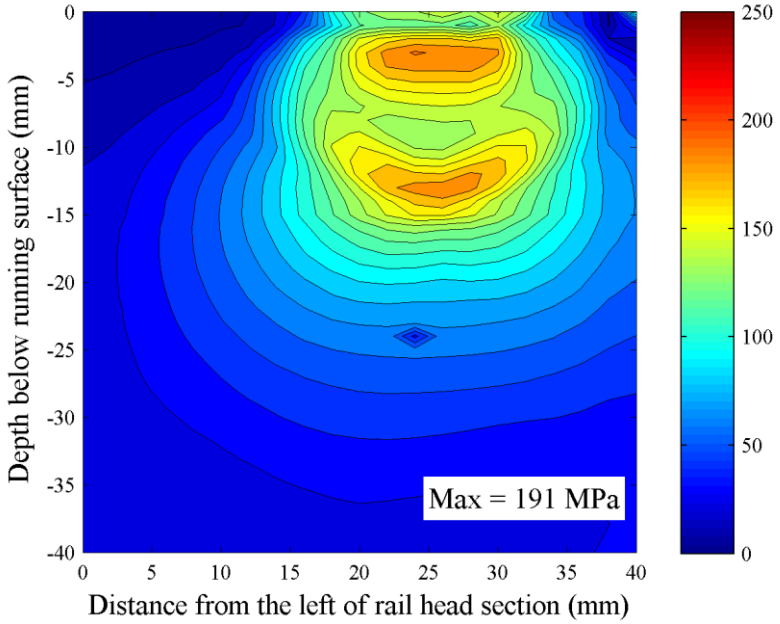

Fig. 3.5. Maximum Findley fatigue index contour (κ = 0.7) of the 162 kN wheel load at the sixth loading cycle by searching selected plane at all nodes.

The direction cosines of critical planes, approximated cracking planes, and the corresponding fatigue indexes of possible crack nucleation sites for all cases are summarized in Table 3.1. Defined in Fig 2.9(b) in Chapter II for the wheel-rail model in this study, x-axis coincides with the longitudinal direction of a rail, while y-axis and z-axis coincide with the vertical and transverse directions respectively. The predicted critical planes of the surface cracks for all values of κ approximately coincide with the horizontal plane, where surface shelling is usually developed in field observations (Sperry Rail Service [2]). For subsurface cracks, which are evident only in the case of κ = 0.5 and 0.7, the three largest fatigue indexes are reported to represent a relatively large damage distribution at subsurface. All critical plane predictions are qualitatively similar; it is a mixed cracking mode between the vertical and horizontal planes, similar to what defined as longitudinal cracks in field observations (Sperry Rail Service [2]). Further study on fatigue damage and critical plane in heavier wheel loads will be discussed in the next section.

Table 3.1

Summary of possible fatigue crack nucleation sites and cracking planes for the 162 kN wheel load with material hardening (Findley fatigue criterion).

Normal coefficient	Node #	Fatigue index (MPa)	Depth below running surface (mm)	Unit normal vector of critical plane			Cracking plane
				x	y	z	
0	235063	212	3	0.3420	0.9397	0.0000	Horizontal
0.3	235063	202	3	0.1736	0.9848	0.0000	Horizontal
0.5	235043	196	3	0.1736	0.9848	0.0000	Horizontal
	235083	152	13	0.0868	0.4924	0.8660	V-H*
0.7	235043	191	3	0.1710	0.9698	0.1736	Horizontal
	235083	187	13	0.0868	0.4924	0.8660	V-H*

*V-H: A mixed cracking plane between the vertical and horizontal planes, where the leading term—V— indicates the cracking plane is more inclined toward the vertical plane.

3.4.2 Fatigue Index of the 162 kN Wheel Load with an Elastic Material

Using the elastic rolling stress result from Chapter II as an input for fatigue analyses, in contrast to the case with material hardening, most part of fatigue index contours remain unchanged as κ increase from 0.3 to 0.7 as shown in Fig. 3.6 and 3.7. The contours of fatigue index are localized within 0 - 10 mm below running surface with the largest index of 259 MPa at about 3 mm below running surface in both cases. No subsurface crack nucleation is predicted. In term of subsurface fatigue crack nucleation, this indicates a strong influence of residual stresses, which are largely tensile at 10 - 30

mm below running surface, on the distribution of fatigue index to greater depth that could result in subsurface crack nucleation in some cases.

Not only that a simplified wheel-rail simulation with an elastic material would give unrealistic rolling stress results, neglecting residual stresses that are observed in measurements may also affects the prediction of fatigue damage in a rail head. This, as well, raises a concern on the importance of plasticity model to a simulation of residual stresses in rolling contact. However, for typical pearlitic rail steel, the participation of the normal stress on fatigue damage is still unknown, and a proper value or a range of κ will be determined from fatigue tests with various type of loading at the end of this chapter.

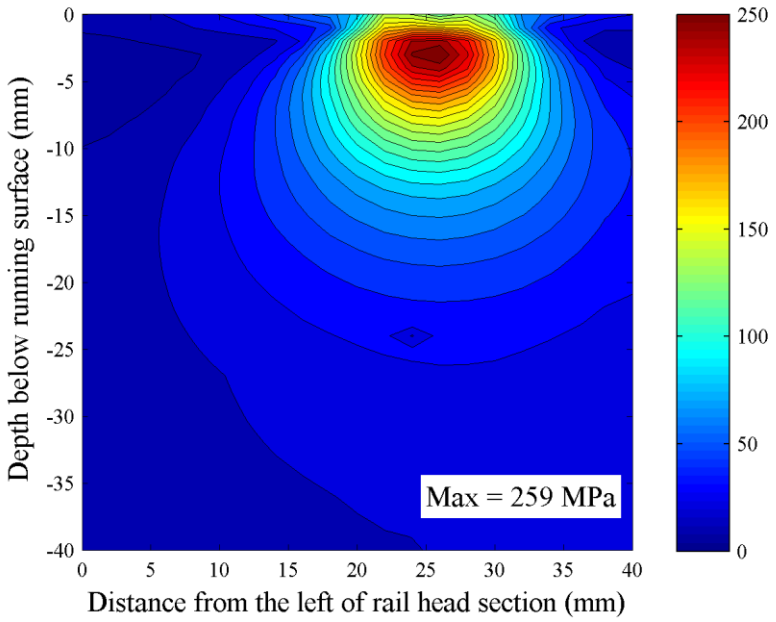

Fig. 3.6. Maximum Findley fatigue index contour (κ = 0.3) of the 162 kN wheel load with elastic material by searching selected plane at all nodes.

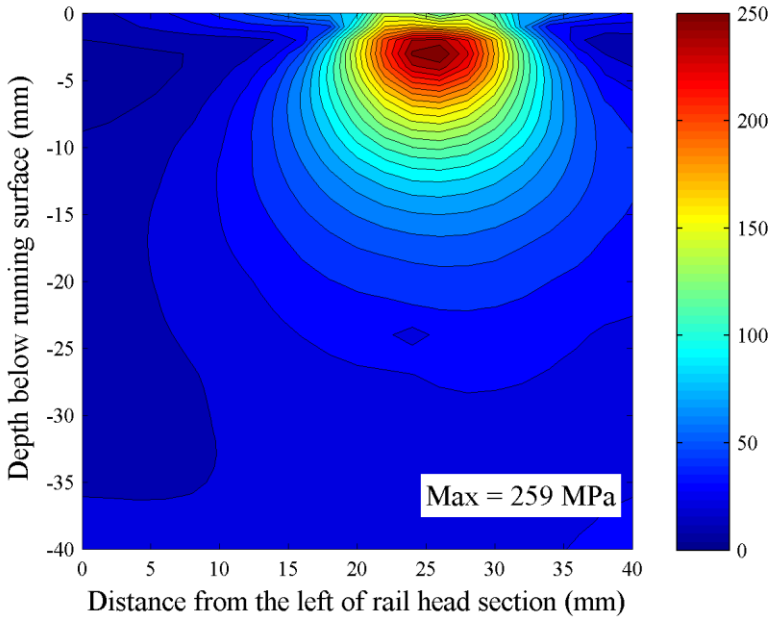

Fig. 3.7. Maximum Findley fatigue index contour (κ = 0.7) of the 162 kN wheel load with elastic material by searching selected plane at all nodes.

3.4.3 Fatigue Index of the 233 kN Wheel Load with Material Hardening

Fig. 3.8, 3.9, and 3.10 are fatigue index contours occurred during the sixth cycle of a rolling contact of the 233 wheel load as κ equals to 0.3, 0.5, and 0.7 respectively. In all cases, the fatigue crack nucleation sites found near the running surface are located at about the same depth—4 mm below running surface—with decreasing peak values as κ increases. Branching of fatigue index contours to greater depth, about 16 mm below running surface, is clearly observed in all cases, and it is more evident as κ increases. As a result, there occurs another possible crack nucleation site at subsurface, where the peak fatigue index is competitive, or even greater for κ = 0.7, to that at near running surface for κ = 0.5. Unlike the results from the 162 kN wheel load case, the fatigue

index contour at subsurface is more evident and clearly separated from that at near running surface.

The direction cosines of critical planes, approximated cracking planes, and corresponding fatigue indexes of possible crack nucleation sites for all cases are summarized in Table 3.2. The results are qualitatively similar to those from the 162 kN wheel load case. The critical planes of surface cracks for all values of κ approximately coincide with the horizontal plane, where surface shelling is usually developed in field observation. For subsurface cracks, the critical planes are a mixed mode between vertical and horizontal planes, where a longitudinal crack may occur.

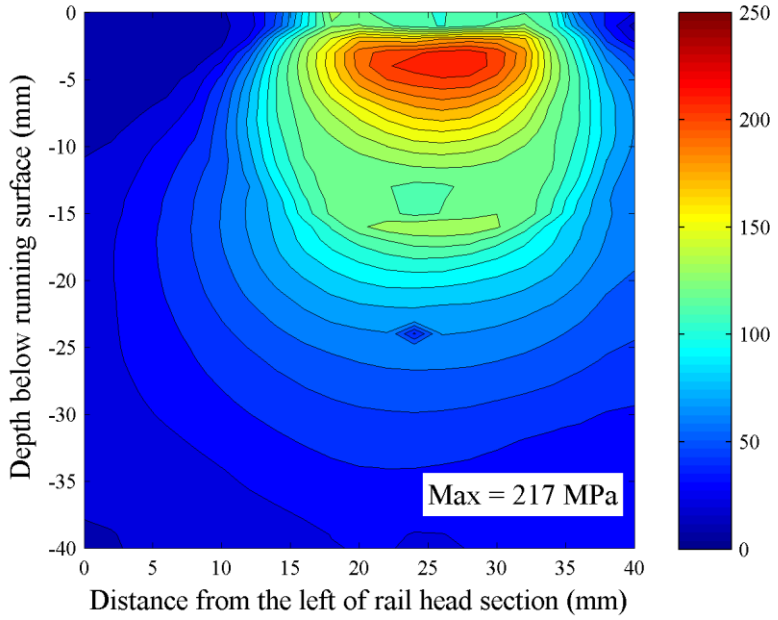

Fig. 3.8. Maximum Findley fatigue index contour (κ = 0.3) of the 233 kN wheel load at the sixth loading cycle by searching selected plane at all nodes.

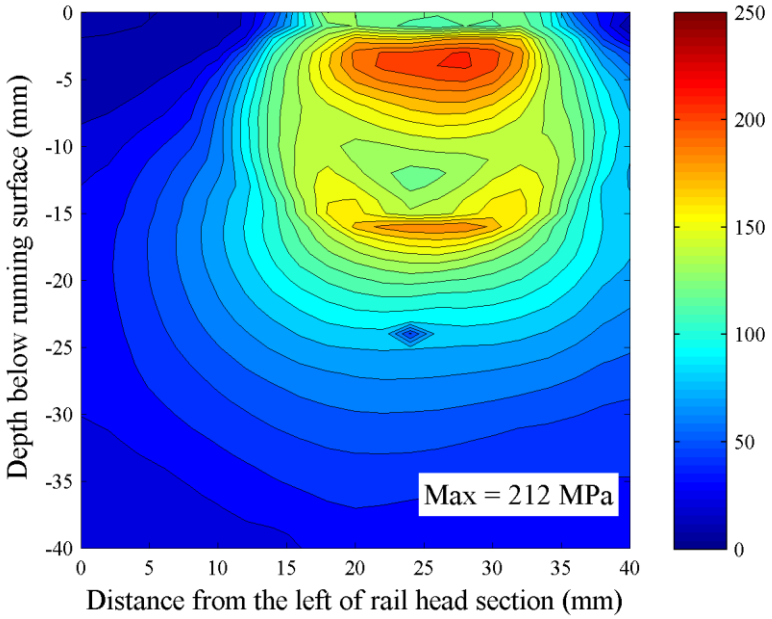

Fig. 3.9. Maximum Findley fatigue index contour (κ = 0.5) of the 233 kN wheel load at the sixth loading cycle by searching selected plane at all nodes.

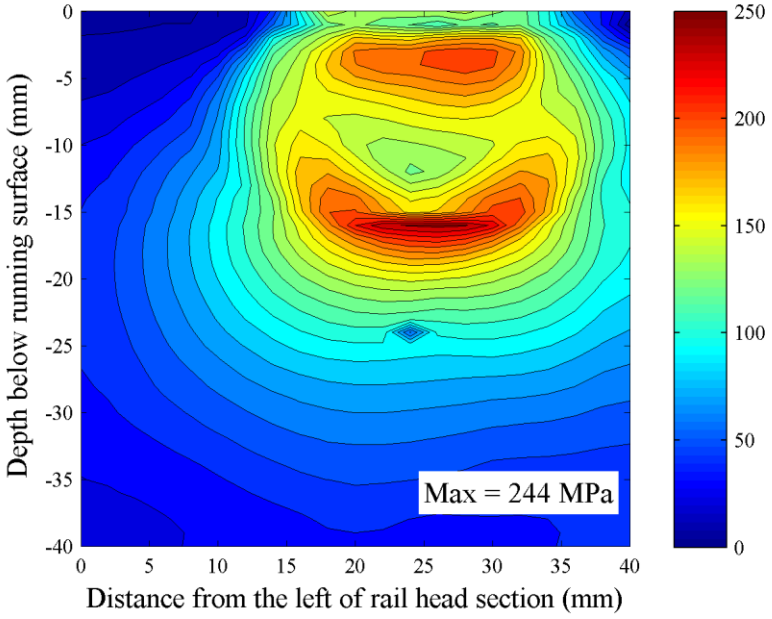

Fig. 3.10. Maximum Findley fatigue index contour (κ = 0.7) of the 233 kN wheel load at the sixth loading cycle by searching selected plane at all nodes.

Table 3.2

Summary of possible fatigue crack nucleation sites and cracking planes for the 233 kN wheel load with material hardening (Findley fatigue criterion).

Normal coefficient	Node #	Fatigue index (MPa)	Depth below running surface (mm)	Unit normal vector of critical plane			Cracking plane
				x	y	z	
0.3	235053	217	4	0.1736	0.9848	0.0000	Horizontal
	234940	139	16	0.0000	0.5000	0.8660	V-H*
0.5	235052	212	4	0.1736	0.9848	0.0000	Horizontal
	234940	188	16	0.1710	0.4698	0.8660	V-H*
0.7	235052	207	4	0.1736	0.9848	0.0000	Horizontal
	234940	244	16	0.1170	0.3214	0.9397	V-H*

*V-H: A mixed cracking plane between the vertical and horizontal planes, where the leading term—V—indicates the cracking plane is more inclined toward the vertical plane.

3.4.4 Comparisons between Fatigue Indexes of the 162 kN and 233 kN Wheel Loads with Material Hardening

The influence of wheel loads, comparing between the 162 kN and 233kN wheel loads, on fatigue indexes in a rail head is clearly observed in all cases; roughly, fatigue index is proportional to wheel load. The area coverage of fatigue index contours and peak fatigue indexes are greater as wheel load increases to 233 kN for both near-surface and subsurface regimes, meaning more fatigue damage in the rail head. Because the changes of fatigue index contours for different values of κ are qualitatively the same, only the case of κ = 0.5, shown in Fig. 3.4 and Fig. 3.9, are discussed. As wheel load

increases from 162 to 233 kN, the fatigue crack nucleation sites found at near running surface move to greater depth, from 3 to 4 mm below running surface.

Similarly, as wheel load increases from 162 to 233 kN, subsurface fatigue crack nucleates at greater depth, increasing from 13 to 16 mm, which coincides with the depth where tensile residual stresses from rolling contact with 233 kN wheel load, presented in Chapter II, is largest. The corresponding peak fatigue index also increases. Unlike the case of 162 kN wheel load, the peak value of subsurface fatigue index for the 233 kN wheel load is more comparable to that found at near running surface. This is due to a greater increase of tensile residual stresses (at subsurface) compared to the increase of compressive residual stresses (at near surface), as wheel load increases from 162 to 233 kN. The critical plane predictions of possible crack sites, at both near surface and subsurface, are slightly different for both wheel loads. Approximately, surface fatigue cracks will nucleate along the horizontal plane, and subsurface fatigue cracks will form along the resultant plane between the vertical and horizontal planes.

In conclusion, an increase of wheel load would increase fatigue index in rail head in overall, but not uniformly. The increase of fatigue index at subsurface would be more pronounced.

3.4.5 Influence of Shear Stress Amplitude and Normal Stress Components on Findley Fatigue Index

A study of mechanisms of surface and subsurface fatigue crack nucleation within a rail head is presented in this section. Decomposing the Findley fatigue criterion into two components—a shear stress amplitude term and a factorized normal stress term, Fig. 3.11, again, presents a Findley fatigue index contour of the 162 kN wheel load (κ = 0.3) during the sixth loading cycles, along with its corresponding contours of shear stress amplitude and factorized normal stress. By adding node-by-node results of Fig. 3.11(b) and 3.11(c)—the shear stress amplitude and factorized normal stress contours, the contour of resultant Findley fatigue index is presented in Fig. 3.11(a). Also, note that it is reported in different scale from the one previously shown.

Comparing these three contours, the surface crack nucleation site agrees with the shear stress amplitude contour, while the subsurface crack nucleation is promoted by both shear stress amplitude and normal stress. A conclusion of fatigue damage mechanism in a rail head according to the Findley fatigue criterion is that follows.

- Shear stress amplitude component dominates crack nucleation and early growth at near surface, due to large tractive forces at near wheel-rail interface.
- Both shear stress amplitude and normal stress promote crack nucleation and early growth at subsurface—13 mm below running surface in this case—partly due to an influence from tensile residual stresses in this region.

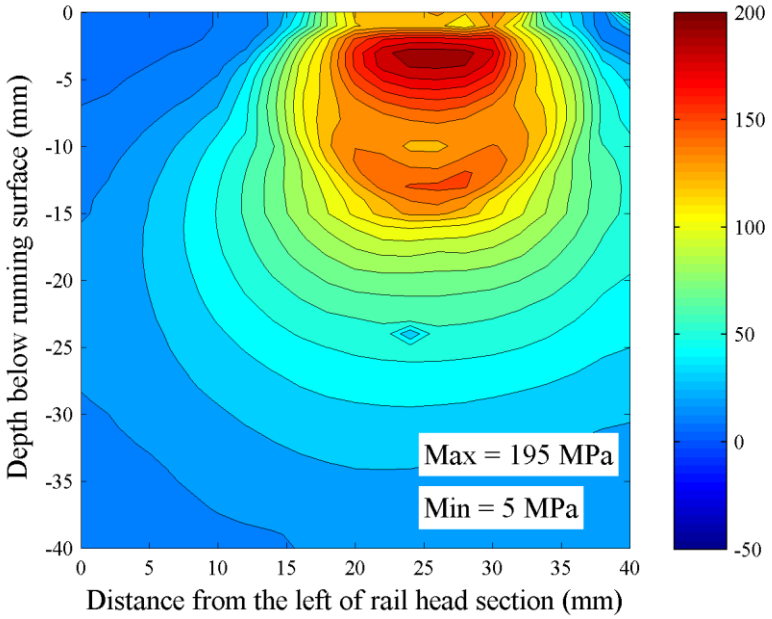

(a)

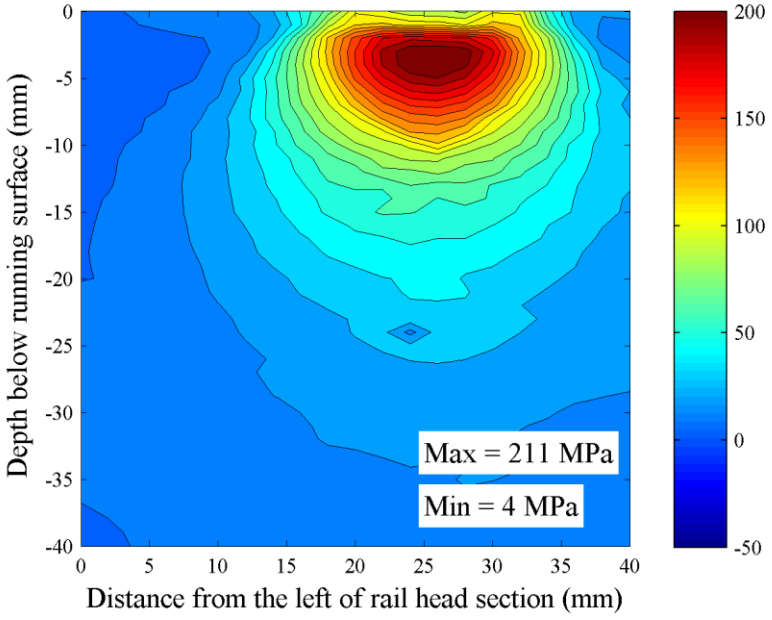

(b)

Fig. 3.11. Contours of (a) Findley fatigue index, (b) shear stress amplitude component, and (c) normal stress component, of the 162 kN wheel load (κ = 0.5) at the sixth loading cycle.

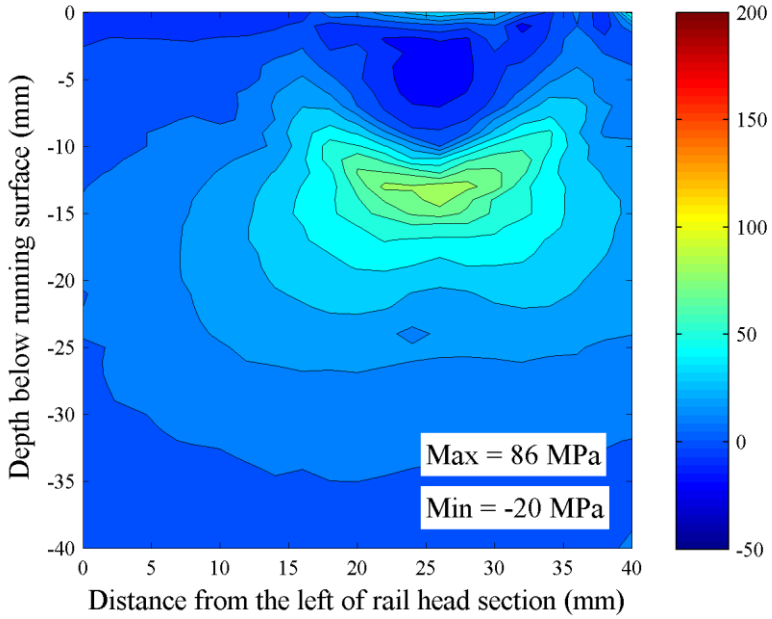

(c)

Fig. 3.11. Continued.

Fig. 3.12 and 3.13 represent two extremes of Findley fatigue criterion: the pure shear mode (κ = 0) and the pure tensile mode (κ = 1 and neglecting the shear stress amplitude term) respectively. Assuming rail steels or rail heads made of a material with high ductility, which failure mechanism is solely dominated by shear stress, it is likely that surface cracks would nucleate as shown in Fig. 3.12.

In contrast, if rail steels or rail heads with high hardness behave in brittle manner, failure mechanisms are dominated by the normal stress component instead, resulting in subsurface crack nucleation as shown in Fig. 3.13. This implies that a strategy of wear rate reduction by improving material hardness must be exercised with caution, as it may

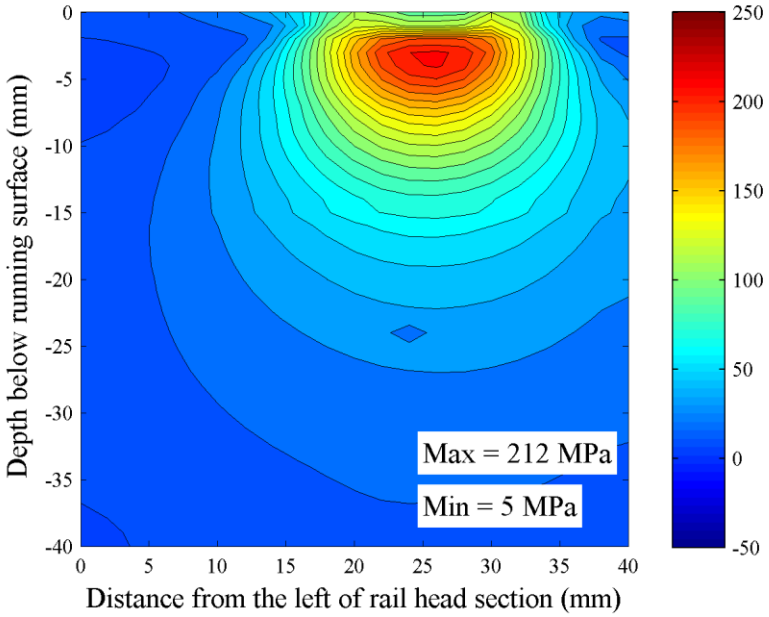

Fig. 3.12. Maximum shear stress amplitude contour of the 162 kN wheel load at the sixth loading cycle by searching selected plane at all nodes.

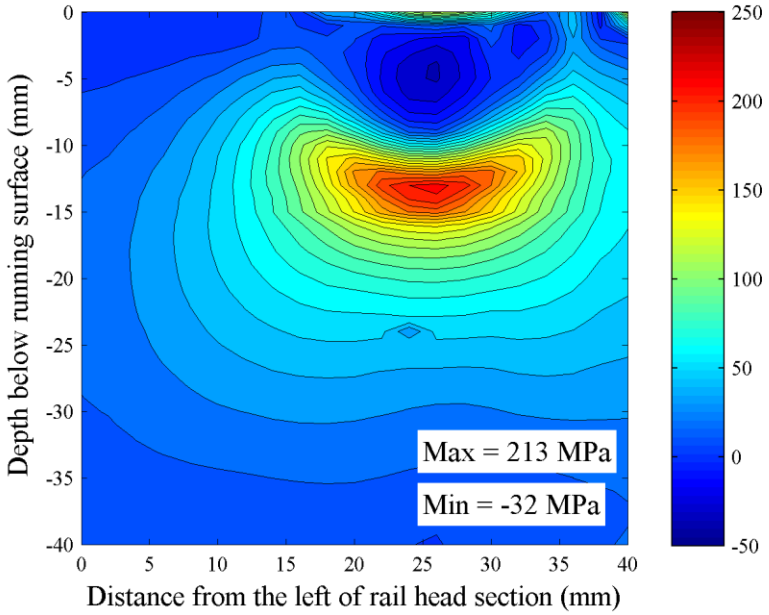

Fig. 3.13. Maximum normal stress contour of the 162 kN wheel load at the sixth loading cycle by searching selected plane at all nodes.

promote the nucleation of subsurface crack unintentionally. However, this, in turn, will mitigate the nucleation of surface cracks.

3.4.6 Evaluation of κ for a Pearlitic Rail Steel

All discussions made prior to this section are based on general fatigue and mechanical behaviors of a metallic material. The predicted rolling stress results include effects from material hardening through the formation of residual stresses, but do not represent effects from implicit material behaviors, such as hardness and variation of strength across a rail cross-section. As discussed in 3.4.1 to 3.4.5, the nucleation of subsurface cracks heavily depends on the participation of normal stress component, defined through κ, in the Findley fatigue criterion. The greater the κ, the more brittle the rail head, and the greater the fatigue index at subsurface is, which, cumulatively, may cause subsurface cracks in long term.

The value of κ that represents fatigue behavior of a rail steel can be determined from a regression analysis of Findley fatigue index and fatigue life data of various loading configurations: uni-axial, torsion-axial, and bending, for rail steel. The proper value of κ is the one that gives the best linear fitting of a log-log plot between the Findley fatigue index and fatigue life. Using fatigue test results of: 1) uni-axial tests (Scutti et al. [60], Iwafuchi et al [61], and Ahlstrom and Karlsson [62]), 2) bending tests (Fry [63]), and 3) axial-torsion tests (Stadlbauer and Werner. [64]), Fig. 3.14 presents the result of a regression analysis for κ = 0.3, where the calculated least square error is minimized. Result agrees with those reported by Park and Nelson [65] for various types

of steel—varying from 0.18 to 0.33, and by Fry [3] for a thermite welded rail steel as 0.3. The fatigue-life equation of the rail steel for Fig. 3.14 can be written as:

$$N = [10 - 3.047 \times F_{FIN}]^{(-1/0.1319)} \tag{14}$$

$$\text{Damage per loading cycle} = 1/N$$

where N is the number of cycles to fatigue failure

F_{FIN} is the Findley fatigue index

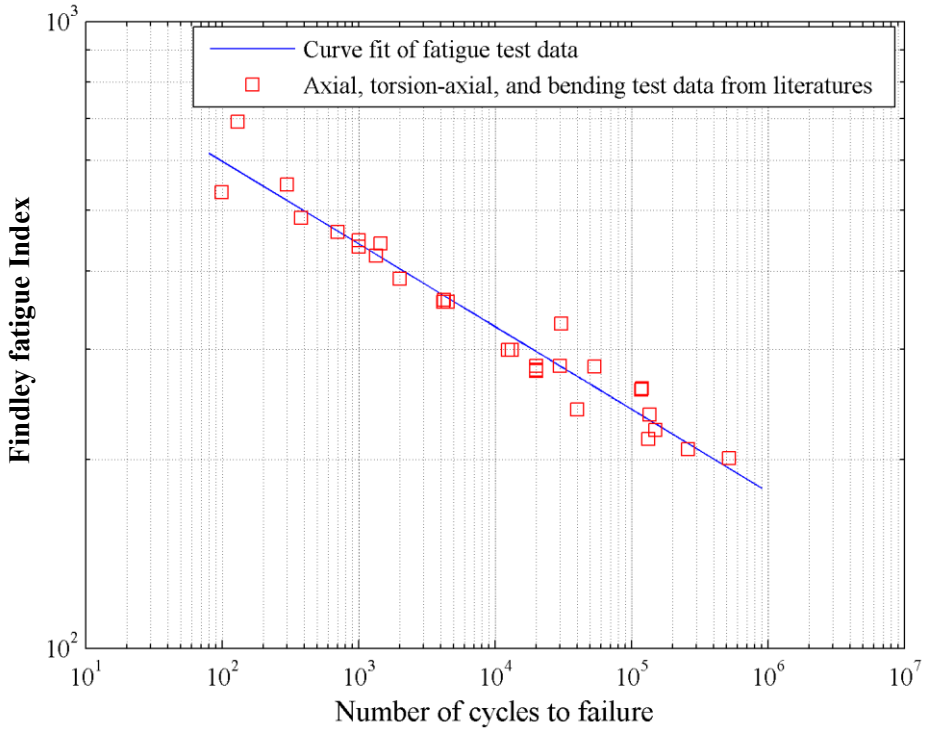

Fig. 3.14. A log-log plot between Findley fatigue index and number of cycles to failure for κ = 0.3. Fatigue test data are taken from various literatures.

As a result, in this study, assuming no surface wear and artificial grinding, fatigue cracks tend to occur at near surface first as shown in Fig. 3.3 and 3.8. However,

there is still a finite accumulation of fatigue damage at subsurface, which is likely to be increasingly dominant with a presence of material imperfections or discontinuities that may act as a stress-riser.

3.4.7 Fatigue Index at Three Orthogonal Planes

Using the rolling stress result at the sixth loading cycle of the 162 kN wheel load for a fatigue analysis with $\kappa = 0.3$, Fig. 3.15 shows contours of Findley fatigue index at three different planes—the horizontal, vertical, and transverse planes—that are often used to classify types of defects in railroad rails (Sperry Rail Service [2]). Note that the contours are presented in different scales. The direction of cosines of the horizontal, vertical, and transverse planes are (0, 1, 0), (0, 0, 1), and (1, 0, 0) respectively. Among these three planes, the fatigue index at near surface observed in the horizontal plane is the largest (Fig. 3.15(a)), approximately twice as much as the peak fatigue indexes found in the vertical and transverse planes. Hence, surface shelling is likely to be a failure mode under this circumstance.

For a perfect rail head, the fatigue index contour in the vertical plane (Fig. 3.15(b)), similar to the vertical split head, is localized at subsurface; whereas, fatigue indexes at surface and subsurface are competitive in the transverse plane (Fig. 3.15(c)). Cannon et al. [8] report that material imperfections or discontinuities due to manufacturing process, if presence at some depths below running surface, may serve as a subsurface fatigue crack nucleation site. The increase of fatigue index and change of

the plane of crack nucleation depend on the shape and orientation of the imperfections as pointed out by Fry [3], and they are not investigated in this study.

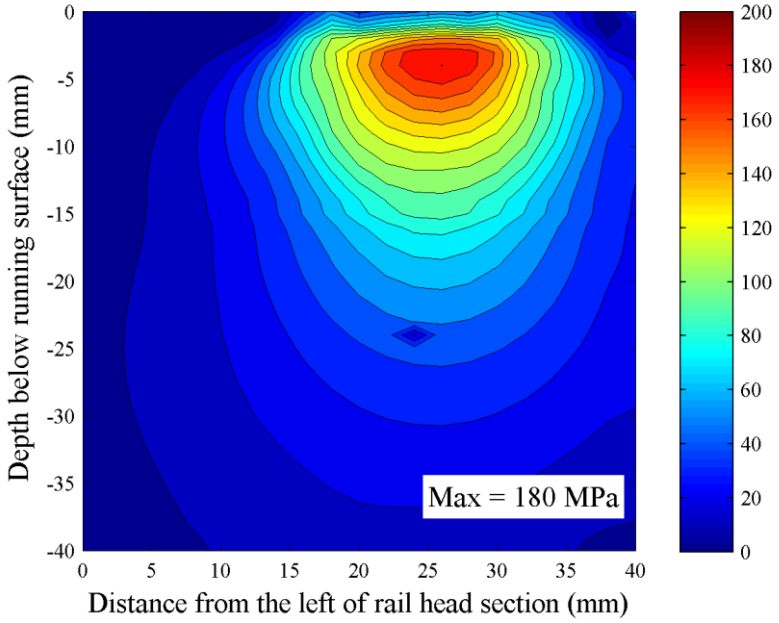

(a)

Fig. 3.15. Findley fatigue index contours (κ = 0.3) of the 162 kN wheel load at the sixth loading cycle, in different scales, at (a) horizontal, (b) vertical, and (c) transverse, planes.

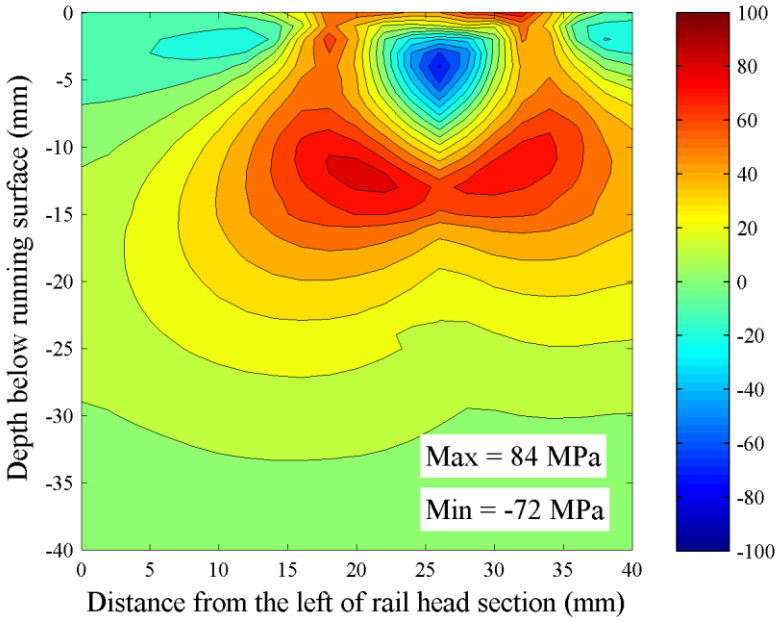

(b)

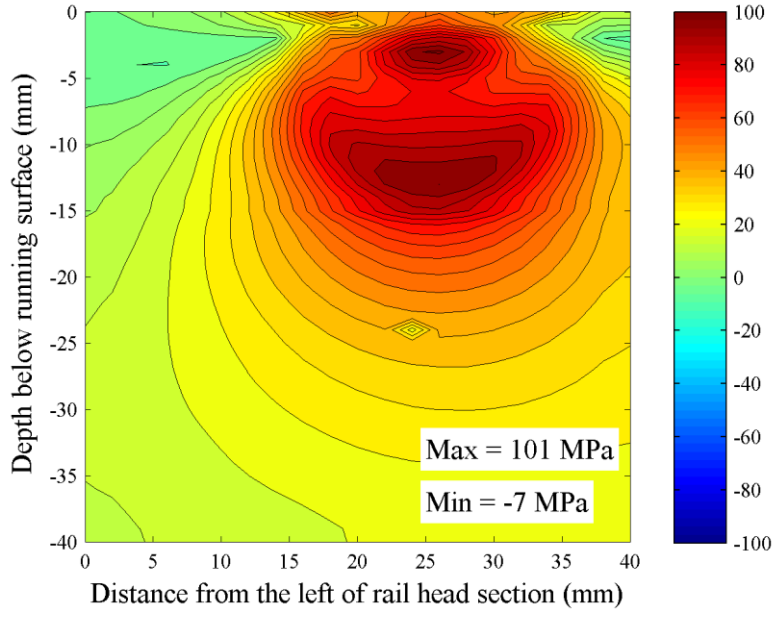

(c)

Fig. 3.15. Continued.

3.4.8 Limitation of Findley Fatigue Criterion to Wheel-Rail Rolling Contact

Since the Findley fatigue criterion is the stress-based approach, it is generally applicable to high-cycle fatigue problems, where stress is lower than material yielding limit. But the results from Chapter II show that material close to wheel-rail interface, from 0 - 10 mm below running surface, deforms plastically. This means that the relationship between stress and strain is no longer linear, and damage mechanism is preferably defined in term of strain (low-cycle fatigue) instead. Therefore, the Findley fatigue criterion is not applicable to the near surface region. In order to resolve this issue, an analysis with a strain-based critical plane criterion will be investigated in the next chapter. Note that this is not the case for fatigue analyses at depth greater than 8 mm below running surface, because both stress-based and strain-based approaches are theoretically the same for high-cycle fatigue application.

3.5 Conclusions

- For both the 162 kN and 223 kN wheel loads, larger fatigue index at subsurface is observed when accounting for the residual stresses. In some cases, this may serve as another possible crack nucleation site.
- As the participation of the normal stress term in the Findley fatigue criterion is low, the shear stress amplitude term dominates the near-surface crack nucleation, representing a failure mechanism of materials with high ductility.
- As the participation of the normal stress term in the Findley fatigue criterion is high, both the normal stress and shear stress amplitude promote the

subsurface crack nucleation, representing a failure mechanism of brittle material.

- At near surface, the plane of fatigue crack nucleation is similar to surface shelling, while the one at subsurface is a mixed mode between the vertical and horizontal planes similar to longitudinal cracks.
- The normal coefficient of typical pearlitic rail steel, defined by κ , is equal to 0.3. The fatigue index at subsurface is smaller but finite compared to that found at near surface for this case.
- The Findley fatigue criterion, which is a stress-based approach, may not accurately present the phenomena at near surface region, where plastic deformation is observed. The strain-based approach is preferable for this case.

CHAPTER IV

A STUDY OF RAIL HEAD FATIGUE DAMAGE WITH A STRAIN-BASED CRITICAL PLANE CRITERION

4.1 Introduction

Based on observations by Smith [6], Cannon et al. [8], Tunna et al. [10], and Ekberg and Kabo [11], fatigue cracks in rail heads nucleate either at near running surface or at some depth below running surface. Since materials in those two regimes behave differently, using only components of stress tensors to describe failure mechanisms for the whole rail head may be inadequate. At near running surface, layers of material near running surface experience severe plastic deformation as a result of a concentrated wheel load, which can be seen as a forward surface flow in experiments (Shima et al. [46] and Hamilton [47]). A relationship between stress and strain is no longer linear in this region because of the strain-hardening mechanism, which, for general metallic materials, will incrementally decrease the stiffness of material as it is loaded further. As a result, a small change of stress may lead to relatively much greater change of strain, suggesting using strains to describe damage evolution with plasticity effect instead.

At greater depth from the running surface, effects from a localized wheel-rail contact diminish. Materials behave elastically, and failure mechanism is defined as a high-cycle fatigue (HCF) mode. Fatigue damages calculated using the stress-based approach—i.e. Findley fatigue criterion (Findley [55]), and the strain-based approach—

i.e. Fatemi-Socie fatigue criterion (Fatemi and Socie [66])—are equally valid for the HCF regime because a relationship between corresponding stress and strain is linear. A study with the Findley fatigue criterion, for a rail head with no material imperfections or discontinuities, in Chapter III shows that the effective normal stresses—a combination of rolling stresses and residual stresses—highly influence the nucleation of subsurface fatigue cracks. Whereas, the surface fatigue cracks are the only possible mode of failure when the residual stresses are excluded. This emphasizes the importance of an inclusion of the residual stresses, especially the tensile residual stresses found at subsurface, into fatigue damage analyses of a wheel-rail rolling contact. Any fatigue criterion proposed for a rolling contact problem should be able to account for the effective rolling stress and mean stress effect into its formulation.

As previously shown in Fig. 2.19 in Chapter II for the 162 kN wheel load, plastic strain accumulations in vertical and transverse directions at near surface, around 0 - 10 mm, at sixth loading cycles are predicted, but do not show significant increase of the accumulation after 4 cycles of loading. Therefore, ratcheting failure, which is defined by a continuous accumulation of strains that will eventually exhaust material's ductility, can not be used to predict fatigue crack nucleation at near-surface in this study. Low-cycle fatigue (LCF) failure, which should be defined in term of strains, is considered as the only failure mechanism for the surface fatigue cracks instead.

To overcome the limitation of the stress-based critical plane criterion on the prediction of near-surface fatigue crack nucleation, a fatigue model must be able to accommodate the followings key points: 1) the influence of effective rolling stresses on

the nucleation of subsurface fatigue crack, and 2) the influence of strain accumulation on fatigue damage in a rail head, with an emphasis on LCF failure at near running surface. The Fatemi-Socie fatigue criterion, formulated such that the shear-strain amplitude is modified by a normal stress component, is investigated for its capability to predict surface and subsurface fatigue crack nucleation due to rolling contact in this chapter.

4.2 Strain-Based Critical Plane Criteria

As well as the strain-life method for LCF with plasticity in uni-axial problems, a strain-based critical plane criterion is recommended when von-Mises equivalent stresses in a region of interest exceed an elastic limit for multi-axial problems. Reviews of theories and applications on various strain-based approaches are given by Meggiolaro et al. [51] and Stephens et al. [67]. Analogous to the Findley fatigue criterion, which is defined as a combination of shear stress amplitude and factorized normal stress on a plane, Brown and Miller [68] formulate a strain-based criterion for shear failure mode as a combination of shear strain amplitude and factorized normal strain on a plane. They propose that cracks nucleate on the plane of maximum shear strain amplitude, not on the plane of the maximum of the combination. The Brown-Miller fatigue model is a pure strain-based approach with no coupling from any stress component; therefore, it is unable to incorporate residual stresses into fatigue damage predictions.

To account for an additional material hardening due to the changing of principal directions from non-proportional loading, Fatemi and Socie [66] suggest replacing the normal strain component in the Brown-Miller fatigue criterion by a normal stress

component. They also modify the fatigue criterion such that no contribution from a pure axial static load to fatigue damages is accounted; therefore, the alternating shear strain is required for fatigue damage to occur. This formulation agrees with observations from experiments and also implicitly account for the effects from residual stresses, which is one of the required key characteristics in this study. The Fatemi-Socie fatigue criterion, providing results in term of *fatigue index*, is shown to be satisfactory in term of fatigue life predictions for various types of metallic material (Socie [14], Fatemi and Socie [66], Jiang et al. [54], Park and Nelson [65], and Fatemi and Kurath [69]. However, the validation of predicted critical plane against experiments is still limited. Using a structural steel (S460N), Jiang et al. [54] study the capability of Fatemi-Socie fatigue criterion and other fatigue models on critical plane predictions. They show that critical plane predictions from all methods deviate from experimental results with varying degrees. They also suggest that an application of critical plane criteria to a material different from the one used in the formulation of criterion must be done with caution.

The coefficient term used to factorize the influence of normal stress on the Fatemi-Socie fatigue criterion is called *normal coefficient* (η) in this study. It is material-dependent and must be determined by a regression analysis of a set of fatigue-life data from uni-axial and torsional fatigue tests, or from at least two tests with different type of loading. The normal coefficient exhibits material sensitivity to the tensile-based damage mechanisms. For example, pure shear damage will correspond to η equal to 0, meaning no influence of the normal stress on fatigue damage mechanism. However, due to the formulation of the criterion, the Fatemi-Socie fatigue criterion is

not applicable to pure tensile-based damage. This will be discussed in greater details in the next section.

The same assumption used previously with the Findley fatigue criterion that crack nucleation and early crack growth periods are considered to consume most of the service life of rails is still applied to this chapter. Life in crack propagation stage, which could be analyzed by fracture mechanics, is assumed to be minimal. An observation by Socie [14] that there is no interaction between different damage planes is still hold, and fatigue indexes should be tracked for each plane independently.

4.3 Fatigue Index Calculation

Originally proposed by Fatemi and Socie [66], the Fatemi-Socie fatigue criterion is represented by the following equation.

$$f_{FAT} = \frac{\Delta\gamma_{\max}}{2}\left(1 + \eta\frac{\sigma_n}{\sigma_y}\right) \tag{15}$$

where $\Delta\gamma_{\max}$ is the maximum shear strain range during rolling step among all possible planes

σ_n is the maximum normal stress during rolling step on a plane of the maximum shear strain range

σ_y is the tensile yield strength of material (406 MPa)

η is the normal coefficient, which is an empirical material constant

f_{FAT} is the Fatemi-Socie fatigue index

The normal stress component is defined as a ratio between the maximum normal stress and monotonic tensile yield stress so that the Fatemi-Socie fatigue criterion remains dimensionless, as is a strain. The critical plane of the above equation is defined as the plane of the maximum shear strain amplitude ($\Delta\gamma_{\max}/2$), not the plane of the maximum of total fatigue index. As a result, in general, the plane where the shear strain amplitude is largest does not necessarily coincide with the plane where the fatigue index is largest, leading to possible ambiguities when performing an optimization of grinding schedules. For example, the plane where the fatigue index accumulation is largest may not coincide with the critical plane predicted by the Fatemi-Socie fatigue criterion. In order to avoid such a problem, the modified Fatemi-Socie fatigue criterion is proposed as the following equation.

$$f_{FAT-MOD} = \left[\frac{\Delta\gamma}{2}\left(1+\eta\frac{\sigma_n}{\sigma_y}\right) \right]_{\max} \tag{16}$$

where $f_{FAT-MOD}$ is the *modified Fatemi-Socie fatigue index*

The critical plane of the modified Fatemi-Socie fatigue criterion is, instead, defined as the plane of the maximum total fatigue index. It is reinforced by Jiang et al. [54] that the discrepancy between the critical planes predicted by the original and the modified Fatemi-Socie fatigue criterion is small. In this study, the modified Fatemi-Socie fatigue criterion is used as it is practically preferable.

Method of fatigue analyses with a critical plane fatigue criterion is described earlier in detail in Chapter III for the stress-based approach. The algorithms of transformation and decomposition of a tensor are also applicable to the strain-based

approach, and only a brief summary will be given in this chapter. To find a plane where the modified Fatemi-Socie fatigue index is largest, an exhaustive search throughout all possible planes is performed with a 10 degree increment in a spherical coordinate. Using a stress-strain tensor history during the sixth rolling cycles of the 162 kN or 233 kN wheel loads as an input, the stress-strain tensors of each node of interest are tracked and transformed into shear and normal components. For each plane, shear strain amplitude is determined from variations of the resolved shear strain vectors at different time increments, and it will be modified by the corresponding normal stress according to the equation (16) for resultant fatigue index.

Parametric studies of the influence of wheel loads (162 and 233 kN) and normal coefficient (η = 0.5 – 3.0) on fatigue index, and location and critical plane of crack nucleation will be reported for the representative cross-section of interest, located at the middle—35 mm from the starting point—of the 70 mm-long rolling path, as defined in Fig. 2.8(b). This cross-section is where combined effects from global bending and rolling are expected to be largest. The definitions of three principal axes: vertical, longitudinal, and transverse, and three orthogonal planes: horizontal, vertical and transverse, are as same as the ones defined previously in Fig. 2.9(b).

4.4 Results and Discussion

4.4.1 Fatigue Index of the 162 kN Wheel Load with Material Hardening

For each node on the cross-section of interest, the modified Fatemi-Socie fatigue index is calculated from a stress and strain tensor history at the sixth loading cycles for

all selected planes. Among those planes, contours of the largest fatigue indexes are reported in Fig. 4.1 to 4.4, for different normal coefficients (η) for the 162 kN wheel load. Note that it is not necessary that critical planes have to be the same for different nodes. The maximum and minimum fatigue indexes are reported within figures, when applicable. Fatigue cracks are categorized into two types, depending on where they are observed. Fatigue crack nucleation located within 0 - 5 mm below running surface is defined as a surface-type, while one located at the depth greater than 5 mm is defined as a subsurface-type.

A site of crack nucleation is where the modified Fatemi-Socie fatigue damage is largest. For $\eta = 0$ (Fig. 4.1), meaning cracks are nucleated solely by shear strain amplitude component, the contour of fatigue index is localized within 0-10 mm below the running surface, right under the wheel-rail contact point, with the largest fatigue index of 0.001341 at approximately 3 mm below running surface. This suggests a possibility of surface crack nucleation. As the participation of normal stress, η, on damage mechanism increases from 0 to 1, fatigue index is still mainly localized at 3 mm below running surface, but with a lower peak value of 0.001225, as shown in Fig. 4.2. At the same time, the contour of fatigue index is observed to grow deeper into subsurface region. Fig. 4.3, and 4.4 show the fatigue index contours when $\eta = 3$ and 5 respectively. In both cases, two sites of surface fatigue cracks are predicted at about 2 - 3 mm below running surface, one to the left and another to the right of wheel-rail contact as looking into the transverse plane. Another possible crack nucleation site is predicted at 11 - 13 mm below the running surface, where tensile residual stresses from rolling contact

presented in Chapter II are largest. This implies an important role of normal stress—strongly influenced by residual stresses—on subsurface fatigue crack nucleation.

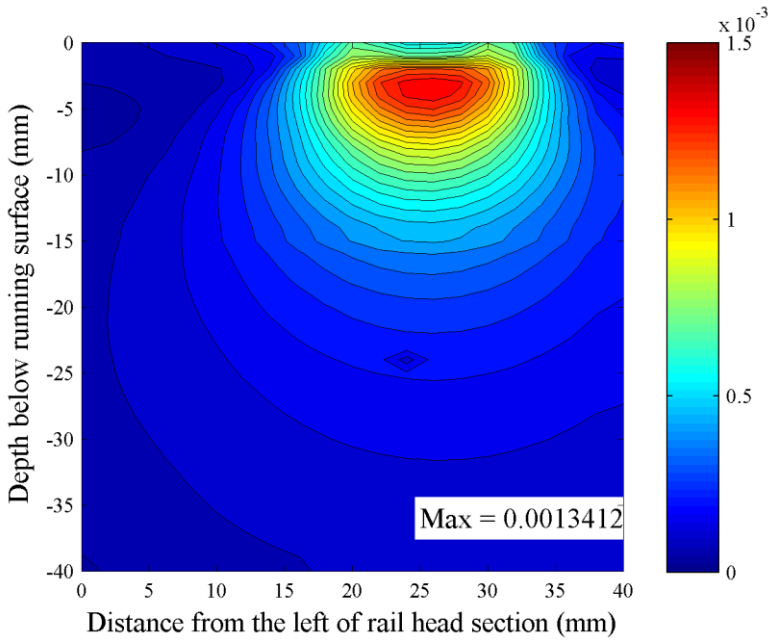

Fig. 4.1. Maximum modified Fatemi-Socie fatigue index contour ($\eta = 0$) of the 162 kN wheel load at the sixth loading cycle by searching selected plane at all nodes.

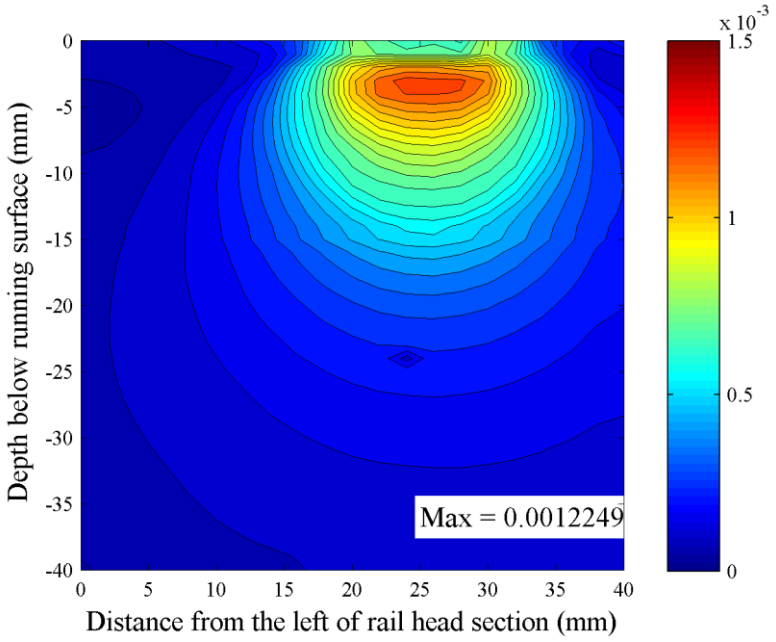

Fig. 4.2. Maximum modified Fatemi-Socie fatigue index contour (η = 1) of the 162 kN wheel load at the sixth loading cycle by searching selected plane at all nodes.

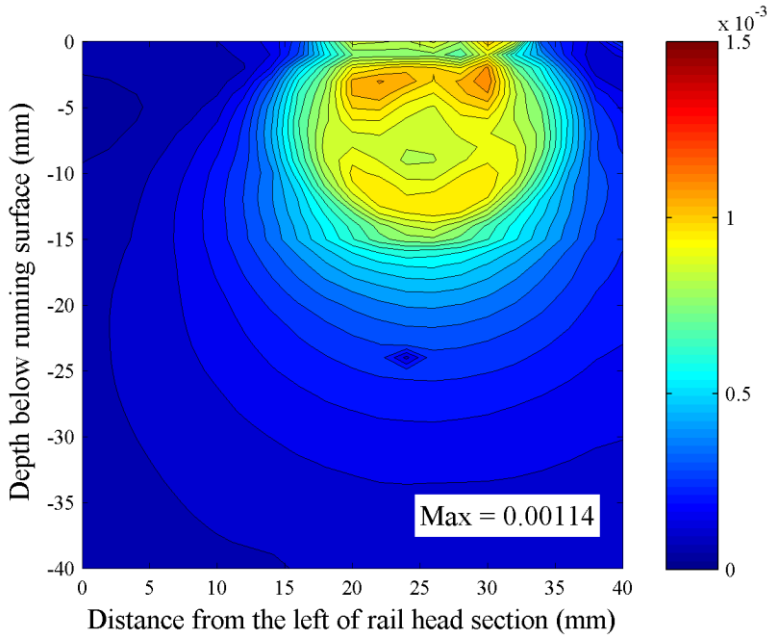

Fig. 4.3. Maximum modified Fatemi-Socie fatigue index contour (η = 3) of the 162 kN wheel load at the sixth loading cycle by searching selected plane at all nodes.

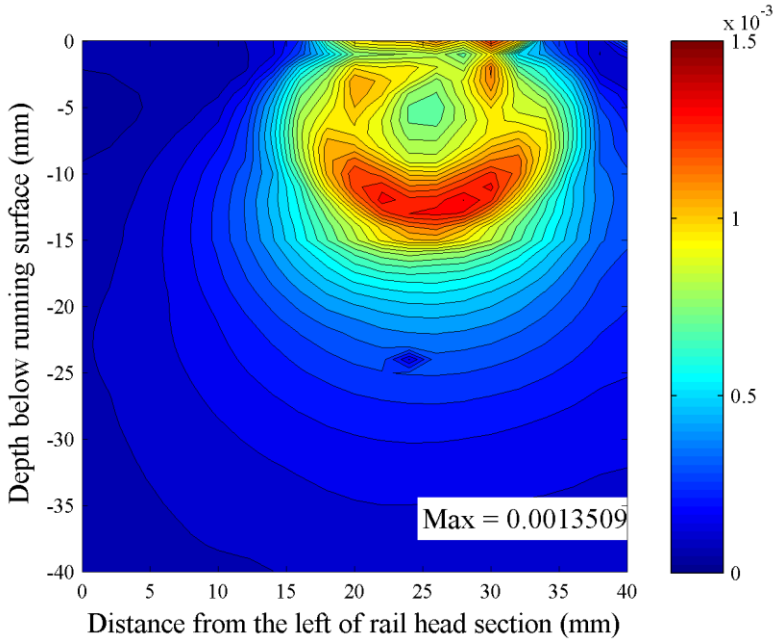

Fig. 4.4. Maximum modified Fatemi-Socie fatigue index contour (η = 5) of the 162 kN wheel load at the sixth loading cycle by searching selected plane at all nodes.

Accounting for residual stresses, the more the participation of normal stress is, the more damaging the rail head at greater depth below running surface is predicted. For example, the peak fatigue index of node#234976 at subsurface increases from 0.000989 to 0.001314 as η increases from 3 to 5. The fatigue index at near surface, in contrast, reduces gradually as η increases from 0 to 3 as a result of compressive residual stresses, but the trend reverses as η increases from 3 to 5. This inconsistency may arise from an assumption behind the formulation of the modified Fatemi-Socie fatigue criterion that shear strains control damage mechanism, whereas the normal stress component only operates as a modifier. Therefore, using η much greater than 1, which indicates likely tensile-based damage, may violate the assumption and misrepresent the damage

phenomena, both at near surface and subsurface. This suggests that applications of the modified Fatemi-Socie fatigue criterion on brittle materials may be limited, and a tensile-based critical plane fatigue criterion proposed by Smith et al. [70] may be preferable for this case.

The direction cosines of critical planes, the approximated cracking planes, and the corresponding fatigue indexes of possible crack nucleation sites for all cases are summarized in Table 4.1. Defined in previous chapters, x-axis coincides with the longitudinal direction of a rail, while y-axis and z-axis coincide with the vertical and transverse directions respectively. The critical planes of surface cracks for all cases of η approximately coincide with the horizontal plane, where surface shelling is usually developed in field observations. Note that two near-surface fatigue crack nucleation sites are predicted for η = 3 and 5, while only one site is predicted for η = 0 and 1. For subsurface cracks, which are evident only in the case of η = 3 and 5, the three largest fatigue indexes are reported to represent a relatively large damage distribution at subsurface. All critical plane predictions at subsurface are qualitatively similar; it is a mixed cracking mode between the vertical and horizontal planes, similar to what defined as longitudinal cracks in field observations. Further study on fatigue damage and critical planes in heavier wheel loads will be discussed in the next section.

Table 4.1

Summary of possible fatigue crack nucleation sites and cracking planes for the 162 kN wheel load with material hardening (modified Fatemi-Socie fatigue criterion).

Normal coefficient	Node #	Fatigue index	Depth below running surface (mm)	Unit normal vector of critical plane			Cracking plane
				x	y	z	
0	235063	0.001341	3	0.3420	0.9397	0.0000	Horizontal
1	235043	0.001225	3	0.1710	0.9698	0.1736	Horizontal
3	234967	0.001114	2	0.1710	0.9698	-0.1736	Horizontal
	234968	0.001140	3	0.1736	0.9848	0.0000	Horizontal
	234976	0.000989	11	0.0000	0.7660	0.6428	H-V**
	235074	0.000988	12	0.1330	0.7544	-0.6428	H-V**
	235083	0.000975	13	0.1116	0.6330	0.7660	V-H*
5	234967	0.001166	2	0.1710	0.9698	-0.1736	Horizontal
	234968	0.001145	3	0.1736	0.9848	0.0000	Horizontal
	234976	0.001314	11	0.0000	0.7660	0.6428	H-V**
	235080	0.001351	12	0.0000	0.6428	0.7660	V-H*
	235083	0.001317	13	0.1116	0.6330	0.7660	V-H*

*V-H: A mixed cracking plane between the vertical and horizontal planes, where the leading term—V— indicates the cracking plane is more inclined toward the vertical plane.
**H-V: A mixed cracking plane between the vertical and horizontal planes, where the leading term—H— indicates the cracking plane is more inclined toward the horizontal plane.

4.4.2 Fatigue Index of the 162 kN Wheel Load with an Elastic Material

Using the elastic rolling stress/strain result from Chapter II as an input for fatigue analyses, in contrast to the case with material hardening, most part of fatigue index contours remain unchanged as η increase from 0 to 3 as shown in Fig. 4.5 and 4.6. The contour of fatigue index is localized within 0 - 10 mm below running surface with the largest fatigue index of 0.001598 and 0.001609 at 3 mm below running surface for the case of η = 0 and 1 respectively. Subsurface crack nucleation is not predicted in both cases. In term of subsurface fatigue crack nucleation, this indicates a strong detrimental influence of residual stresses, which are largely tensile at 10 - 30 mm below running surface, on the distribution of fatigue index to greater depth that could result in subsurface crack nucleation in some cases.

Comparing Fig. 4.1 to Fig. 4.5 for the case of η = 0, in contrast, the fatigue index at near surface decreases from 0.001598 to 0.001341 when residual strains accumulated near the running surface as a result of rolling contact are considered. A similar observation is observed in the simulation with η = 3 (see Fig. 4.3 and 4.6), indicating a beneficial role of the strain accumulation on surface fatigue crack nucleation calculated in term of low-cycle fatigue. This contradicts to the detrimental role of strain accumulation in failures due to ratcheting.

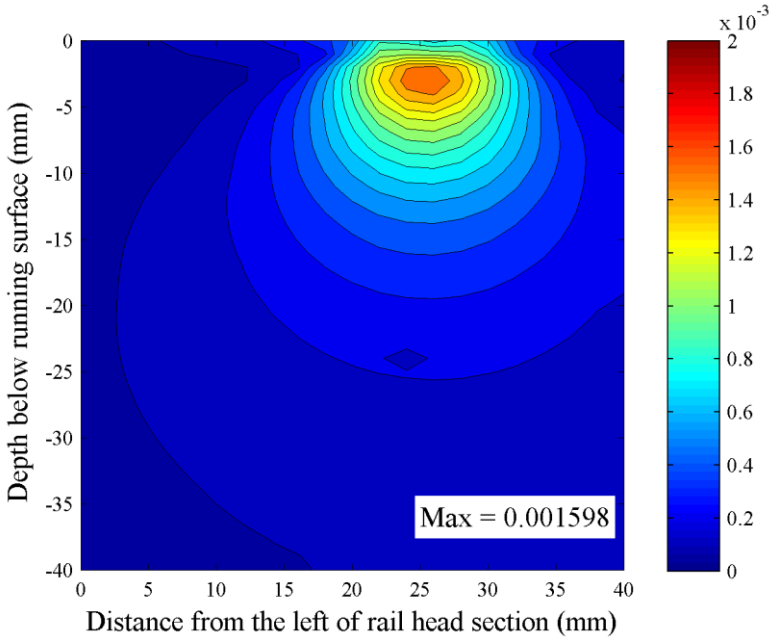

Fig. 4.5. Maximum modified Fatemi-Socie fatigue index contour ($\eta = 0$) of the 162 kN wheel load with elastic material by searching selected plane at all nodes.

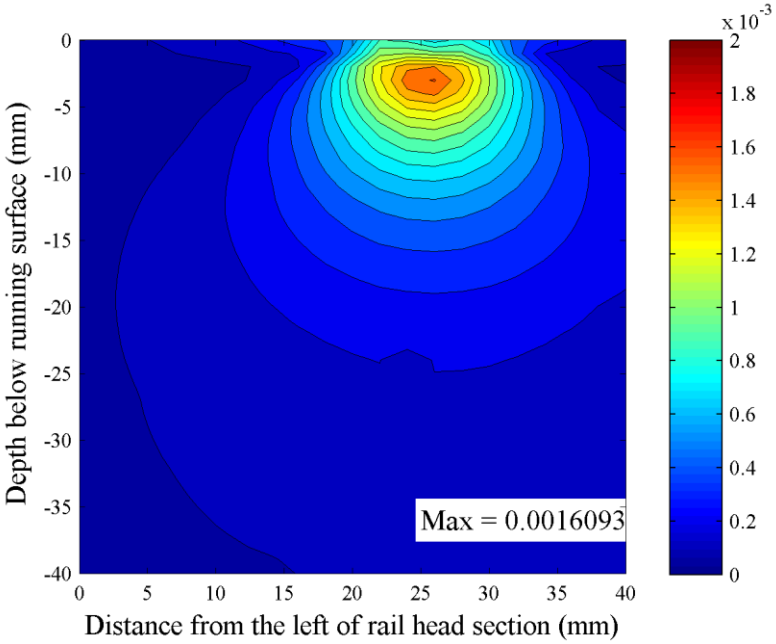

Fig. 4.6. Maximum modified Fatemi-Socie fatigue index contour ($\eta = 3$) of the 162 kN wheel load with elastic material by searching selected plane at all nodes.

4.4.3 Fatigue Index of the 233 kN Wheel Load with Material Hardening

Fig. 4.7, 4.8, 4.9 and 4.10 are the fatigue index contours occurred during the sixth cycle of a rolling contact of the 233 wheel load as η equals to 0, 1, 3, and 5 respectively. In all cases, the fatigue crack nucleation sites found near the running surface are located at approximately 3 - 4 mm below running surface, with decreasing peak values as η increases. Two sites of surface fatigue cracks, one to the left and another to the right of wheel-rail contact point as looking into the transverse plane, are predicted for η = 3 and 5, as shown in Fig. 4.9 and 4.10. Branching of the fatigue index contours to greater depth, approximately 14 - 16 mm below the running surface, is predicted in all cases with η greater than 0, and it is more evident as η increases. As a result, there occurs another possible crack nucleation site at the subsurface, where the peak fatigue index is competitive, or even greater for η = 5, to that at near running surface for η = 3.

The direction cosines of critical planes, approximated cracking planes, and corresponding fatigue indexes of possible crack nucleation sites for all cases are summarized in Table 4.2. Results are qualitatively similar to those from the 162 kN wheel load case. The critical planes of surface cracks for all values of η approximately coincide with the horizontal plane, where surface shelling is usually developed in field observations. For subsurface cracks, which are evident only in the case of η = 3 and 5, the three largest fatigue indexes is reported to represent a relatively large damage distribution at subsurface. All critical plane predictions are qualitatively similar; it is a

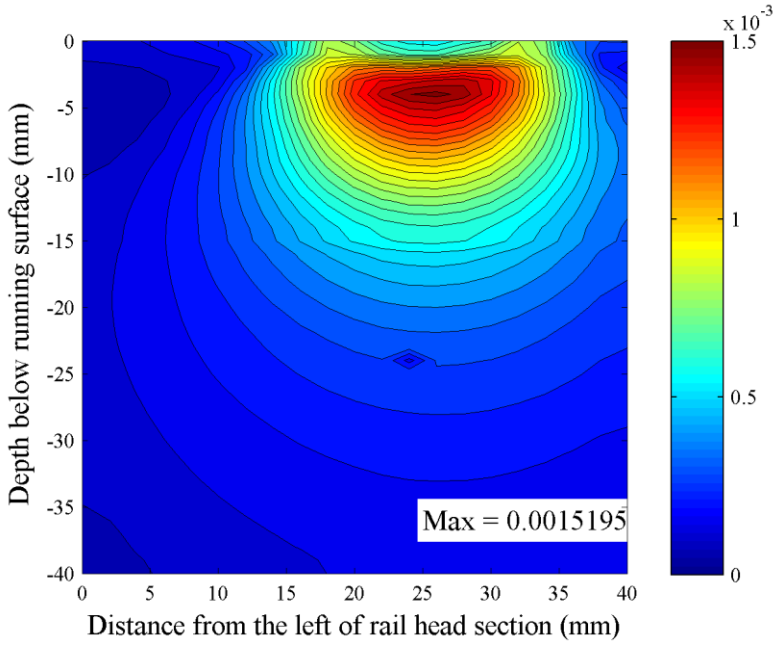

Fig. 4.7. Maximum modified Fatemi-Socie fatigue index contour (η = 0) of the 233 kN wheel load at the sixth loading cycle by searching selected plane at all nodes.

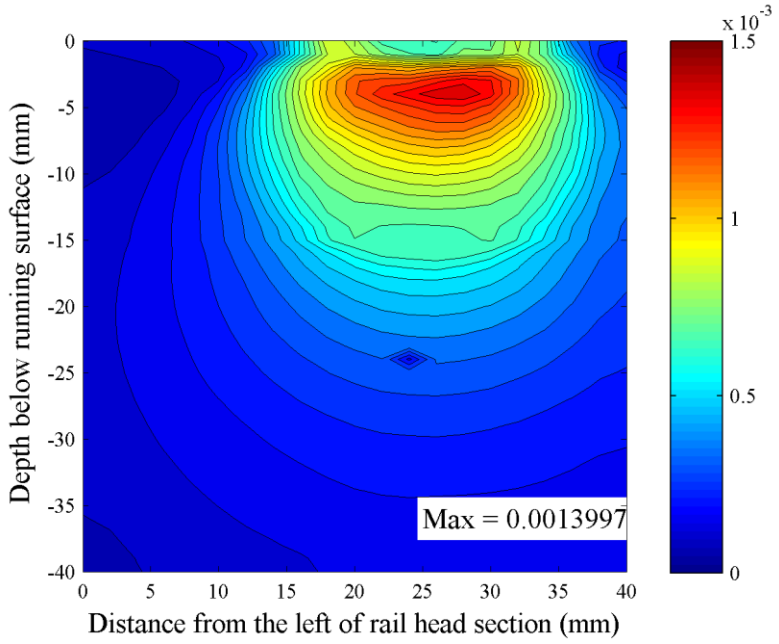

Fig. 4.8. Maximum modified Fatemi-Socie fatigue index contour (η = 1) of the 233 kN wheel load at the sixth loading cycle by searching selected plane at all nodes.

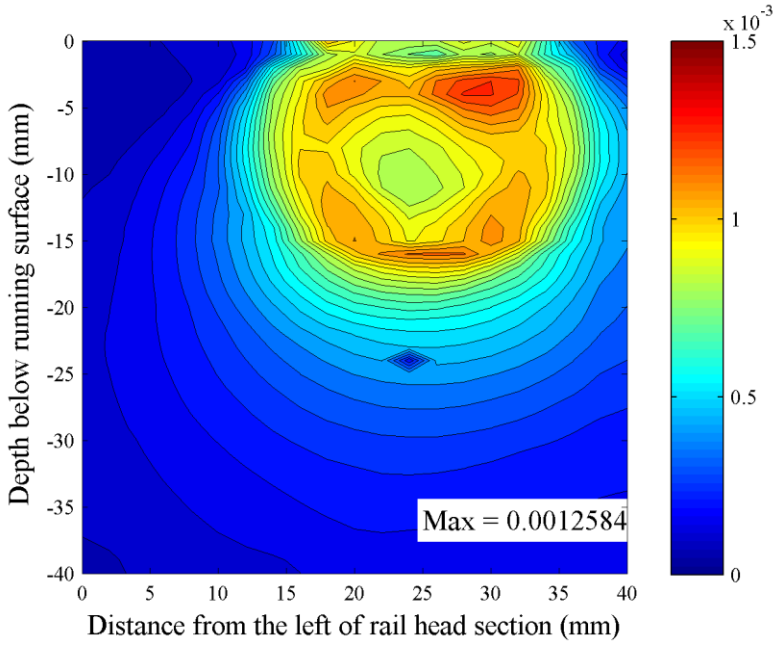

Fig. 4.9. Maximum modified Fatemi-Socie fatigue index contour (η = 3) of the 233 kN wheel load at the sixth loading cycle by searching selected plane at all nodes.

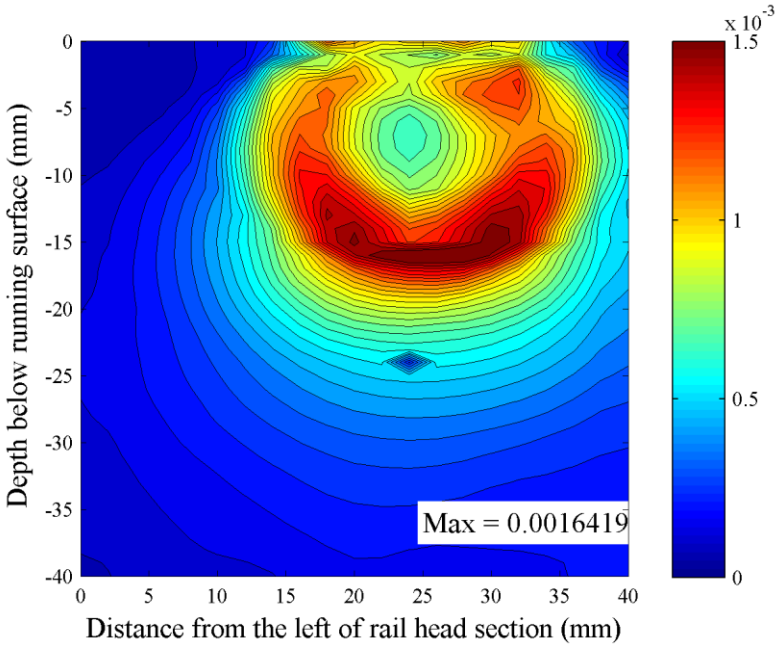

Fig. 4.10. Maximum modified Fatemi-Socie fatigue index contour (η = 5) of the 233 kN wheel load at the sixth loading cycle by searching selected plane at all nodes.

Table 4.2

Summary of possible fatigue crack nucleation sites and cracking planes for the 233 kN wheel load with material hardening (modified Fatemi-Socie fatigue criterion).

Normal coefficient	Node #	Fatigue index	Depth below running surface (mm)	Unit normal vector of critical plane			Cracking plane
				x	y	z	
0	235053	0.001520	4	-0.3420	0.9397	0.0000	Horizontal
1	235052	0.001400	4	-0.1736	0.9848	0.0000	Horizontal
3	234968	0.001250	3	-0.1736	0.9848	0.0000	Horizontal
	235052	0.001258	4	0.0000	1.0000	0.0000	Horizontal
	234979	0.001121	14	0.0000	0.7660	0.6428	H-V**
	234844	0.001127	15	0.0000	0.7660	0.6428	H-V**
	234936	0.001159	16	0.0000	0.6428	0.7660	V-H*
5	234994	0.001266	3	0.1710	0.9698	-0.1736	Horizontal
	234990	0.001249	4	0.1736	0.9848	0.0000	Horizontal
	234844	0.001548	15	0.0000	0.7660	0.6428	H-V**
	234929	0.001553	16	0.1330	0.7544	-0.6428	H-V**
	234940	0.001642	16	0.0000	0.5000	0.8660	V-H*

*V-H: A mixed cracking plane between the vertical and horizontal planes, where the leading term—V— indicates the cracking plane is more inclined toward the vertical plane.
**H-V: A mixed cracking plane between the vertical and horizontal planes, where the leading term—H— indicates the cracking plane is more inclined toward the horizontal plane.

mixed cracking mode between the vertical and horizontal planes, similar to what defined as longitudinal cracks in field observations.

4.4.4 Comparisons between Fatigue Indexes of the 162 kN and 233 kN Wheel Loads with Material Hardening

Fatigue indexes for the case of 233 kN wheel load, in overall, are greater than those in the case of 162kN wheel load. The area coverage of fatigue index contours and the peak fatigue index are greater as wheel load increases from 162 to 233 kN for both near-surface and subsurface regimes, possibly suggesting more fatigue damage in the rail head. Because the changes of fatigue index contours for different values of η are qualitatively the same, only the case of η = 3, shown in Fig. 4.3 and Fig. 4.9, are used for the following discussion, in order to cover both near-surface and subsurface phenomena. As wheel load increases from 162 to 233 kN, the fatigue crack nucleation sites found at near running surface slightly move to greater depth, approximately from 2 to 4 mm below running surface. Two sites of surface crack nucleation are observed in both cases.

Similarly, as wheel load increases from 162 to 233 kN, the regime that subsurface fatigue cracks nucleate also move to greater depth, increasing from a range between 11 - 13 mm to 14 - 16 mm. The change to greater depth coincides with the change of the location of peak tensile residual stresses from rolling contact due to an increasing wheel load, presented in Chapter II. Unlike the case of 162 kN wheel load, the peak value of fatigue index for the 233 wheel load is more comparable to that found

at near running surface. This is due to a greater increase of tensile residual stresses (at subsurface) compared to the increase of compressive residual stresses (at near surface), as wheel load increases from 162 to 233 kN.

The critical plane predictions of possible crack sites, at both near surface and subsurface, are slightly different for both wheel loads. Approximately, surface fatigue cracks will nucleate along the horizontal plane, and subsurface fatigue cracks will form along the resultant plane between the vertical and horizontal planes.

In conclusion, by using the modified Fatemi-Socie fatigue criterion, an increase of wheel load would increase fatigue damage in rail head in overall, but not uniformly. The increase of fatigue damage at subsurface is more pronounced.

4.4.5 Influence of Shear Strain Amplitude and Normal Stress Components on Modified Fatemi-Socie Fatigue Index

A study of mechanisms of surface and subsurface fatigue crack nucleation within a rail head is presented in this section. The modified Fatemi-Socie fatigue criterion is decomposed into two components—shear strain amplitude term and normal-stress-modified shear strain amplitude term—as defined below.

- Shear strain amplitude term: $\frac{\Delta\gamma}{2}$
- Normal-stress-modified shear strain amplitude term: $\frac{\Delta\gamma}{2}\left(\eta\frac{\sigma_n}{\sigma_y}\right)$

Fig. 4.11, again, presents the modified Fatemi-Socie fatigue index contour of the 162 kN wheel load (η = 3) during the sixth loading cycles, along with its corresponding

contours of shear strain amplitude and normal-stress-modified shear strain amplitude. By adding node-by-node results of Fig. 4.11(b) and 4.11(c)—the shear strain amplitude and normal-stress-modified shear strain amplitude contours, the resultant modified Fatemi-Socie fatigue index contour is presented in Fig. 4.11(a). Also, note that the Fig. 4.11(a) is reported in different scale from the one previously shown.

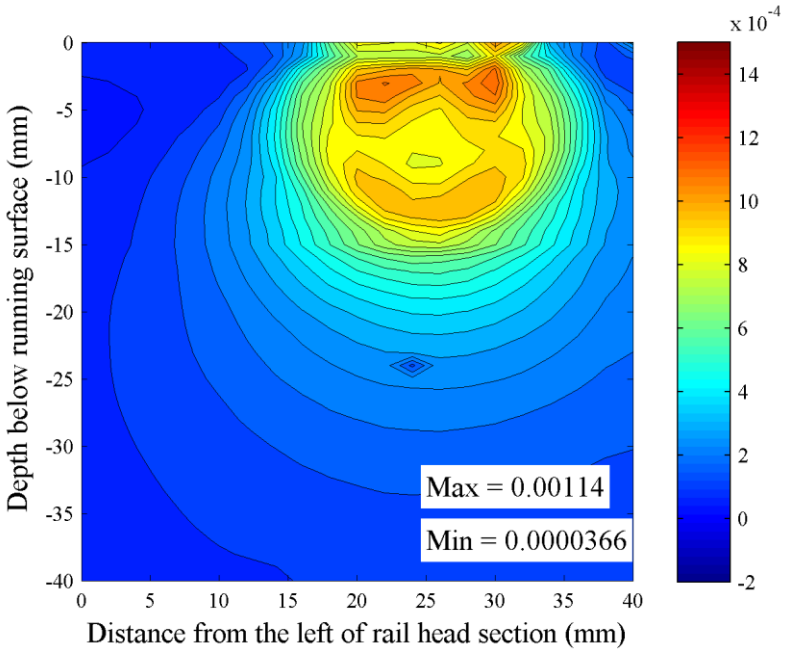

(a)

Fig. 4.11. Modified Fatemi-Socie fatigue index and its shear strain amplitude and normal stress component contours (η = 3) of the 162 kN wheel load at the sixth loading cycle by searching selected plane at all nodes.

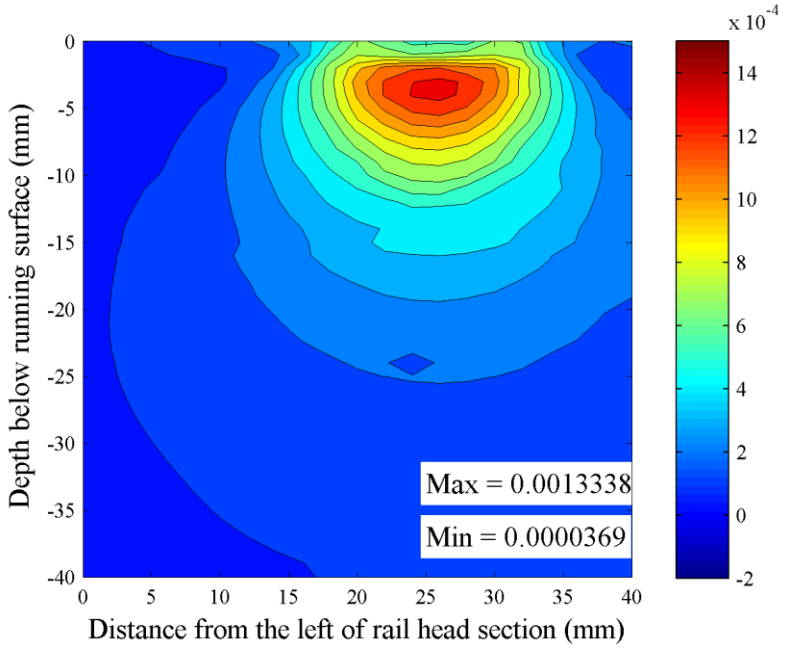

(b)

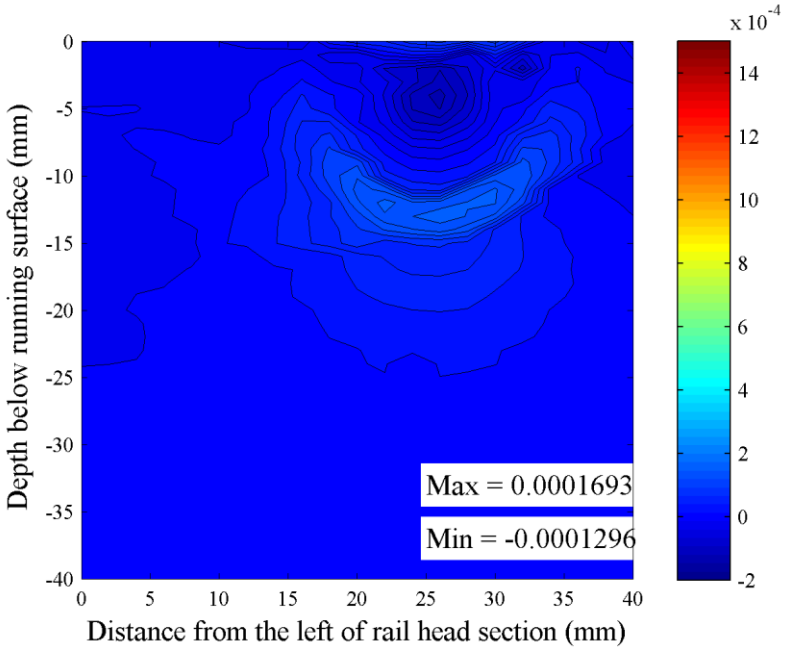

(c)

Fig. 4.11. Continued.

Comparing these three contours, the surface crack nucleation site agrees with the shear strain amplitude contour, while the subsurface crack nucleation is influenced by both the shear strain amplitude and normal stress. The conclusions of fatigue damage mechanism in a rail head according to the modified Fatemi-Socie fatigue criterion are that follow.

- Shear strain amplitude component dominates the nucleation of cracks at near surface, due to large strains and displacements at near wheel-rail interface.
- Both shear strain amplitude and normal stress promote the nucleation of cracks at subsurface—approximately at 11 - 13 mm below running surface in this case—partly due to an influence from tensile residual stresses in this region.

4.4.6 Evaluation of η for a Pearlitic Rail Steel

All discussions made prior to this section are based on general fatigue and mechanical behavior of metallic material. The predicted rolling stress results include effects from material hardening through the formation of residual stresses, but do not represent effects from implicit material behaviors, such as hardness and variation of strength across a rail cross-section. The nucleation of subsurface cracks heavily depends on the participation of normal stress term, defined by η, in the modified Fatemi-Socie fatigue criterion. The greater the η is, the greater the fatigue index at subsurface is predicted, which, cumulatively, may cause subsurface cracks in long term.

The amount of η that represents fatigue behavior of typical pearlitic rail steel can be determined from a regression analysis between the modified Fatemi-Socie fatigue index and fatigue life data of various loading configurations: uni-axial, torsion-axial, and bending, for rail steel. The proper value of η is the one that gives the best linear fitting of a log-log plot between the modified Fatemi-Socie fatigue index and fatigue life. Using the same set of fatigue test results previously used in Chapter III, Fig. 4.12 presents the result of a regression analysis for $\eta = 1$, where the calculated least square error is minimized. Result agrees with those reported by Park and Nelson [65] for various types of alloyed steel—η varying from 0 to 2. Stephens et al. [67] also recommend using $\eta = 1$ for a first approximation when fatigue test data is not available. A fatigue-life equation of rail steel for Fig. 4.12 can be written as the following equation.

$$N = \left[10^{1.0259} \times F_{FAT-MOD}\right]^{(-1/0.3485)} \tag{17}$$

$$\text{Damage per loading cycle} = 1/N$$

where N is the number of cycles to fatigue failure

$F_{FAT-MOD}$ is the modified Fatemi-Socie fatigue index

As a result, in this study, assuming no surface wear and artificial grinding, fatigue cracks tend to nucleate at near surface first as shown in Fig. 4.3 and 4.9. However, there is still a smaller but finite accumulation of fatigue damage at subsurface, which is likely to be increasingly dominant with a presence of material imperfections or discontinuities that may act as a stress-riser.

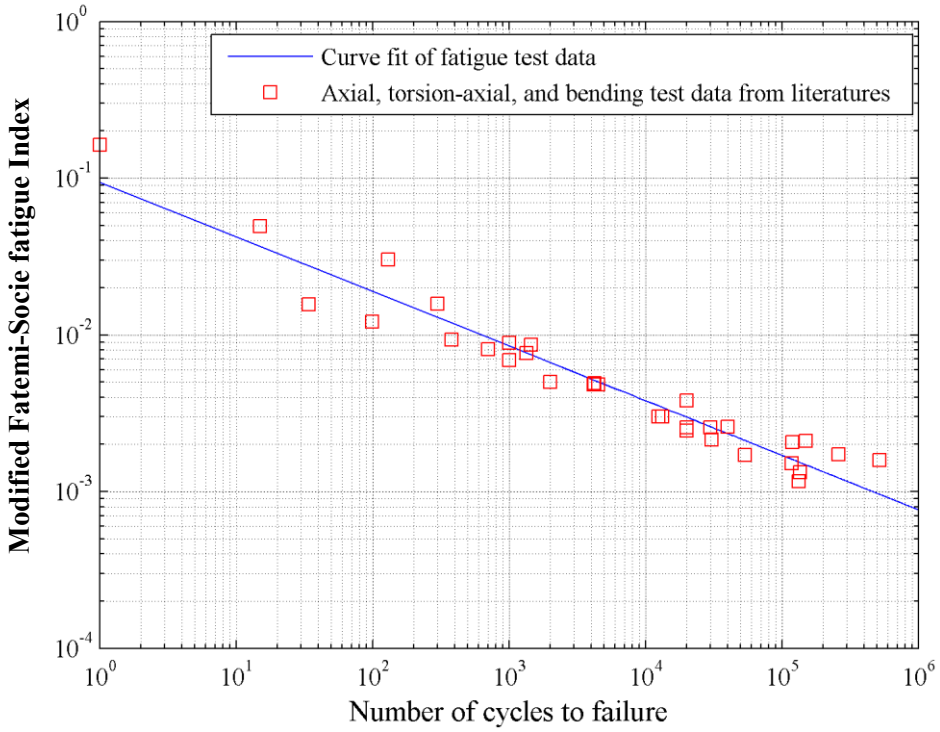

Fig. 4.12. A log-log plot between the modified Fatemi-Socie fatigue index and number of cycles to failure for $\eta = 1$. Fatigue test data are taken from various literatures.

4.4.7 Fatigue Index at Three Orthogonal Planes

Using rolling stress-strain results at the sixth loading cycle of the 162 kN wheel load for a fatigue analysis with $\eta = 1$, Fig. 4.13 shows contours of the modified Fatemi-Socie fatigue index of three different planes—the horizontal, vertical, and transverse planes—that are often used to classify types of defects in railroad rails (Sperry Rail Service [2]). Note that the contours are presented in different scales. The direction of cosines of the horizontal, vertical, and transverse planes are (0, 1, 0), (0, 0, 1), and (1, 0, 0) respectively. Among these three planes, the fatigue index at near surface predicted in

the horizontal plane is the largest (Fig. 4.13(a)), approximately twice as large as the peak fatigue indexes found in the vertical and transverse planes. Hence, surface shelling is likely to be a failure mode under this circumstance.

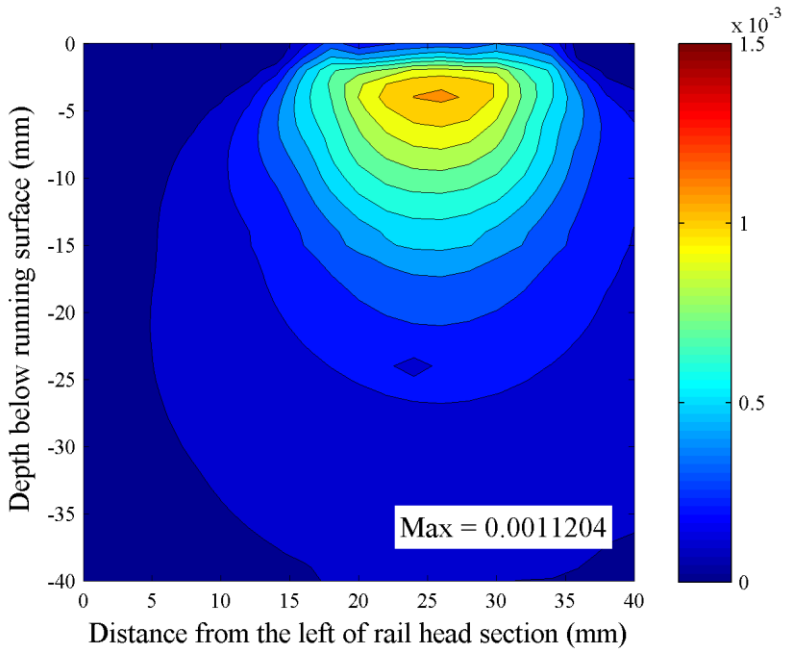

(a)

Fig. 4.13. Modified Fatemi-Socie fatigue index contour (η = 1) of the 162 kN wheel load at the sixth loading cycle, in different scales, at (a) horizontal plane, (b) vertical plane, and (c) transverse plane.

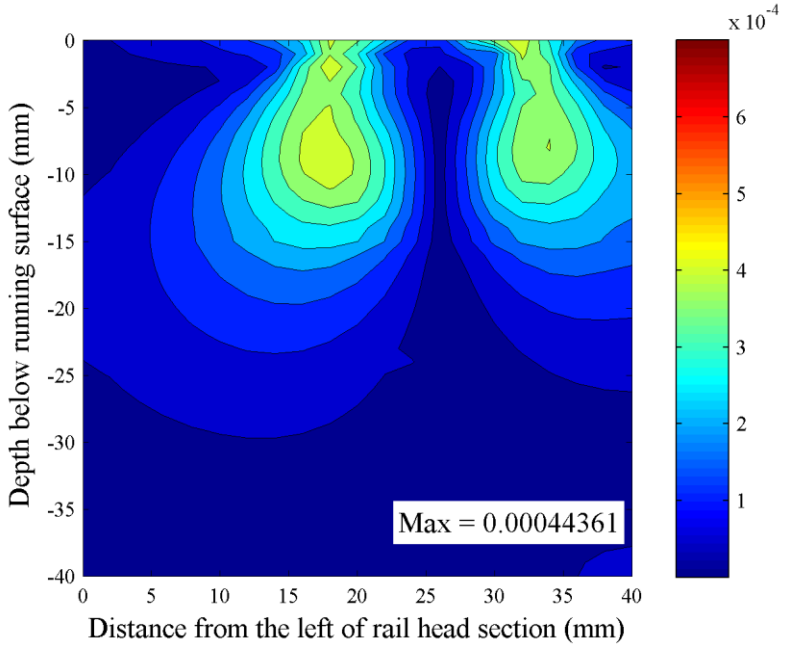

(b)

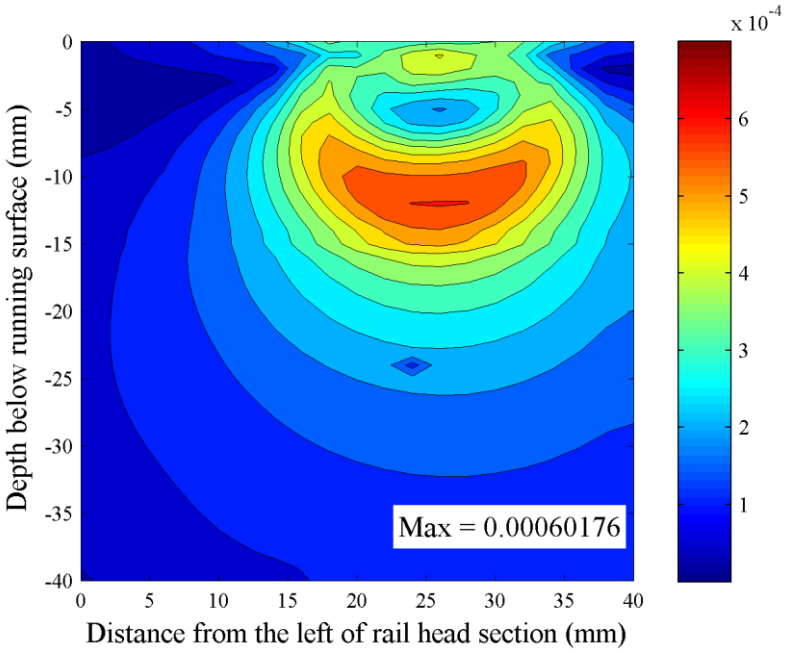

(c)

Fig. 4.13. Continued.

For a perfect rail head, a significant amount of fatigue index in the vertical plane (Fig. 4.13 (b)), similar to the vertical split head, is predicted along regions to the left and the right of the wheel-rail contact point, from running surface down to subsurface region, with greater localization at subsurface. Whereas, subsurface fatigue crack nucleation are dominant for the transverse plane (Fig. 4.13 (c)). Fatigue damages on the vertical and transverse planes may become dominant by a presence of material imperfections or discontinuities due to manufacturing process. The increase of fatigue index and change of the corresponding critical plane as a result of stress riser from discontinuities at subsurface can be determined by the Eshelby equivalent inclusion method (Eshelby [71]). Examples of the modified Fatemi-Socie fatigue index contours when there are spherical pores at subsurface are given in Appendix A.

4.4.8 Comparisons between the Stress-Based and Strain-Based Critical Plane Approaches

The Findley fatigue criterion, a stress-based critical plane approach, is defined as a linear combination of the shear stress amplitude and the factorized normal stress. As discussed in Chapter III, the criterion works well for predicting subsurface crack nucleation dominated by high-cycle fatigue, while it is not applicable to surface crack nucleation dominated by low-cycle fatigue. For the modified Fatemi-Socie fatigue criterion, which is a strain-based critical plane approach, on the other hand, an influence of the normal stress on fatigue damage is nonlinear. A ratio of normal stress and yield strength is factorized and added by 1, for a single normal-stress induced term that will be

used to multiply with the shear strain amplitude. The criterion is applicable to both high-cycle and low-cycle fatigue applications.

For both the 162 kN and 233 kN wheel loads with material hardening, in overall, the contours of Findley fatigue index and modified Fatemi-Socie fatigue index are qualitatively similar. Both criteria agree well in the critical plane predictions of both near-surface and subsurface fatigue cracks. Area coverage of the fatigue contours and the peak fatigue index increase as wheel load increases from 162 to 233 kN. The predicted fatigue indexes are localized at near surface when the participation of normal stress is small—κ = 0 and 0.3 for the Findley fatigue criterion, and η = 0 and 1 for the modified Fatemi-Socie fatigue criterion, with a finite amount of fatigue index at subsurface. As the participation of normal stress increases—κ = 0.5 and 0.7 for the Findley fatigue criterion, and η = 3 and 5 for the modified Fatemi-Socie fatigue criterion, both criteria predict another site of fatigue crack nucleation at subsurface, located at the same depth where the largest tensile residual stress resides. However, predictions of the near-surface fatigue cracks are different. The modified Fatemi-Socie fatigue criterion predicts two near-surface crack nucleation sites, while the Findley fatigue criterion predicts only one.

Because fatigue indexes calculated from both approaches are represented in different units, a quantitative comparison of fatigue indexes must be done in term of fatigue index per loading cycle, which relates to the fatigue-life equations: Eq. (14) for the Findley fatigue criterion, and Eq. (17) for the modified Fatemi-Socie fatigue criterion, instead. For typical pearlitic rail steel, Fig. 4.14(a) and 4.14(b) present contours

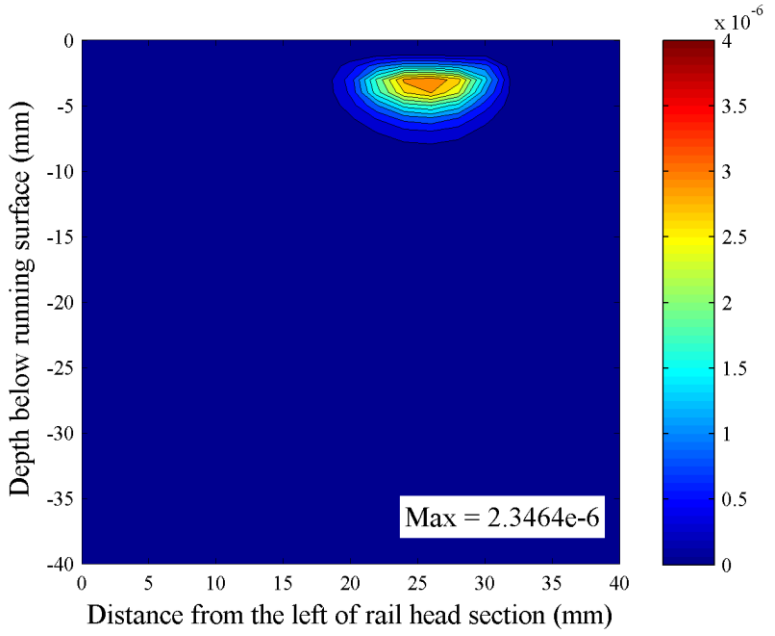

(a)

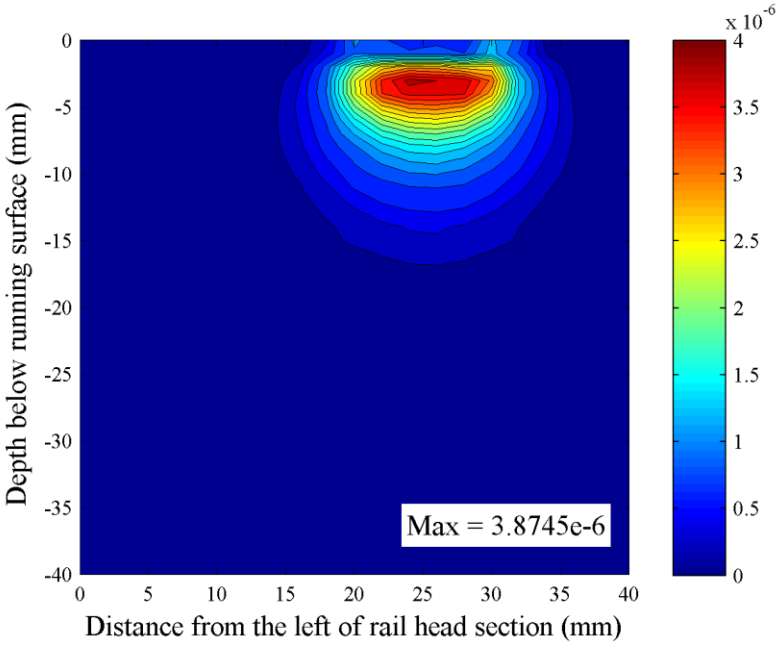

(b)

Fig. 4.14. Contours of fatigue index per loading cycle for the 162 kN wheel load using: (a) Findley fatigue criterion (κ = 0.3), and (b) modified Fatemi-Socie fatigue criterion (η = 1).

of fatigue index per loading cycle calculated using the Findley fatigue criterion (κ = 0.3) and the modified Fatemi-Socie fatigue criterion (η = 1) respectively, for the 162 kN wheel load. The result shows that the modified Fatemi-Socie fatigue criterion predicts larger fatigue index per loading cycle than the Findley fatigue criterion. Note that, ideally, the fatigue index per cycle contours (Fig. 4.14(a) and 4.14(b)) should look very similar to the maximum fatigue index contours (Fig. 3.3 and 4.2) respectively. However, it is found that the contours of fatigue index per cycle are more localized to near-surface, while they are hardly observed at subsurface. These deviations are due to a nonlinear relationship between fatigue index and fatigue life such that a small change of fatigue index could result in much larger change of fatigue life; therefore, the fatigue index per cycle contours and the maximum fatigue index contours are represented with different resolutions.

Due to its validity in both low-cycle and high-cycle fatigue regimes and its capability to incorporate residual stresses into subsurface crack predictions, the modified Fatemi-Socie fatigue criterion, with η = 1, will be applied to study fatigue damages in a rail head for various amount of wheel loads in the Chapter V. Results will be used to develop a set of grinding schedules that maximize the service life of railroad rails.

The differences between the multi-axial fatigue model proposed in this study and the *T-gamma method* (Tunna et al. [10], Kalker [72], and Iwnicki [73]) should also be noted here. Using vehicle dynamics simulations, the T-gamma method calculates '*wear number*' as a product of applied traction (T) and creepage (gamma—defined as the difference in velocities of contacting surfaces with respect to their mean velocity

(Clayton and Hill [74])). The calculation provides an energy input that goes into plastic deformation and crack nucleation processes in the rail head and can be correlated to field observation of wear and RCF. In contrast to the proposed multi-axial fatigue model, which is the critical plane based approach and is capable to predict RCF in rail head at depth greater than 3 mm below running surface, the T-gamma method is energy-based and focuses on wear and RCF phenomena at or close to the running surface that is expected to be ground-out in this study. That is, the T-gamma method is intended to capture the surface behavior of the contact patch between a wheel and a rail. It may be possible to use the T-gamma method for the prediction of wear due to operations and incorporate the predicted wear results to rail grinding schedules. Defined in term of plastic shear strain accumulation, a similar model for wear and RCF prediction at or closed to running surface is given by Vasic et al. [75].

4.5 Conclusions

Conclusions on the modified Fatemi-Socie fatigue criterion

- The modified Fatemi-Socie fatigue criterion is able to incorporate residual stresses and strains into subsurface crack predictions, and it is applicable to both low-cycle and high-cycle fatigue applications.
- For both the 162 kN and 223 kN wheel loads, larger fatigue index at subsurface is predicted when accounting for residual stresses and strains. In some cases, this may serve as another possible crack nucleation site.

- As the participation of the normal stress term in the modified Fatemi-Socie fatigue criterion is low, the shear strain amplitude term dominates near-surface crack nucleation, representing a failure mechanism of materials with high ductility.
- As the participation of the normal stress term in the modified Fatemi-Socie fatigue criterion is high, both the normal stress and shear strain amplitude promote subsurface crack nucleation, representing a failure mechanism of relatively brittle material. However an application of the criterion to tensile-based damages is limited, as it is originally formulated according to shear-based damages.
- At near surface, the plane of fatigue crack nucleation is similar to surface shelling, while the one at subsurface is a mixed mode between the vertical and horizontal planes similar to longitudinal cracks.
- The normal coefficient of typical pearlitic rail steel, defined by η, is approximately equal to 1. Fatigue index at subsurface is smaller but finite compared to that found at near surface for this case.

Conclusions on a comparison between the Findley and modified Fatemi-Socie fatigue criteria

- Fatigue index contours predicted by both criteria are qualitatively similar.
- Both criteria agree well in critical plane prediction of both near-surface and subsurface fatigue cracks.

- As subsurface fatigue crack is increasingly observable, the modified Fatemi-Socie fatigue criterion predicts two near-surface crack nucleation sites: one to the left and another to the right of wheel-rail contact as looking into the transverse plane, while the Findley fatigue criterion predicts only one, located right below the wheel-rail contact.
- The modified Fatemi-Socie fatigue criterion predicts larger fatigue index per loading cycle in rail head than the Findley fatigue criterion does.

CHAPTER V

OPTIMIZATION OF GRINDING SCHEDULES

5.1 Introduction

Olver [76] classifies rolling contact fatigue (RCF) phenomenon in railway tracks as: 1) surface cracks, 2) subsurface cracks, 3) gauge corner cracks, 4) wear, and 5) complete fracture of rail. Localized plastic deformation from wheel-rail contact is considered as a root cause of the surface crack nucleation, either by low-cycle fatigue (LCF) or ratcheting (Grassie et al. [5], Smith [6], and Kapoor et al. [7]). When visible surface-type RCF cracks present, it can be eliminated by conventional corrective rail grinding through an appropriate routine maintenance, or a portion of rail can be cut-out and replaced by a new rail section. In contrast, the subsurface-type RCF cracks in rail head are hardly detected by visual inspection and can cause abrupt failure in rails when they go undetected (Tunna et al. [10], Ekberg and Kabo [11], and Smith [6]).

Results from fatigue analyses with critical plane approaches in Chapter III (stress-based) and Chapter IV (strain-based) show that tensile residual stresses found in rail head at subsurface region play a damaging role on fatigue life of rails. Larger fatigue damages—represented in term of *fatigue index*—are predicted when a presence of various shapes and types of inhomogeneities and pores are considered (Fry et al. [12]). These subsurface fatigue damages accumulate as loading cycles increase until they eventually form incipient fatigue cracks that could lead to rail fracture and failure. The current corrective grinding method does not incorporate the accumulation of subsurface

fatigue damages mentioned above; therefore, it mistakenly regards the newly after-grinding rail section as a damage-free rail, only with a shorter rail head, and fails to control the nucleation of subsurface cracks.

As shown in Chapters III and IV, without rail grinding, fatigue damages tends to accumulate within a limited regime, whether for the case of 1) the surface-crack dominated mode found in ductile materials, or 2) the combined surface and subsurface crack mode found in brittle materials. An increase of wheel load tends to move the location of peak fatigue index to greater depth, but with a relatively small influence. In this chapter, a systematic study of the influence of rail grinding on fatigue life of typical pearlitic rail steel is conducted. One-point contact configuration found in a tangent rail is assumed, and natural wear from wheel-rail contact is considered negligible. Using fatigue index per cycle results determined from the modified Fatami-Socie fatigue criterion for rail steels in Chapter IV, this chapter intends to: 1) investigate the benefits of rail grinding on fatigue life of rails , 2) create a framework of an optimization of rail grinding schedule with genetic algorithm (GA) that is applicable to one-point wheel rail contact mode and its variations, and 3) provide a set of rail grinding schedules that help maximizing the service life of rails before making rail replacements for the current case of study.

5.2 Rail Grinding Practice for Rolling Contact Fatigue

5.2.1 Introduction to Rail Grinding

Corrective rail grinding has been a common practice in railroad industry to eliminate surface cracks due to RCF, remove rail corrugations, and reshape rail heads (Frohling [77] and Grassie [78]). Grinding an amount of rail surface prohibits crack propagations, reduce dynamic loads due to rail corrugations, and reduce concentrated loads occurred in a contact between the deformed wheel and rail profiles (Magel et al. [79]). These help prolong the service life of rail, and also prevent unexpected failures of rail from surface crack propagations, which could lead to undesirable accidents or derailments. However as it mainly relies on visual inspection, application of the corrective grinding approach is limited for subsurface cracks. The proposed preventive grinding, instead, is designed to prevent the nucleation of cracks—both at surface and subsurface—throughout the service life of rail, and will be the area of focus in this chapter.

To find an optimal preventive grinding plan, researchers are interested in two main questions (Grassie et al. [5]). The first question is: what is the optimal grinding schedule, covering both frequency and amount of material to be ground out? The second question is: what rail profiles should be used for grinding to minimize impact load from wheel-rail contact? This project intends to deal with only the first question of the optimal grinding schedule and will assume that the profile of running surface of rail remains the same as the original one throughout grinding process.

5.2.2 Corrective Grinding Versus Preventive Grinding

The original grinding practice—called *'corrective grinding'*—are designed mainly to eliminate visible fatigue cracks as soon as they are detected (Magel et al. [79]). This method tends to grind out relatively large amount of material in each grinding cycle and still leaves a possibility of the failure from subsurface fatigue crack propagations, if they are undetected. To overcome such pitfalls in corrective grinding, *'preventive grinding'* is introduced with different philosophy. In preventive grinding, relatively thin layers of material at running surface are ground out frequently, working together with the natural wear, to prevent the nucleation of surface and subsurface cracks at the same time. A study of the influence of rail grinding on surface and subsurface crack nucleation is done by Satoh and Iwafuchi [80] by monitoring the micro-structural change within rail heads. Using the Findley fatigue criterion and including the residual stresses from measurements to an elastic rolling result, Jones [81] presents an analytical study suggesting that fatigue life of rails could increase by 200% when the preventive rail grinding is applied.

Preventive grinding is considered as artificial wear, in addition to the natural wear occurred in wheel-rail contact. Proper combinations of the controlled artificial wear and natural wear—yielding what so called *'Magic Wear Rate'*—in which together, theoretically, create an amount of wear required to just remove existing cracks on the running surface (Kapoor and Franklin [82], and Magel et al. [79]). If the combined wear rate is too small, surface cracks will either possibly grow upward to the running surface or downward into the rail head. The preventive rail grinding is currently planned based

on intuitive, experience, or historical data, without consideration of the possible subsurface fatigue crack nucleation. In this study, the proposed rail grinding schedules will represents only the artificial wear, with an assumption that the natural wear is minimal, and it will also take subsurface crack nucleation into consideration. Note that the amount of grinding in each grinding step also could be regarded as a combination of artificial and natural wears, if the amount of natural wear is known.

The Canadian Pacific Railway (CPR) presents that the 'Magic Wear Rate' in sharp curves is about 0.025 mm per Mega Gross Ton (MGT), providing approximately 750 MGT wear life for total allowable wear of 19 mm (Magel et al. [79] and Sroba et al. [4]). On the tangent tracks and mild curves, Magic Wear Rate decreases to 0.008 mm and 0.016 mm per MGT respectively. Ishida et al. [83] present that after the Central Japan Railway adopts a preventive grinding approach with grinding thickness of 0.08 mm for every grinding interval of 40 MGT, the number of squats—a type of surface defect (Sperry Rail Service [2])—has been steadily decreasing. However, the aforementioned grinding are designed mainly from experience, and it is still controversial among researchers that which of the following options would extend the fatigue life of rail better: 1) removing large amount of material with longer grinding interval, and 2) removing small amount of material with shorter grinding interval. This is also an issue to be investigated in this study through an optimization of grinding schedules.

Compared with other grinding methods, preventive grinding is arguably the most cost-effective grinding strategy without sacrificing safety (Frohling [77]). Grassie et al.

[5] provide a supporting calculation that a preventive grinding strategy with the rate of metal removal of 0.2 mm per 25 MGT could reduce the total cost of grinding and rail replacements by 40% for the Sweden's heavy haul railway. Sroba et al. [4] also report a reduction in yearly maintenance cost of the Canadian Pacific Railway (CPR), from $81 to $65 millions, and 300% increase of service life of rail when the preventive grinding is used (compared with the corrective grinding approach).

5.3 Optimization of Grinding Schedules with Genetic Algorithm

Genetic algorithm (GA) is a population-based optimization method that simulates natural evolution according to various parameter-controlled stochastic processes. Aarts and Lenstra [84], Eiben and Smith [85], and Mitchell [86] present comprehensive reviews on theory and applications of the single-objective optimization with GA. Eiben et al. [87] and Reed et al. [88] provide guidelines for parameter setting and control for *re-combination*, *mutation*, *parent-selection*, and *survivor selection* steps. A study by Eiben and Schippers [89] present capabilities of GA to find the global-optimal solution with a combined use of re-combination and mutation processes. Solutions to an optimization problem, called *individuals*, are encoded into a chromosome-like format that is able to capture the change in the solution-search landscape. Exploration in feasible region is performed by the mutation operators, which could abruptly change the components of individuals, therefore help preventing the optimization from getting stuck within the local optima. In contrast, re-combination operators tend to encourage the exploitation by combining good characteristics of two or more parents, giving the local

search capability. In this study, individuals are evolved only by mutation operators, which parameters will be adjusted accordingly for the global and local searches.

Persson and Iwnicki [90] apply GA to a design of railway wheel profiles by using a binary representation for individuals, and use a combination of contact stresses, wear, and stability of a railway truck as a *fitness function* (the quality of the solution). An application of GA on surface grinding operations of machine tools studied by Saravanan et al. [91] shows that GA outperforms the quadratic programming technique in cost optimization. Also, GA is reported to be more robust and more efficient in handling multi-objective functions. A comparison of the optimal solution from GA to other evolutionary computation techniques on the previous grinding problem is presented by Asokan et al. [92]. In this chapter, GA is applied to optimize a single-objective function of the service life of rail according to various constraints: i.e. total allowable grind-out thickness, grinding resolution, and maximum fatigue index accumulation.

5.4 Optimization Problem Formulation

Define indexes as:

N	= number of grinding steps	(N = 4, 5, 8, 10, 15, 20)
P	= number of representative wheel loads	(P = 5)
i	= order of grinding step	(i = 1,…,N)
j	= representative wheel loads	(j = 1,…,M)
k	= order of nodes of interest in rail head	(k = 1,…,861)

The decision variables are:

x_i = number of 'loading unit (LU)' applied before the i^{th} grinding step

y_i = grinding thickness of the i^{th} grinding step in millimeters

r = remaining fatigue life in LU before fatigue crack nucleation

The input parameter from fatigue analysis performed in previous chapter is:

$f_{k,i,j}$ = fatigue index (damage) per LU at node k at the i^{th} grinding step for the j^{th} wheel load

The optimization problem of rail grinding schedules can be written as:

$$\max \quad \sum_{i=1}^{N} x_i + r \qquad \text{(total fatigue life in LU)}$$

$$\text{s.t.} \quad \sum_{i=1}^{N} y_i = 20 \qquad \text{(total allowable grinding thickness)}$$

$$\sum_{i=1}^{N} \sum_{j=1}^{P} x_i f_{k,i,j} < 1 \qquad , k = 1,\ldots,861$$

(damage accumulation at each node)

$x_i = 0.1, 0.2,\ldots,\infty$ (discrete)

$y_i = 1, 2,\ldots, 20$ (integer)

$r = 0.1, 0.2,\ldots,\infty$ (discrete)

The objective of the optimization is to maximize the total fatigue life—defined in term of LU—with respect to the specified constraints. The equality in the total allowable grinding thickness constraint is a result of intuition and experience, which suggest a direct relationship between allowable grinding thickness and fatigue life of rails. The

resolution of the total fatigue life is 0.1 LU in this study to limit the feasible region of the optimization. Genetic algorithm (GA) is selected as a tool to solve this optimization problem and will be discussed in the next section.

5.5 Procedures

5.5.1 Representative Wheel Loads

In order to study the benefit of surface grinding on fatigue life of rails, a group of representative dynamic wheel loads and their corresponding number of wheel passages is chosen to represent a typical distribution of wheel loads and loading frequencies in a heavy-hauled corridor. Based on a field measurements of a train with a 173 kN wheel load passing at 64 km/h reported by Joy et al. [93], five representative dynamic wheel loads of 125, 144, 162, 180, and 197 kN, and their corresponding number of wheel passages of 730, 6150, 13820, 8450, and 1390 respectively are statistically selected to represent a loading spectrum in discreet manner. This altogether presents a *loading unit (LU)* that will be used as a measure of total fatigue life in the optimization step.

Finite element analyses of wheel-rail contact and fatigue damage analyses with the Fatemi-Socie fatigue criterion are performed for each wheel load for the *fatigue index per cycle* results. Fatigue index per cycle is determined by Eq. (17) presented in Chapter IV for typical pearlitic rail steel with $\eta = 1$. Frequencies of loading per 1 LU will be used to calculate the total fatigue index accumulation per LU for each wheel load. Assuming linear combinations of fatigue accumulation among all wheel loads with the *Miner's rule* (Bannantine et al. [48]), combining total fatigue index of all five

representative wheel loads gives the total fatigue damage as a result of 1 LU. The larger the number of LU a railroad rail can withstand, the longer the fatigue life is, and the better the grinding schedule performs. Since rail steel is considered as a brittle material, crack nucleation and early growth processes consume most of its fatigue life, and material will fail when the total fatigue index accumulation of such a point of interest in the rail head reaches unity. Note that the Miner's rule is used in this study for simplification, such that fatigue index results from different wheel loads are linearly combined regardless of the order of loading.

It should be noted that the fatigue index calculated from the Fatemi-Socie fatigue criterion could be either positive or negative, depending on the amount of compressive stress at the node of interest. Positive fatigue index indicates the deterioration of the rail, while negative fatigue index will extend the fatigue life of rail, which may not be realistic. In this study, wherever the fatigue index is negative will be forced to be zero fatigue index, providing conservative optimal grinding schedules.

5.5.2 Influence of Rail Grinding on Rolling Contact Stresses

An optimization of rail grinding is designed according to a grinding resolution of 1 mm in thickness. As a result, RCF results for every grinding step are required as an input of the optimization. For example, given that there are five representative wheel loads with 20 mm allowable grinding thickness, total number of simulations required to create a database of fatigue index at different stages of grinding is 105 cases. For each simulation, six rolling cycles is required for residual stresses to reach the steady state.

Such an amount of simulation of wheel-rail contact with material plasticity is very computationally expensive, and perhaps, prohibitive. Instead, an assumption that there is no significant change of the rolling stresses in rail head among different stages of grinding is made, such that mapping of the rolling stresses and strains of the original rail profile to other grinding steps is allowed. This will reduce the number of simulations required to 5 cases. In order to validate this assumption, a finite element analysis of a rail being ground out for 15 mm with the same running surface profile, shown in Fig. 5.1, is performed for three rolling cycles. The von-Mises stress results from the simulation and the one with the original rail profile are compared to validate the proposed assumption.

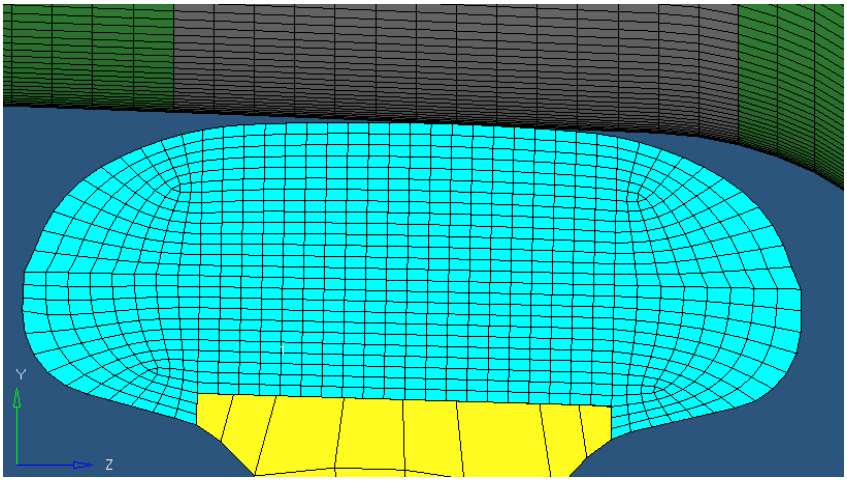

Fig. 5.1. A rail profile after 15-mm-ground-out.

5.5.3 Fatigue Index Database Preparation

There are 861 nodes of interest (41 rows and 21 columns) in the center of rail head of a cross-section located at the middle of rolling path as previously shown in Fig.

2.8(b) in Chapter II. For each representative wheel load, a relationship between the Fatemi-Socie fatigue index and fatigue life (Eq. (17)) for typical pearlitic rail steel is used to determine number of cycles to crack nucleation of all nodes in the original (no-grinding) rail profile. Calculated as a reciprocal of number of cycles to failure, the fatigue index per cycle is stored in a database as the step before first grinding. Counting from running surface, mapping the result of nodes in the first row (21 nodes) to the second row, the second row to the third row, and so on gives a result of fatigue index per cycle after grinding the running surface out for 1 mm. Now the first row of nodes is considered to be ground out and imposed by zero fatigue index as no further fatigue damage accumulation. Mapping process is performed repeatly for the cases of 2 mm-grinding, 3 mm-grinding, and so on until 20 mm-grinding—the final step. At the end, a database of grinding process of all representative wheel loads is stored for using in the optimization of grinding schedules by tracking fatigue damage accumulation at each node throughout the grinding process.

5.5.4 Representation of Individuals for Genetic Algorithm

Information of an *individual* (a solution to the problem) needs to be properly encoded into a format that allows the variation of each unit of the individual. In this study, since the objective is to maximize the total loading unit allowed before any cracks would nucleate, individuals are encoded into a chromosome-like string with units representing: 1) amount of loading unit (LU), and 2) incremental grinding thickness (mm) for every grinding step. Fig. 5.2 presents an example of individual with 3 grinding

steps. Note that the amount of loading unit at the end of individual (1.5 LU in Fig. 5.2) indicates the remaining fatigue life of rail after final grinding before crack nucleation. The total allowable grinding thickness is 20 mm in this study.

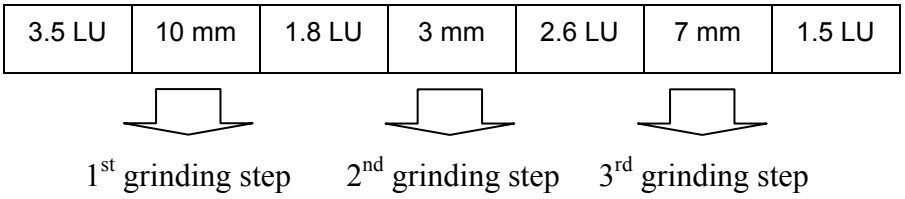

Fig. 5.2. A schematic representation of an individual with 3 grinding steps for GA.

Lengths of the string of individuals vary as the total number of grinding step changes. For example, an individual representing four-grinding-step schedule will consist of nine units, while an individual representing six-grinding-step schedule will consist of thirteen units. General information about grinding schedule: i.e. total grinding thickness, total loading units, and direction cosines of a plane of a node with largest fatigue index is appended to individuals, but they do not involve in evolutionary process. A set of number of individuals is called *population*.

The following is an example of the calculation of fatigue index accumulation of all nodes of interest due to the 3-step grinding schedule shown in Fig. 5.2. Firstly, total number of wheel passages for 3.5 LU is calculated for each wheel load. Using the fatigue index per cycle result of the no-grinding case in the database, fatigue index accumulation for each wheel load is determined, and combined into the total fatigue

index accumulation for the no-grinding step. Repeating the same procedure for the first grinding step with 1.8 LU, but using the fatigue index per cycle result of 10 mm-grinding case instead, yields additional fatigue index accumulation after the first grinding step. Similarly, with additional 3 mm and 7mm grinding in the second and third grinding steps, the fatigue index per cycle result of 13 and 20 mm-grinding cases are used for fatigue calculations corresponding to the 2.6 and 1.5 LU respectively. For this individual, the total grinding thickness is 20 mm (10 mm + 3 mm + 7 mm), and the total allowable loading unit is 9.4 LU (3.5 LU + 1.8 LU + 2.6 LU + 1.5 LU). However, the feasibility of this individual must be checked if it satisfies the imposed constraints. In this study, the constraints are: 1) the upper and lower bounds of total allowable loading units, and 2) total fatigue index accumulation of each node must be not greater than unity. An individual is considered infeasible if it violates any of the constraints, and must be adjusted accordingly. Note that, as described earlier, the total grinding thickness is forced to remain 20 mm during evolution processes.

5.5.5 Deterministic Grinding Schedules with a Constantly Fixed Loading Unit and Grinding Thickness

A deterministic approach is applied to study a grinding strategy that is least complicated to implement. This is similar to grinding plans currently applied in railroad industry, but designed from fatigue damage analyses, instead of pure intuition or experience. Constrained by the 1 mm grinding resolution, a non-integer grinding increment is not allowed in this study; therefore, for a total grinding thickness of 20 mm,

only 4, 5, 10, and 20 grinding steps are investigated. The loading unit (LU) is presented in one decimal place throughout this chapter.

5.5.6 Optimization of Grinding Schedules with Genetic Algorithm

Two optimization strategies with different type of starting populations are applied in this study. Considered as a knowledge-based approach, the first strategy uses a set of individuals created by the deterministic approach in 5.4.5 as a starting population. In contrast, the starting population in the second searching strategy is randomly created, providing more diversified group of individuals in the feasible region; thus, encouraging global search and avoiding the solution to get stuck in local optima.

5.5.6.1 Optimization with Deterministic Starting Population

The deterministic and heuristic methods are synergistically used in the optimization. First, the domain of solution searches will be narrowed down by the deterministic approach previously used in 5.5.5; therefore, only 4, 5, 10, and 20 grinding steps can be investigated. The deterministically-created starting populations are given in Appendix B. These starting populations will be improved by either: 1) mutating only LU components or 2) mutating both LU and grinding thickness components, according to stochastic algorithms that control the probability to choose which component to be mutated and its corresponding amount of mutation. The mutation of each LU components are independent from each other, while the mutation of grinding thickness components must be done in pair such that an increase of a unit must follow a decrease

of the same amount, or vice versa, of another unit to maintain a total grinding thickness of 20 mm. In this study, the searching of solution consists of two consecutive steps: 1) evolutions with relatively large mutation rate to explore feasible region until no significant improvement is found, and 2) evolutions of the population from the first step with relatively small mutation rate for a local search. Parameters used in both steps are given in Appendix C. Fig. 5.3 is the schematic of optimization procedures. With 20 individuals in starting population, the procedures of both evolutionary steps are the same, as that follows.

1. Stochastically mutate the LU components or grinding thickness components of all individuals in the original population. The twenty newly created individuals must satisfy all imposed constraints. Note that after a certain number of mutation trials, if a new feasible individual from mutating an original individual cannot be found, a feasible individual from the 'backup' population (another set of pre-defined feasible solutions) will be brought in as a new individual instead.
2. Combine the new set of individuals to the original population, yielding a set of forty individuals. Sort all individuals in descending order respected to the total LU allowed (the objective function).
3. Select individuals for the new generation of population according to the following selection method: 1) six individuals randomly picked from the first top ten individuals of sorted list, 2) six individuals randomly picked from a set of individuals ranked from 11 to 20, 3) four individuals randomly picked

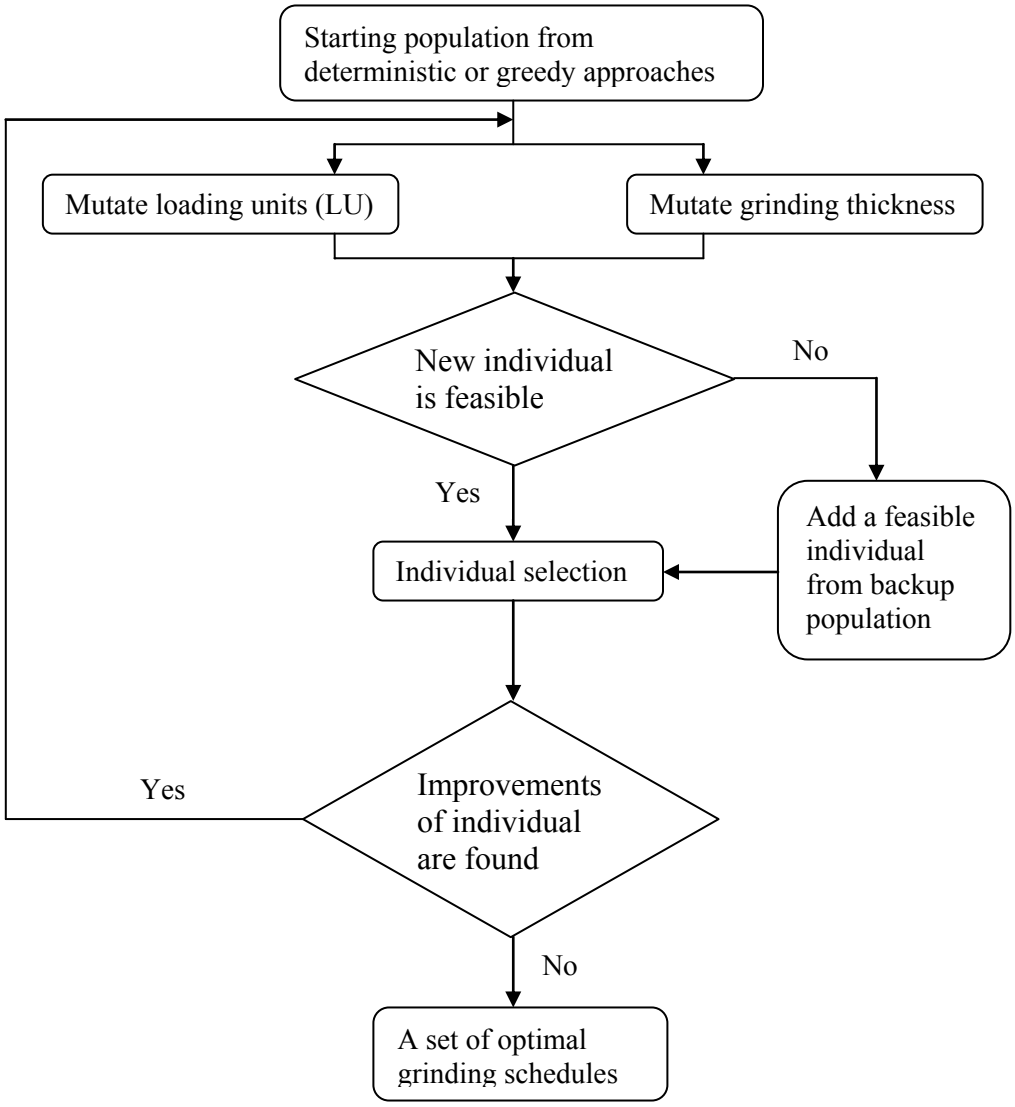

Fig. 5.3. A schematic showing optimization procedures with GA.

from a set of individuals ranked from 21 to 30, and 4) four individuals randomly picked from a set of individuals ranked from 31 to 40.

4. Check against the desired improvement rate if there is an improvement on either the maximum or the average of the total LU allowed in the new generation of individuals.
5. Repeat step 1 to 4 until no improvement is found for certain consecutive trials.

5.5.6.2 Optimization with Randomly-Created Starting Population

A set of twenty individuals are randomly generated for the cases of 4, 8, 10, and 15 grinding steps to be the starting population. Individuals must not violate the following constraints.

1. Loading unit must be presented in one decimal place.
2. Total grinding thickness must equal to 20 mm.
3. Fatigue damage accumulation in every node must not greater than unity.
4. No repetition of individuals.

Using above individuals as the starting population, the optimization of grinding schedules is performed as steps described in 5.5.6.1.

5.6 Results and Discussion

5.6.1 Fatigue Index per Loading Cycle of the Representative Wheel Loads

Applying the Fatemi-Socie fatigue criterion to the rolling stress results from the sixth rolling cycle of all five representative wheel loads, Fig. 5.4 - 5.8 show their corresponding contours of fatigue index per loading cycle, which are determined by Eq. (17) for typical pearlitic rail steel with η = 1. In general, greater amount (cross-section area) of material that experiences damage—both in width and depth—is predicted as wheel loads increase. In term of magnitude, similarly, the peak fatigues index presented at 2-3 mm below running surface are proportional to the wheel load up to 162 kN. Then as the fatigue index contours grow deeper to subsurface region, a drop of peak fatigue index at near-surface is observed when wheel loads change from 162 to 180 kN, possibly considered as the critical wheel load range where the subsurface fatigue cracks start to become another possible mode of failure. The increase of fatigue index is proportional to wheel loads again after this critical point. According to above observations, subsurface fatigue cracks would be increasingly common in the heavier wheel loads.

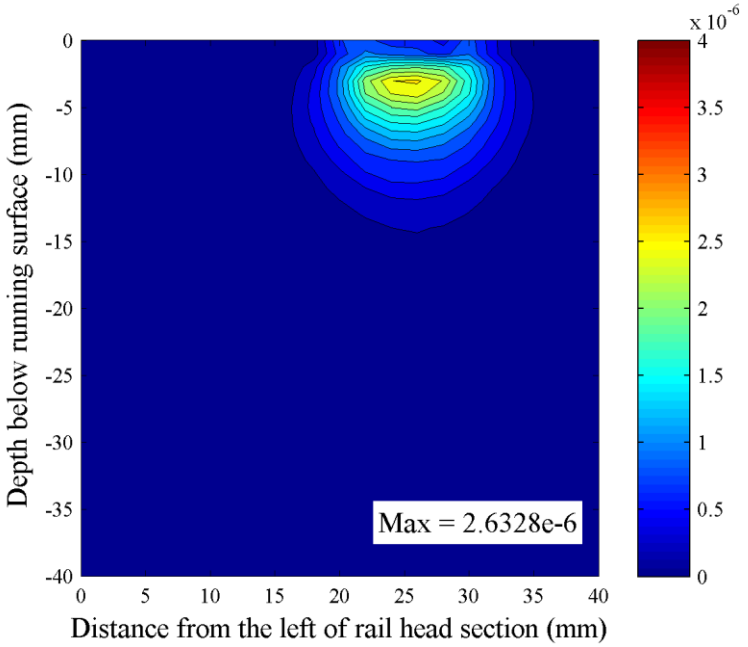

Fig. 5.4. A contour of maximum fatigue index per loading cycle with the 125 kN wheel load for a typical rail steel (η = 1).

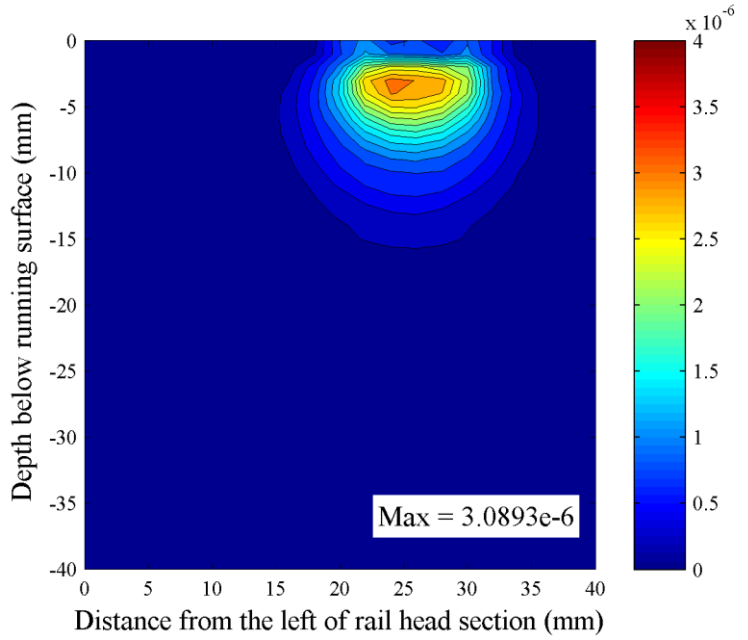

Fig. 5.5. A contour of maximum fatigue index per loading cycle with the 144 kN wheel load for a typical rail steel (η = 1).

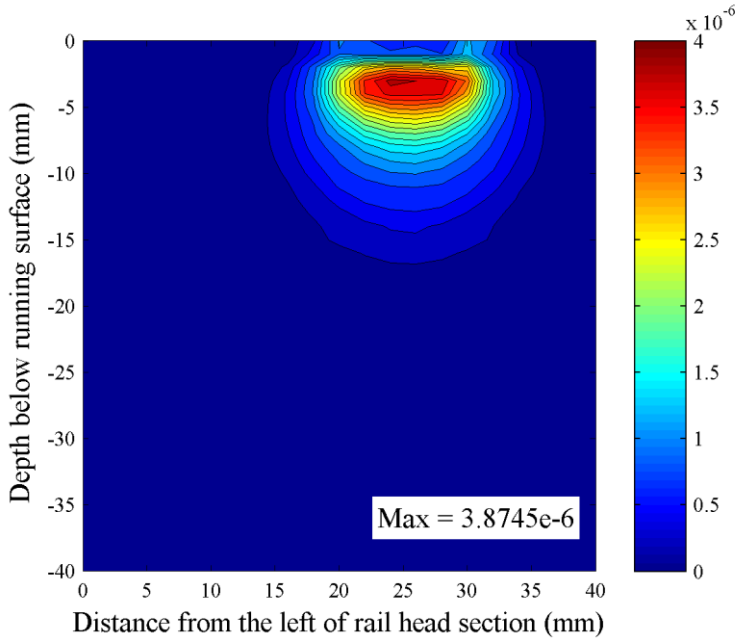

Fig. 5.6. A contour of maximum fatigue index per loading cycle with the 162 kN wheel load for a typical rail steel (η = 1).

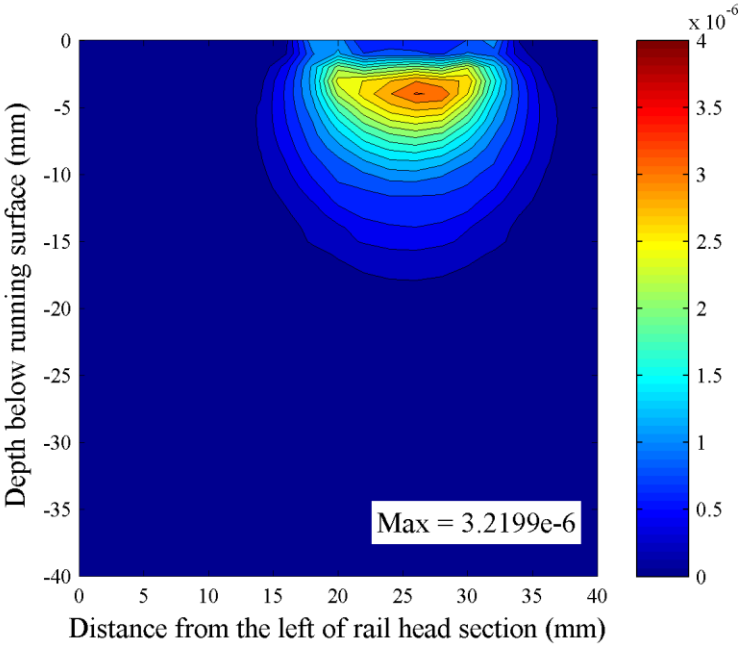

Fig. 5.7. A contour of maximum fatigue index per loading cycle with the 180 kN wheel load for a typical rail steel (η = 1).

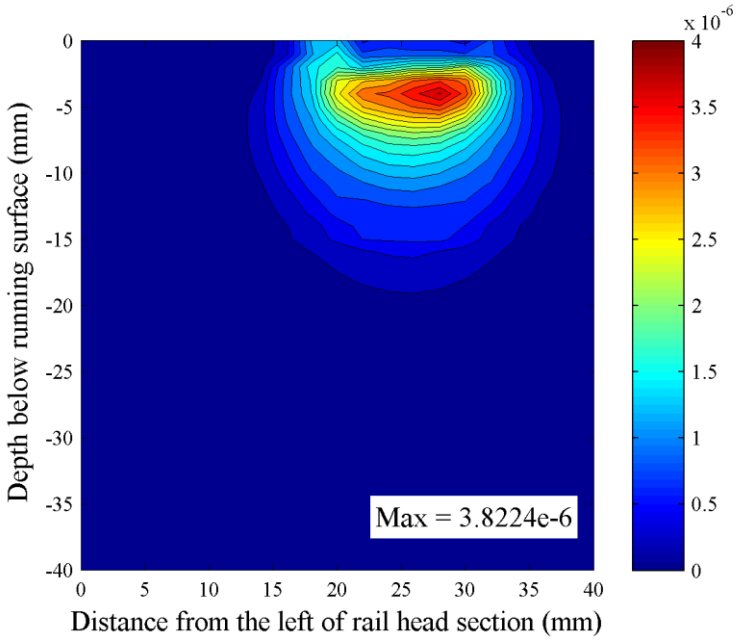

Fig. 5.8. A contour of maximum fatigue index per loading cycle with the 197 kN wheel load for a typical rail steel (η = 1).

5.6.2 Fatigue Life of Rails without Rail Grinding

Without an application of rail grinding and assuming minimal material loss from wear, Fig. 5.9 is the contour of fatigue index accumulation after 10.16 LU, where fatigue cracks begin to nucleate (fatigue index accumulation equals to 1) at around 3 mm below the running surface. The critical plane of the crack nucleation agrees with the horizontal plane as often seen in field tests as shelling. The service life of 10.16 LU will be used as a benchmark to evaluate the capability of different rail grinding schedules developed by the optimization in the next section.

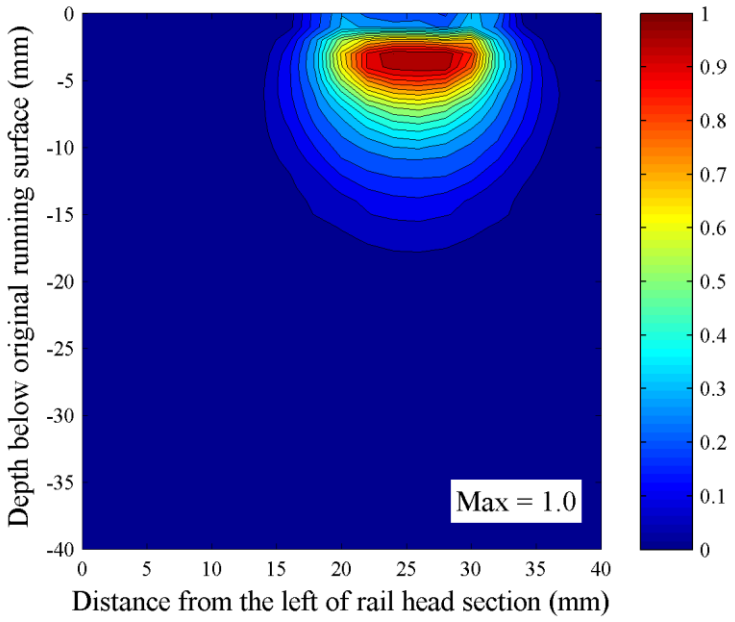

Fig. 5.9. A contour of maximum fatigue index accumulation at failure for a typical rail steel (η = 1) without rail grinding (total fatigue life = 10.16 LU).

5.6.3 A Comparison of Rolling Stresses between the Original and 15-mm-ground-out Rail Profiles

The von-Mises stress contours in the rail head at the third rolling cycle of the 15-mm-ground-out case (with a peak value of 439 MPa: see Fig. 5.10(a)) and the original rail head profile (with a peak value of 428 MPa: see Fig. 5.10(b)) are qualitatively similar. With a 2.57% difference of the peak equivalent stresses and their agreeable contours, this justifies the use of the proposed rolling stresses mapping scheme that is described earlier.

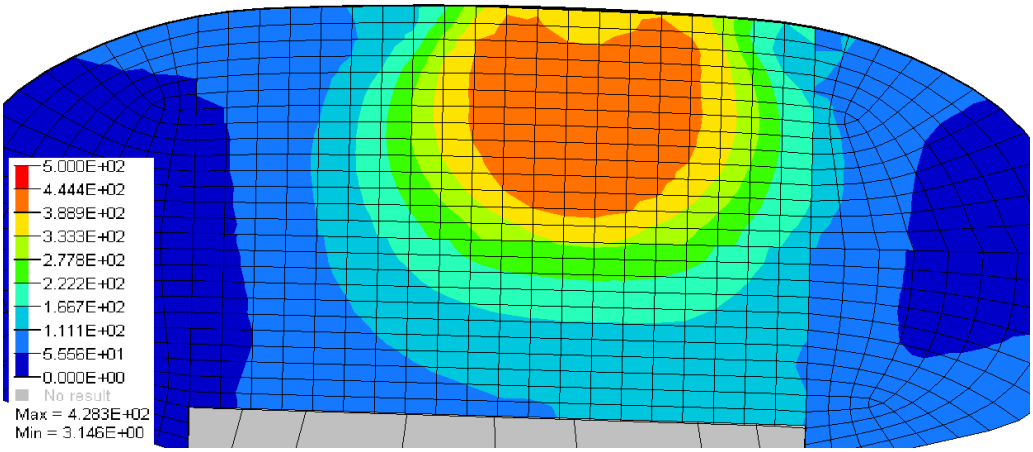

(a)

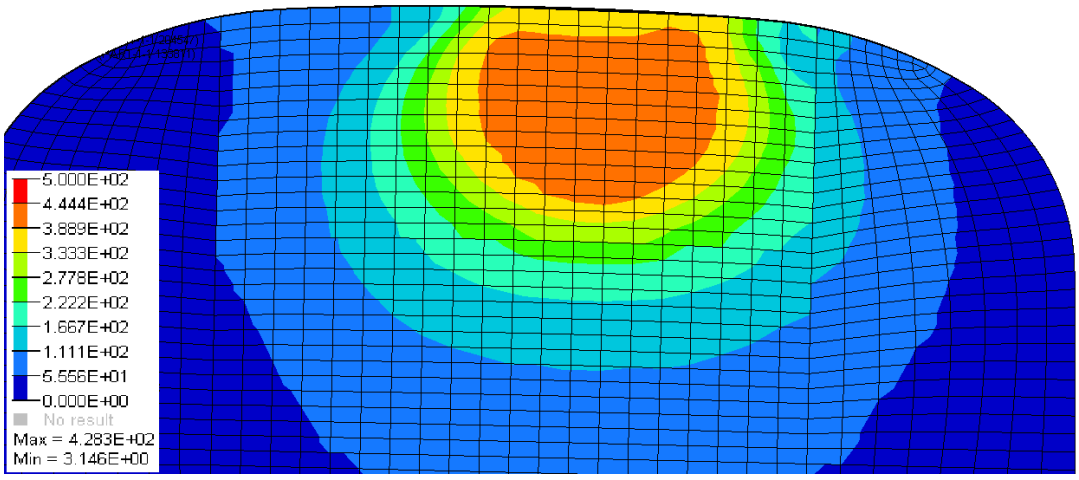

(b)

Fig. 5.10. von-Mises stress contours of a cross-section of rail located at the middle of rolling path at the third rolling cycle with 162 kN wheel load of: (a) a rail profile after 15 mm grinding, and (b) an original rail profile.

5.6.4 Deterministic Grinding Schedules with a Constantly Fixed Loading Unit and Grinding Thickness

Table 5.1 is a set of grinding schedules, which LU and grinding thickness components remain a constant throughout grinding process, that give the best fatigue life for 4, 5, 10, and 20 grinding steps. The corresponding contours of the fatigue index accumulation for each grinding case are shown in Fig. 5.11 to 5.14, with the maximum fatigue index reported at the bottom-right of the figures. The horizontal white lines located at 20 mm below the running surface present the location of the final running surface before fatigue crack nucleation. Results of fatigue accumulations of material beyond these lines, which actually has been ground out, can be used to qualitatively determine the quality of the proposed grinding schedules. The greater the amount of material having fatigue index accumulation close to 1.0, the greater the material in rail head having been exercised, as a result, the better the grinding schedules are.

Without a need of an optimization by GA, the grinding schedules determined from a deterministic approach are able to increase fatigue life of rails about 200%, from 10.16 to 29.4 - 31.2 LU. The grinding schedule with 5 grinding steps provides the best fatigue life of 31.2 LU in this case. However, as seen in Fig. 5.11 to 5.14, the deterministic grinding schedules are not yet able to exhaust layers of ground-out material efficiently, and they are subject to further improvement by GA in the next section.

Depth of crack nucleation reported in Table 5.1 can also be used as another measure of the quality of grinding schedules. A grinding schedule that creates the first crack nucleation at above final running surface—20 mm below running surface—can be

further improved by a local search as the remaining material below final running surface has not been fully exhausted yet. The critical planes of crack nucleation in all cases agree with the horizontal plane as often seen in field tests as shelling.

Table 5.1

A set of grinding schedules from the deterministic approach

Number of steps	Total LU	Crack depth (mm)	Individual (LU | mm)										
4	30.5	23	6.1	5	6.1	5	6.1	5	6.1	5	6.1		
5	31.2	23	Individual (LU | mm)										
			5.2	4	5.2	4	5.2	4	5.2	4	5.2	4	5.2
10	29.7	20	Individual (LU | mm)										
			2.7	2	2.7	2	2.7	2	2.7	2	2.7	2	
			2.7	2	2.7	2	2.7	2	2.7	2	2.7	2	2.7
20	29.4	20	Individual (LU | mm)										
			1.4	1	1.4	1	1.4	1	1.4	1	1.4	1	
			1.4	1	1.4	1	1.4	1	1.4	1	1.4	1	
			1.4	1	1.4	1	1.4	1	1.4	1	1.4	1	
			1.4	1	1.4	1	1.4	1	1.4	1	1.4	1	1.4

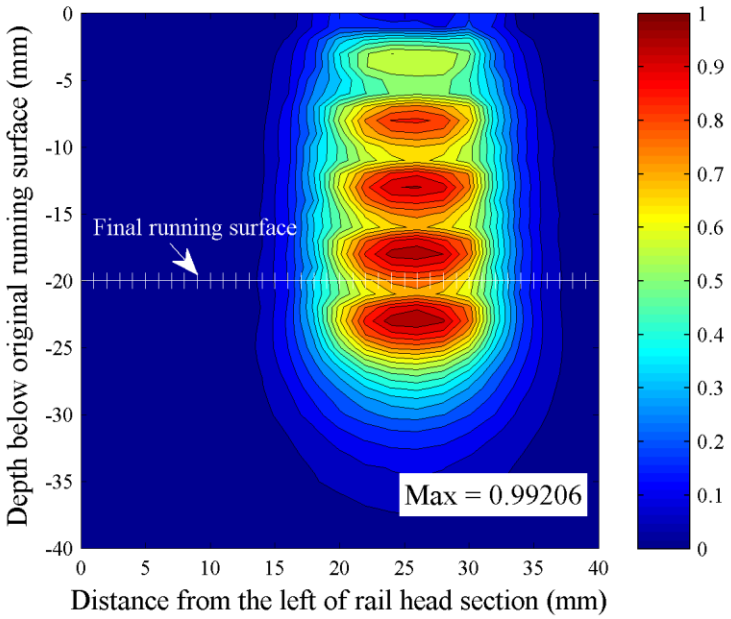

Fig. 5.11. A contour of maximum fatigue index accumulation for the 4-step grinding with a fixed grinding rate of 6.1 LU/5 mm and 30.5 total LU.

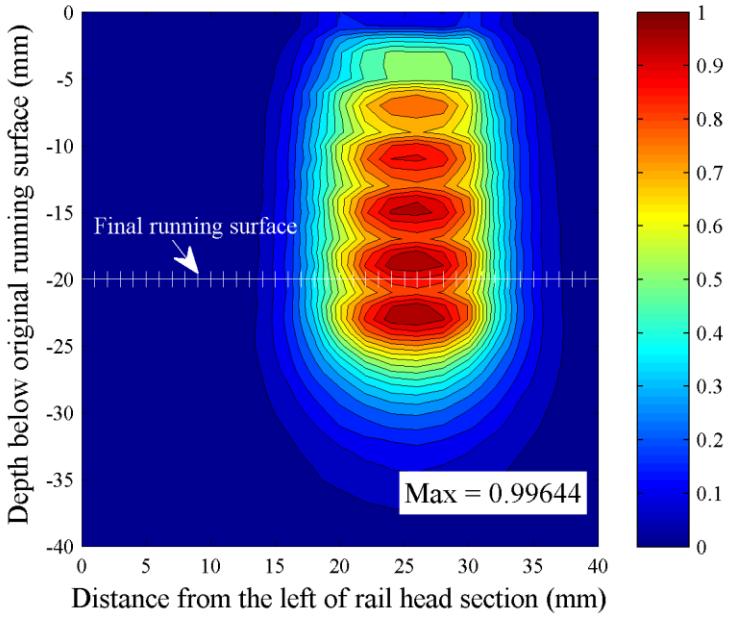

Fig. 5.12. A contour of maximum fatigue index accumulation for the 5-step grinding with a fixed grinding rate of 5.2 LU /4 mm and 31.2 total LU.

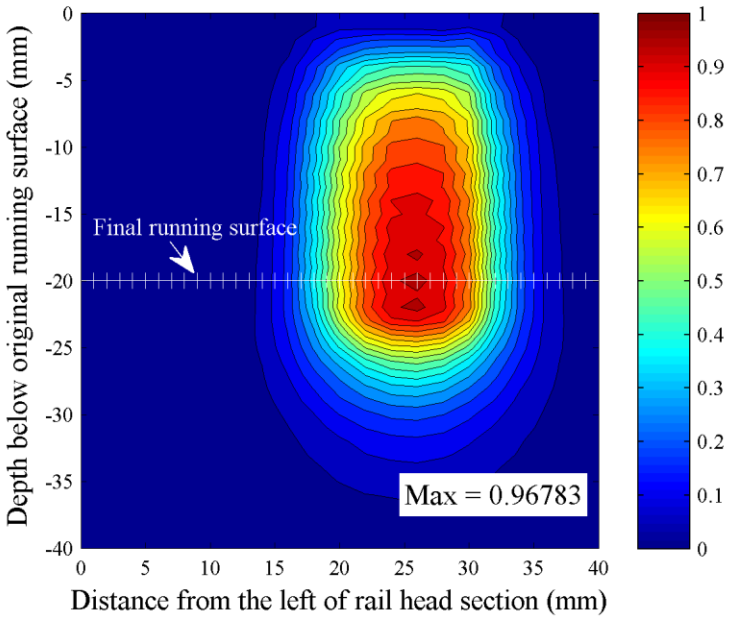

Fig. 5.13. A contour of maximum fatigue index accumulation for the 10-step grinding with a fixed grinding rate of 2.7 LU /2 mm and 29.7 total LU.

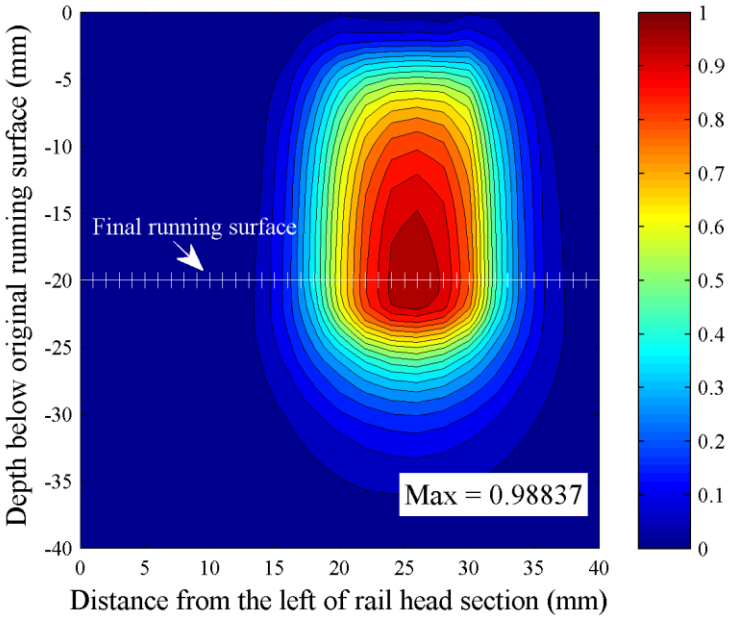

Fig. 5.14. A contour of maximum fatigue index accumulation for the 20-step grinding with a fixed grinding rate of 1.4 LU /1 mm and 29.4 total LU.

5.6.5 Grinding Schedules from Various Optimization Strategies

In order to explore searching space in feasible region, two sets of starting population are used for the optimization with GA in this section. Individuals of the first set, including ones reported in 5.5.4, are created by the deterministic approach, while individuals of the second set are created stochastically. Note that all individuals must, and always, satisfy the constraints of the 20 mm total grinding thickness and the upper limit of fatigue accumulation. List of the starting populations is reported in Appendix B. The parameters of the optimization with GA are reported in Appendix C. Two mutation methods: 1) mutating only LU components, and 2) mutating both LU and grinding thickness components, are applied to optimize the deterministically-created population, while only the second mutation method is applied to the stochastically-created population. As a result, three groups of optimization results are reported below.

5.6.5.1 Results of the Deterministically-Created Population with Only LU Mutations (Group 1)

Limited to only mutations of LU components, Tables 5.2 – 5.5 are the five best grinding schedules from the optimization for the cases with 4, 5, 10, and 20 grinding steps respectively. All grinding schedules show improvements on fatigue life of rails as the total LU ranging from 33.5 to 35, or 230 to 244% increase compared to one of the no-grinding case (10.16 LU). In average, the more the number of grinding steps, the better the fatigue life is. However, this relationship will be further investigated when the local search with GA is applied to improve the grinding schedules reported in this

section. The depths of first crack nucleation found in all grinding cases vary throughout the rail head, from 6 – 23 mm, also suggesting a possible improvement with the local search to move cracking location down to the 20 mm-plus region.

Table 5.2

Optimization results of the deterministic starting population with 4 grinding steps and only LU mutations

Max. Index	Total LU	Crack depth (mm)	Individuals (LU | mm)								
0.99503	33.9	23	10.1	5	5.5	5	6.1	5	6.1	5	6.1
0.99354	33.6	23	9.8	5	5.6	5	6	5	6.1	5	6.1
0.99460	33.6	23	9.8	5	5.5	5	6.1	5	6.1	5	6.1
0.99956	33.6	18	10.1	5	5.7	5	5.3	5	6.5	5	6
0.99139	33.5	18	9.8	5	5.5	5	6.1	5	6.1	5	6

Table 5.3

Optimization results of the deterministic starting population with 5 grinding steps and only LU mutations

Max. Index	Total LU	Crack depth (mm)	Individuals (LU | mm)										
0.99496	34.7	6	10.1	4	4	4	5.5	4	4.6	4	5.5	4	5
0.99787	34.6	15	10.1	4	4	4	5.5	4	5	4	5	4	5
0.99720	34.6	23	9.7	4	4.2	4	5.2	4	5.1	4	5.2	4	5.2
0.99928	34.5	23	9.4	4	4.3	4	5.2	4	5.2	4	5.2	4	5.2
0.99907	34.5	23	9.5	4	4.2	4	5.2	4	5.2	4	5.2	4	5.2

Table 5.4

Optimization results of the deterministic starting population with 10 grinding steps and only LU mutations

Max. Index	Total LU	Crack depth (mm)	Individuals (LU | mm)										
0.99657	34.9	22	9.7	2	0.3	2	3.8	2	2.1	2	3.3	2	
			2.4	2	1.8	2	2.7	2	3.3	2	2.6	2	2.9
0.99638	34.9	6	9.2	2	0.9	2	3.6	2	2.4	2	2.6	2	
			3.1	2	0.6	2	5	2	1	2	0.2	2	6.3
0.99857	34.8	18	9.7	2	0.4	2	3.8	2	1.2	2	3.3	2	
			2.4	2	2.2	2	3	2	3.3	2	1.7	2	3.8
0.99749	34.8	23	9.2	2	0.6	2	3.6	2	2.7	2	2.4	2	
			3.1	2	0.4	2	5	2	1.4	2	0.1	2	6.3
0.99897	34.6	23	9.2	2	0.3	2	3.6	2	2.7	2	2.4	2	
			3.1	2	0.5	2	5	2	1.4	2	0.1	2	6.3

Table 5.5

Optimization results of the deterministic starting population with 20 grinding steps and only LU mutations

Max. Index	Total LU	Crack depth (mm)	Individuals (LU | mm)										
0.99931	35.2	16	9.1	1	0.5	1	0.5	1	1.4	1	0.6	1	
			2.7	1	0.4	1	1.6	1	1.7	1	1.2	1	
			0.9	1	0.3	1	2.5	1	1.4	1	2	1	
			0.2	1	1.4	1	1.4	1	0.6	1	1.2	1	3.6
0.99917	35	23	6.8	1	1.4	1	0.9	1	2.6	1	0.5	1	
			1.4	1	1.2	1	1.7	1	1.4	1	1.1	1	
			2	1	0.5	1	1.6	1	1.4	1	1.7	1	
			1.4	1	0.4	1	0.3	1	0.6	1	1.4	1	4.7
0.99604	35	16	8.2	1	0.4	1	1.4	1	1.2	1	1.4	1	
			1.4	1	0.6	1	2.4	1	1.4	1	0.7	1	
			2	1	0.3	1	1.2	1	2.4	1	1.4	1	
			0.9	1	1.8	1	0.3	1	2.7	1	0.1	1	2.8
0.99731	35	6	8.2	1	0.4	1	1.3	1	1.4	1	1.4	1	
			1.4	1	0.6	1	2.4	1	1.4	1	0.7	1	
			2	1	0.2	1	1.2	1	2.4	1	1.4	1	
			0.9	1	1.8	1	0.2	1	2.7	1	0.2	1	2.8
0.99775	35	22	9.1	1	0.5	1	0.5	1	1.4	1	0.6	1	
			2.7	1	0.4	1	1.6	1	1.7	1	1.2	1	
			0.9	1	0.3	1	2.5	1	1.4	1	1.2	1	
			0.2	1	2	1	1.4	1	0.6	1	1.2	1	3.6

5.6.5.2 Results of the Deterministically-Created Population with both LU and Grinding Thickness Mutations (Group 2)

Using the deterministic starting population, but allowing both grinding thickness and LU components to mutate to expand the searching space, Tables 5.6 – 5.8 are the five best grinding schedules from the optimization for the cases with 4, 5, and 10

grinding steps respectively. All grinding schedules show improvement on fatigue life of rails as the total LU ranging from 33.1 to 34.7, or 226 to 242% increase compared to one of the no-grinding case (10.16 LU). In average, the more the number of grinding steps, the better the fatigue life is. The depths of first crack nucleation found in all grinding cases vary throughout the rail head, from 3 – 23 mm, suggesting a possible improvement with the local search to move cracking location down to 20 mm plus region.

Table 5.6

Optimization results of the deterministic starting population with 4 grinding steps, and both LU and grinding thickness mutations

Max. Index	Total LU	Crack depth (mm)	Individuals (LU | mm)							
0.99940	33.8	13	9.6	5	5.9	5	6.1	5	6.1	5	6.1
0.99940	33.2	13	9.6	5	5.9	5	6.1	5	6.1	5	5.5
0.99871	33.1	12	10.1	5	5.3	4	5.3	6	6.5	5	5.9
0.99430	33.1	3	10.1	5	5.3	5	5.3	5	6.5	5	5.9
0.99871	33.1	12	10.1	5	5.3	4	5.3	6	5.9	5	6.5

Table 5.7

Optimization results of the deterministic starting population with 5 grinding steps, and both LU and grinding thickness mutations

Max. Index	Total LU	Crack depth (mm)	Individuals (LU | mm)									
0.98880	34.3	15	9.3	4	4.6	4	5.1	4	5.1	4	5.1	4	5.1
0.99042	34	15	8.5	4	5.1	4	5.1	4	5.1	4	5.1	4	5.1
0.97976	33.8	23	9.3	4	4.1	4	5.1	4	5.1	4	5.1	4	5.1
0.98167	33.8	6	9.3	4	4.6	4	4.6	4	5.1	4	5.1	4	5.1
0.98603	33.8	15	9.3	5	4.6	3	4.6	4	5.1	4	5.1	4	5.1

Table 5.8

Optimization results of the deterministic starting population with 10 grinding steps, and both LU and grinding thickness mutations

Max. Index	Total LU	Crack depth (mm)	Individuals (LU | mm)										
0.99782	34.7	22	9	2	0.9	1	1.4	2	3	2	2.1	1	
			2.1	2	2.9	3	3	1	1.5	3	4.2	3	4.6
0.98993	34.7	6	9.1	3	2.7	1	1.2	2	1.1	1	3.6	3	
			3.3	2	2.7	2	2.2	2	1.2	1	3.8	3	3.8
0.99092	34.6	16	9	2	1.1	2	1.4	1	3.3	2	1.7	1	
			2.1	3	2.9	2	3	1	1.7	3	4.2	3	4.2
0.99979	34.5	19	9.1	3	2.7	2	1.2	1	1.1	1	3.6	3	
			3.3	2	2.7	2	2.2	2	2.1	1	2.7	3	3.8
0.99732	33.8	22	5.2	1	3	3	3	1	2.7	2	1.9	3	
			3.9	2	2.6	2	2.7	2	2.7	2	1.7	2	4.4

5.6.5.3 Results of the Stochastically-Created Population with both LU and Grinding Thickness Mutations (Group 3)

In this case, the searching space is considered to be most generalized, as the starting population is stochastically created, and the mutation of both LU and grinding thickness components is allowed. Tables 5.9 – 5.12 are the five best grinding schedules from the optimization for the cases with 4, 5, 8, 10, and 15 grinding steps respectively. All grinding schedules show improvement on fatigue life of rails as the total LU ranging from 31.4 to 35.2, or 209 to 246% increase compared to one of the no-grinding case (10.16 LU). The fatigue life improvements are comparable, but taking twice as much runtime, to those optimized from the deterministically-created population in 5.5.5.1 and 5.5.5.2. This suggests the benefit of using the knowledge-based starting population in an

optimization with GA in this study. Due to stochastic process, the relationship between number of grinding steps and fatigue is less apparent, but remaining proportional. The depths of first crack nucleation found in all grinding cases vary throughout the rail head, from 4 – 23 mm, suggesting a possible improvement with the local search to move cracking location down to 20 mm plus region.

Table 5.9

Optimization results of the stochastic starting population with 4 grinding steps, and both LU and grinding thickness mutations

Max. Index	Total LU	Crack depth (mm)	Individuals (LU | mm)								
0.99219	32.5	23	9.8	6	6.6	7	7.2	3	3	4	5.9
0.98396	32.2	23	9.8	5	5.4	7	7.2	4	4	4	5.8
0.99678	32.1	22	9.4	5	5.7	7	7.5	5	4.8	3	4.7
0.99995	31.5	23	9.4	7	7.4	2	0.4	5	7.4	6	6.9
0.99922	31.4	22	10.1	6	6.4	6	6.8	6	6.6	2	1.5

Table 5.10

Optimization results of the stochastic starting population with 5 grinding steps, and both LU and grinding thickness mutations

Max. Index	Total LU	Crack depth (mm)	Individuals (LU | mm)									
0.99929	34.1	5	8.6	3	3.8	3	4	4	5.5	5	6	5	6.2
0.99967	33.9	17	9.9	4	4.2	2	1.4	3	5.5	5	6.2	6	6.7
0.99850	33.8	6	9.9	4	4.2	2	1.3	3	5.5	5	6.2	6	6.7
0.99729	33.8	8	8.6	3	3.6	3	4.4	4	5	5	6	5	6.2
0.99731	33.7	23	8.6	3	3.4	3	4	4	5.5	5	6	5	6.2

Table 5.11

Optimization results of the stochastic starting population with 8 grinding steps, and both LU and grinding thickness mutations

Max. Index	Total LU	Crack depth (mm)	Individuals (LU | mm)									
0.99633	34.1	5	5.8	2	5.2	4	5.2	4	4.7	2	0.5	1
			3.1	3	3.2	1	1.7	3	4.7			
0.99983	34	4	1	1	9.2	5	5.7	3	2.5	3	5.1	3
			2.4	1	1.4	1	1.2	3	5.5			
0.99757	34	23	5.8	2	5.2	4	5.2	4	4.7	2	0.4	1
			3.1	3	3.2	2	1.7	2	4.7			
0.99983	33.9	4	1	1	9.2	5	5.7	3	2.5	3	5.1	3
			2.6	1	1.1	1	1.2	3	5.5			
0.99449	33.6	19	2.1	1	7.8	3	2.4	3	4.5	2	1.8	2
			2.8	1	1	4	6.3	4	4.9			

Table 5.12

Optimization results of the stochastic starting population with 10 grinding steps, and both LU and grinding thickness mutations

Max. Index	Total LU	Crack depth (mm)	Individuals (LU | mm)										
0.99781	34.3	4	9.2	2	1.5	3	1.6	1	4.5	3	2.6	1	
			1.6	3	3.9	2	0.8	1	1.3	1	1.4	3	5.9
0.99821	34.3	7	8	1	1.1	2	1.9	2	4	3	2.3	1	
			0.7	2	4.9	4	5	2	1.1	2	1.9	1	3.4
0.98818	34	13	8.3	4	4.9	2	0.6	1	1.2	1	1.8	1	
			2.4	2	2.6	2	2.4	3	4.4	3	0.7	1	4.7
0.99571	33.9	19	9.8	3	1.3	1	1.1	1	0.1	2	5.7	3	
			1.7	2	3.8	1	0.7	3	5.2	3	2.1	1	2.4
0.98966	33.8	23	8	1	1.7	2	1.9	3	4	2	2.3	1	
			0.7	3	4.9	2	1.6	1	1.3	3	2.1	2	5.3

Table 5.13

Optimization results of the stochastic starting population with 15 grinding steps, and both LU and grinding thickness mutations

Max. Index	Total LU	Crack depth (mm)	Individuals (LU | mm)										
0.99888	35.2	16	9.4	1	0.4	1	0.6	1	0.2	2	4.6	2	
			2	1	1	1	0.4	1	3	3	3.6	1	
			1.5	1	0.4	1	0.2	1	2.3	2	1.2	1	4.4
0.99729	35.1	16	6.6	1	0.7	1	3.3	2	1.1	1	0.9	1	
			2.7	1	1.4	2	1.6	2	4.3	2	1.2	1	
			2	1	1	1	1.5	1	1.5	1	0.5	2	4.8
0.99452	34.8	5	8.8	1	0.8	2	2.3	1	0.1	1	2.5	1	
			0.3	1	2.3	1	1.1	2	2.7	1	0.2	1	
			3.1	2	1.4	2	4.1	2	0.9	1	0.7	1	3.5
0.99945	34.8	16	6.6	1	0.7	1	3.3	2	1.1	1	1	1	
			2.7	1	1.4	2	1.6	2	4.3	2	1.2	1	
			2	1	1	1	1.5	1	1.5	1	0.1	2	4.8
0.99523	34.7	23	9.4	2	0.8	1	0.7	1	0.2	1	3.5	2	
			2.9	1	0.7	1	0.5	1	2.7	3	3.6	1	
			0.9	1	0.5	1	0.3	1	2.3	2	1.3	1	4.4

5.6.6 Local Search Optimization with Genetic Algorithm

Best individuals from the first exploratory search of the three groups previously reported in Tables 5.1 – 5.13 are subject to refinements with the optimization with local search. Parameters used in the local search are given in Appendix B. Narrowing down the search space by incrementally adjusting LU and grinding thickness components by 0.1 LU and 1 mm respectively, Tables 5.14 - 5.17 present the improvement of the grinding schedules in Group 1. The order of the mutated individuals remains as same as that of the starting set. For example, the first grinding schedule in Table 5.14 is a result

of an optimization of the first grinding schedule in Table 5.2 and so on. The optimization results with local search of Groups 2 and 3 are shown in Tables 5.18 - 5.20 and 5.21 - 5.25 respectively. Note that the total LU indicated in bold implies an increase due to the local search, while the crack depth indicated in bold or underlined implies a change of first crack nucleation to greater depth or lower depth respectively.

Group 1

Table 5.14

Results from local search with GA of the grinding schedules in Group 1 with 4 grinding steps

Max. Index	Total LU	Crack depth (mm)	Individuals (LU | mm)							
0.99834	**34.1**	8	10.1	5	5.7	5	6.1	5	6.1	5	6.1
0.99550	**34**	23	10.1	5	5.6	5	6.1	5	6.1	5	6.1
0.99918	**34**	13	10.1	5	5.5	5	6.2	5	6.1	5	6.1
0.99956	*33.6*	18	10.1	5	5.7	5	5.3	5	6.5	5	6
0.99550	**34**	**23**	10.1	5	5.6	5	6.1	5	6.1	5	6.1

Table 5.15

Results from local search with GA of the grinding schedules in Group 1 with 5 grinding steps

Max. Index	Total LU	Crack depth (mm)	Individuals (LU | mm)									
0.99921	**35**	**23**	10.1	4	4	4	5.7	4	4.6	4	5.5	4	5.1
0.99834	**35**	**23**	10.1	4	4	4	5.5	4	5	4	5.2	4	5.2
0.99864	**34.9**	23	9.9	4	4.2	4	5.3	4	5.1	4	5.2	4	5.2
0.99928	34.5	23	9.4	4	4.3	4	5.2	4	5.2	4	5.2	4	5.2
0.99921	**34.6**	23	9.6	4	4.2	4	5.2	4	5.2	4	5.2	4	5.2

Table 5.16

Results from local search with GA of the grinding schedules in Group 1 with 10 grinding steps

Max. Index	Total LU	Crack depth (mm)	Individuals (LU | mm)										
0.99945	**35.1**	22	9.8	2	0.3	2	3.8	2	2.1	2	3.3	2	
			2.4	2	1.9	2	2.7	2	3.3	2	2.6	2	2.9
0.99944	**35.1**	**23**	9.2	2	0.9	2	3.6	2	2.4	2	2.6	2	
			3.1	2	0.7	2	5	2	1	2	0.3	2	6.3
0.99857	**34.9**	18	9.7	2	0.4	2	3.8	2	1.2	2	3.3	2	
			2.4	2	2.2	2	3	2	3.3	2	1.7	2	3.9
0.99979	**35**	23	9.3	2	0.6	2	3.6	2	2.7	2	2.4	2	
			3.1	2	0.5	2	5	2	1.4	2	0.1	2	6.3
0.99977	**35.1**	23	9.6	2	0.4	2	3.6	2	2.7	2	2.4	2	
			3.1	2	0.5	2	5	2	1.4	2	0.1	2	6.3

Table 5.17

Results from local search with GA of the grinding schedules in Group 1 with 20 grinding steps

Max. Index	Total LU	Crack depth (mm)	Individuals (LU | mm)									
0.99931	35.3	16	9.1	1	0.5	1	0.5	1	1.4	1	0.6	1	
			2.7	1	0.4	1	1.6	1	1.7	1	1.2	1	
			0.9	1	0.3	1	2.5	1	1.4	1	2	1	
			0.2	1	1.4	1	1.5	1	0.6	1	1.2	1	3.6
0.99917	35	23	6.8	1	1.4	1	0.9	1	2.6	1	0.5	1	
			1.4	1	1.2	1	1.7	1	1.4	1	1.1	1	
			2	1	0.5	1	1.6	1	1.4	1	1.7	1	
			1.4	1	0.4	1	0.3	1	0.6	1	1.4	1	4.7
0.99937	**35.2**	**22**	8.3	1	0.4	1	1.4	1	1.2	1	1.4	1	
			1.4	1	0.6	1	2.4	1	1.4	1	0.7	1	
			2	1	0.3	1	1.2	1	2.4	1	1.4	1	
			0.9	1	1.8	1	0.3	1	2.7	1	0.1	1	2.9
0.99906	**35.2**	**22**	8.2	1	0.4	1	1.3	1	1.4	1	1.4	1	
			1.4	1	0.6	1	2.4	1	1.4	1	0.7	1	
			2.1	1	0.2	1	1.2	1	2.4	1	1.4	1	
			1	1	1.8	1	0.2	1	2.7	1	0.2	1	2.8
0.99997	**35.3**	22	9.1	1	0.5	1	0.6	1	1.4	1	0.6	1	
			2.7	1	0.5	1	1.7	1	1.7	1	1.2	1	
			0.9	1	0.3	1	2.5	1	1.4	1	1.2	1	
			0.2	1	2	1	1.4	1	0.6	1	1.2	1	3.6

Group 2

Table 5.18

Results from local search with GA of the grinding schedules in Group 2 with 4 grinding steps

Max. Index	Total LU	Crack depth (mm)	Individuals (LU | mm)								
0.99940	33.8	13	9.6	5	5.9	5	6.1	5	6.1	5	6.1
0.99940	**33.8**	13	9.6	5	5.9	5	6.1	5	6.1	5	6.1
0.99872	**33.6**	**23**	10.1	5	5.3	4	5.3	6	6.8	5	6.1
0.99956	**33.6**	**18**	10.1	5	5.7	5	5.3	5	6.5	5	6
0.99871	33.1	12	10.1	5	5.3	4	5.3	6	5.9	5	6.5

Table 5.19

Results from local search with GA of the grinding schedules in Group 2 with 5 grinding steps

Max. Index	Total LU	Crack depth (mm)	Individuals (LU | mm)									
0.99835	**34.8**	**23**	9.5	4	4.6	4	5.2	4	5.1	4	5.2	4	5.2
0.99814	**34.6**	**23**	8.9	4	5.1	4	5.1	4	5.1	4	5.2	4	5.2
0.99928	**34.5**	23	9.4	4	4.3	4	5.2	4	5.2	4	5.2	4	5.2
0.99830	**34.6**	**23**	9.4	4	4.7	4	4.8	4	5.3	4	5.2	4	5.2
0.99808	**34.6**	**23**	9.8	5	4.6	3	4.7	4	5.1	4	5.2	4	5.2

Table 5.20

Results from local search with GA of the grinding schedules in Group 2 with 10 grinding steps

Max. Index	Total LU	Crack depth (mm)	Individuals (LU | mm)									
0.99818	**34.9**	22	9.2	2	0.9	1	1.4	2	3	2	2.1	1	
			2.1	2	2.9	3	3	1	1.5	3	4.2	3	4.6
0.99978	**35.2**	**22**	9.1	3	2.7	1	1.3	2	1.2	1	3.8	3	
			3.3	2	2.7	2	2.2	2	1.2	1	3.8	3	3.9
0.99583	**35**	**22**	9.3	2	1.1	2	1.4	1	3.3	2	1.7	1	
			2.1	3	2.9	2	3	1	1.7	3	4.3	3	4.2
0.99979	34.5	19	9.1	3	2.7	2	1.2	1	1.1	1	3.6	3	
			3.3	2	2.7	2	2.2	2	2.1	1	2.7	3	3.8
0.99979	**34.1**	22	5.3	1	3	3	3	1	2.7	2	2.1	3	
			3.9	2	2.6	2	2.7	2	2.7	2	1.7	2	4.4

Group 3

Table 5.21

Results from local search with GA of the grinding schedules in Group 3 with 4 grinding steps

Max. Index	Total LU	Crack depth (mm)	Individuals (LU | mm)								
0.99309	**32.8**	23	10	6	6.7	7	7.2	3	3	4	5.9
0.99876	**33**	23	10.1	5	5.6	7	7.3	4	4.2	4	5.8
0.99786	**32.7**	22	10	5	5.7	7	7.5	5	4.8	3	4.7
0.99995	31.5	23	9.4	7	7.4	2	0.4	5	7.4	6	6.9
0.99922	31.4	22	10.1	6	6.4	6	6.8	6	6.6	2	1.5

Table 5.22

Results from local search with GA of the grinding schedules in Group 3 with 5 grinding steps

Max. Index	Total LU	Crack depth (mm)	Individuals (LU | mm)									
0.99929	34.1	5	8.6	3	3.8	3	4	4	5.5	5	6	5	6.2
0.99967	**34.2**	17	9.9	4	4.2	2	1.4	3	5.5	5	6.2	6	7
0.99967	**34.2**	**17**	9.9	4	4.2	2	1.4	3	5.5	5	6.2	6	7
0.99860	**34**	**23**	8.6	3	3.6	3	4.4	4	5.1	5	6.1	5	6.2
0.99941	**34.1**	23	8.8	3	3.5	3	4	4	5.6	5	6	5	6.2

Table 5.23

Results from local search with GA of the grinding schedules in Group 3 with 8 grinding steps

Max. Index	Total LU	Crack depth (mm)	Individuals (LU | mm)									
0.99817	**34.4**	**22**	5.8	2	5.2	4	5.2	4	4.7	2	0.5	1
			3.1	3	3.4	1	1.8	3	4.7			
0.99983	34	4	1	1	9.2	5	5.7	3	2.5	3	5.1	3
			2.4	1	1.4	1	1.2	3	5.5			
0.99973	**34.1**	23	5.8	2	5.2	4	5.2	4	4.7	2	0.5	1
			3.1	3	3.2	2	1.7	2	4.7			
0.99996	**34.1**	15	1	1	9.2	5	5.7	3	2.5	3	5.1	3
			2.7	1	1.2	1	1.2	3	5.5			
1.00000	**34**	**22**	2.3	1	7.8	3	2.4	3	4.6	2	1.8	2
			2.8	1	1	4	6.3	4	5			

Table 5.24

Results from local search with GA of the grinding schedules in Group 3 with 10 grinding steps

Max. Index	Total LU	Crack depth (mm)	Individuals (LU | mm)										
0.99904	**34.5**	**23**	9.2	2	1.5	3	1.6	1	4.5	3	2.7	1	
			1.6	3	4	2	0.8	1	1.3	1	1.4	3	5.9
0.99920	**34.4**	**14**	8	1	1.1	2	1.9	2	4	3	2.4	1	
			0.7	2	4.9	4	5	2	1.1	2	1.9	1	3.4
0.99930	**34.6**	**23**	8.5	4	4.9	2	0.6	1	1.2	1	1.8	1	
			2.4	2	2.7	2	2.5	3	4.5	3	0.8	1	4.7
0.99988	**34.4**	**22**	10	3	1.5	1	1.1	1	0.1	2	5.7	3	
			1.7	2	3.8	1	0.7	3	5.2	3	2.1	1	2.5
0.99951	**34.5**	23	8.1	1	1.7	2	1.9	3	4.1	2	2.6	1	
			0.8	3	4.9	2	1.6	1	1.4	3	2.1	2	5.3

Table 5.25

Results from local search with GA of the grinding schedules in Group 3 with 15 grinding steps

Max. Index	Total LU	Crack depth (mm)	Individuals (LU | mm)										
0.99888	35.2	16	9.4	1	0.4	1	0.6	1	0.2	2	4.6	2	
			2	1	1	1	0.4	1	3	3	3.6	1	
			1.5	1	0.4	1	0.2	1	2.3	2	1.2	1	4.4
0.99968	**35.4**	16	6.9	1	0.7	1	3.3	2	1.1	1	0.9	1	
			2.7	1	1.4	2	1.6	2	4.3	2	1.2	1	
			2	1	1	1	1.5	1	1.5	1	0.5	2	4.8
0.99686	**35.3**	**22**	8.8	1	0.8	2	2.3	1	0.1	1	2.6	1	
			0.3	1	2.4	1	1.1	2	2.7	1	0.2	1	
			3.1	2	1.5	2	4.2	2	0.9	1	0.7	1	3.6
0.99945	**35.2**	16	6.6	1	0.7	1	3.3	2	1.1	1	1	1	
			2.7	1	1.4	2	1.6	2	4.3	2	1.2	1	
			2	1	1	1	1.5	1	1.6	1	0.3	2	4.9
0.99957	**35.1**	23	9.5	2	0.9	1	0.7	1	0.2	1	3.5	2	
			2.9	1	0.7	1	0.6	1	2.7	3	3.7	1	
			0.9	1	0.5	1	0.3	1	2.3	2	1.3	1	4.4

The optimization with the local search GA is able to increase fatigue life of rail in most cases. The main mechanism of such improvements is by moving first crack nucleation to the regime below the final running surface, says greater than 20 mm. For the grinding schedules in Group 1, the average improvement rates of the loading unit (LU) respected to ones before the local search are 0.89, 0.64, 0.69, and 0.46 % for 4, 5, 10, and 20 grinding steps respectively. For the grinding schedules in Group 2, the average improvement rates of loading unit (LU) are 0.97, 2, and 0.81 % for 4, 5, and 10 grinding steps respectively. For the grinding schedules in Group 3, the average improvement rates of loading unit (LU) are 1.05, 0.77, 0.59, 1.24, and 0.92 % for 4, 5, 8, 10, and 15 grinding steps respectively.

Note that only two grinding schedules in Table 5.14 show improvements of fatigue life while the first crack nucleation moving to lower depth, from 23 to 8 mm and 23 to 13 mm. This is because the limit of the imposed grinding resolution of 1 mm, which is not fine enough. A manual adjustment, not presented here, shows that an increase of final loading unit by 0.05 will increase fatigue life and shift the crack depths to 23 mm for both cases.

Fig. 5.15 is a plot between the increase of fatigue life—compared to one from the no-grinding case (10.16 LU)—and numbers of grinding steps of three groups of grinding schedules. In general, more frequent grinding schedules (15 and 20 grinding steps) tend to give longer fatigue life than that of the less frequents (4, 5, 8, and 10 grinding steps). However, the benefit of increasing grinding steps from 15 to 20 on fatigue life is not

observed as well as that of the 8-grinding-step case, which could be a result of the stochastic approach used in GA.

Comparing between all three groups for 4, 5, and 10 grinding-step cases, Group 1 provides the best grinding schedules for 4, and 5 grinding-steps, while Group 2 provides the best grinding schedule for 10 grinding-steps. In addition to the shorter run-time of the exploratory optimizations in 5.5.5, this again suggests the benefit of using a knowledge-based starting population in an optimization with GA in this study. The benefits of using a stochastic-based starting population, however, should be more apparent when dealing with highly nonlinear fatigue damage distribution, as predicted in the case of more brittle rail steel or a rail steel with discontinuities.

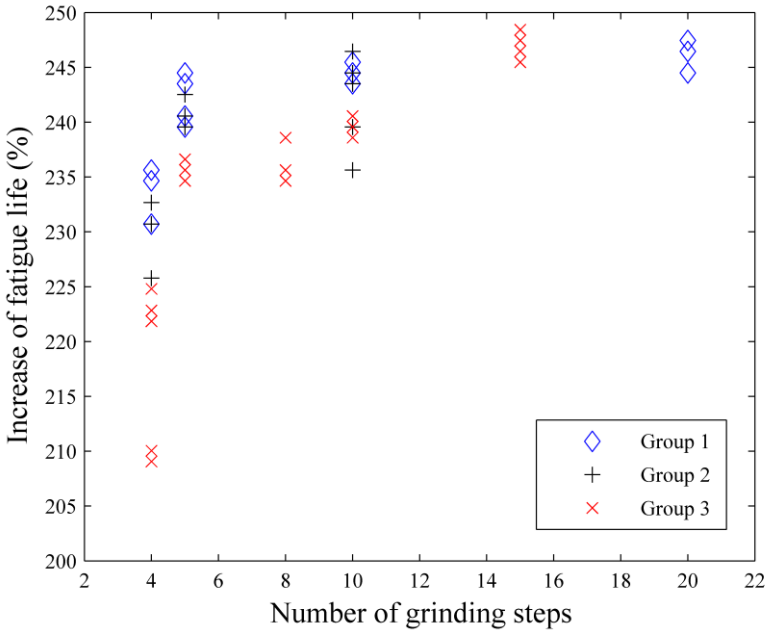

Fig. 5.15. A plot between plot between the predicted loading unit (LU)—normalized by the fatigue life of without-grinding case (10.16 LU), and numbers of grinding steps.

5.6.7 Optimal Grinding Schedules

Fig. 5.16 to 5.21 present schematics of the optimal grinding procedures and their corresponding contours of fatigue index accumulation, right before the nucleation of the first fatigue crack, for different numbers of grinding step. Compared against Fig. 5.11 – 5.14, which are the contours of fatigue index accumulation from the pure deterministic grinding schedules, optimizations with exploratory and local search GAs are able to exercise greater amount of material to near-damage stage. As a result, fatigue life increases from 10.16 LU (no-grinding) and 29.4 - 31.2 LU (deterministically-created grinding schedules) to 34.1 – 35.4 LU when the grinding schedules developed from an optimization with GA are applied. This indicates a 236 – 248 % increase of fatigue life. Nevertheless, the best grinding schedule found in this study (Fig. 5.19(a)) is still unlikely to be the global optima, as the fatigue accumulation contour (Fig. 5.19(b)) seems to deviate from the ideal case, where a continuous contour is expected.

Excluding the case with 8 grinding steps, all grinding plans recommend highly non-uniform grinding patterns for a typical rail steel with $\eta = 1$. Starting with a damage-free rail, the topmost surface of rail is removed after an application of relatively large amount of accumulated axle load, just before those ground-out materials reaching failure. Though grinding helps re-distribute residual stresses in rail head, which will be soon developed again after a few new rolling cycles; the accumulation of fatigue damage at greater depth remains ongoing. As a result, the subsequent grinding steps must be applied at higher frequencies. However, this grinding strategy may or may not be applicable if material behavior changes or discontinuities are taken into consideration.

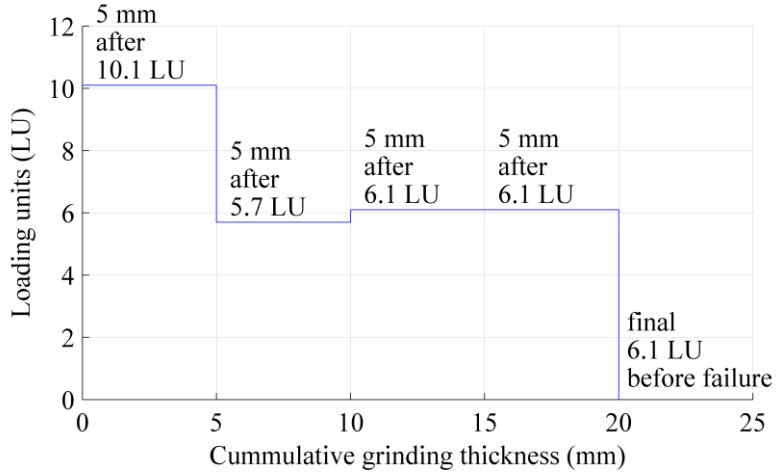

(a)

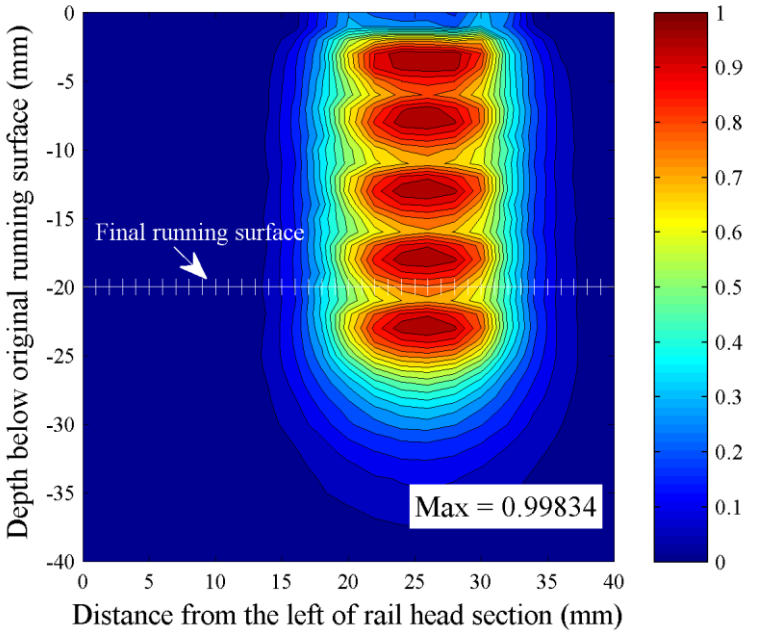

(b)

Fig. 5.16. For the best grinding schedule of 34.1 LU and 0.99834 maximum fatigue index with 4 grinding steps (from Group 1): (a) a schematic of grinding schedule, and (b) a contour of maximum fatigue index accumulation before failure.

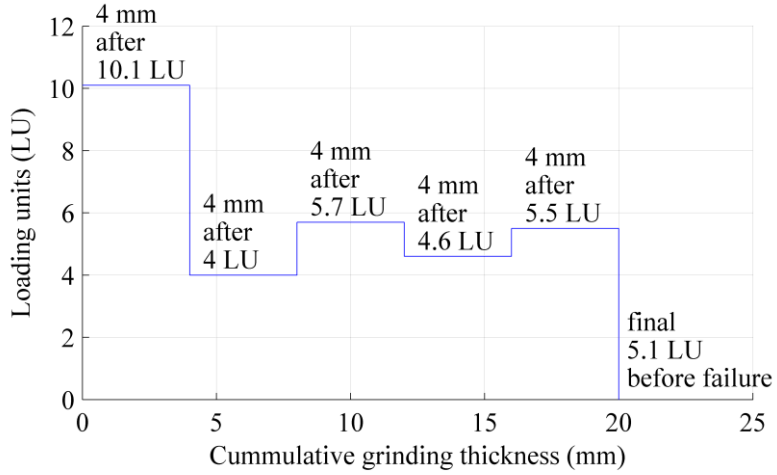

(a)

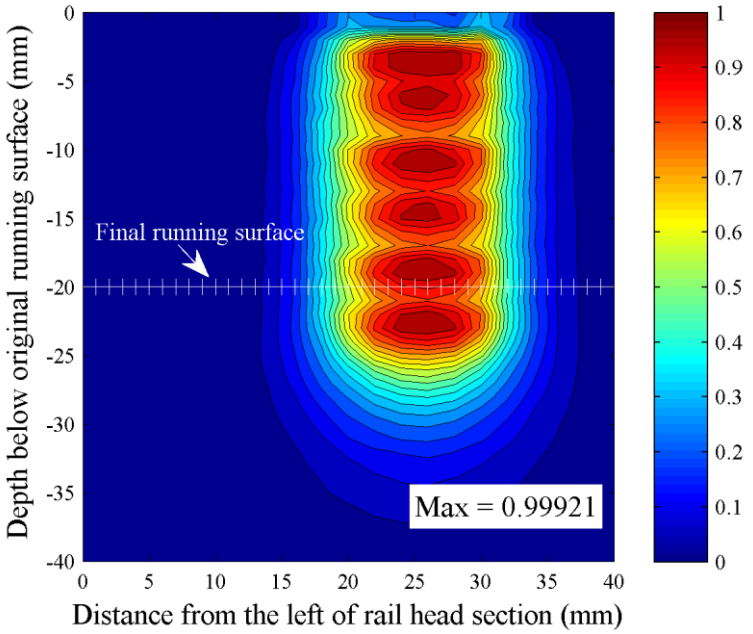

(b)

Fig. 5.17. For the best grinding schedule of 35 LU and 0.99921 maximum fatigue index with 5 grinding steps (from Group 1): (a) a schematic of grinding schedule, and (b) a contour of maximum fatigue index accumulation before failure.

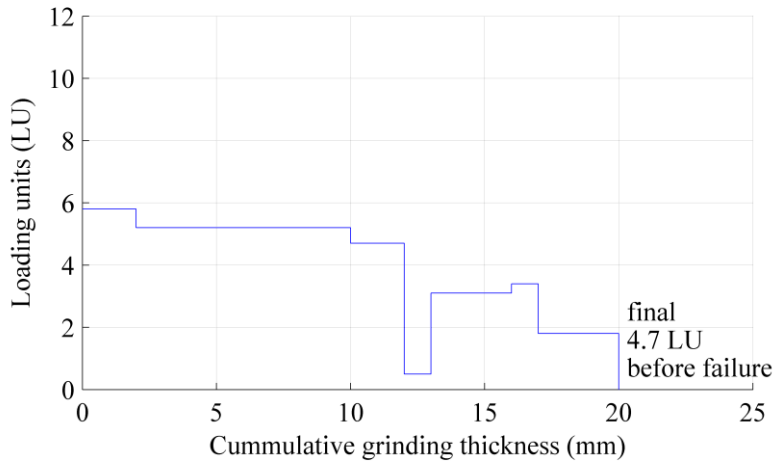

(a)

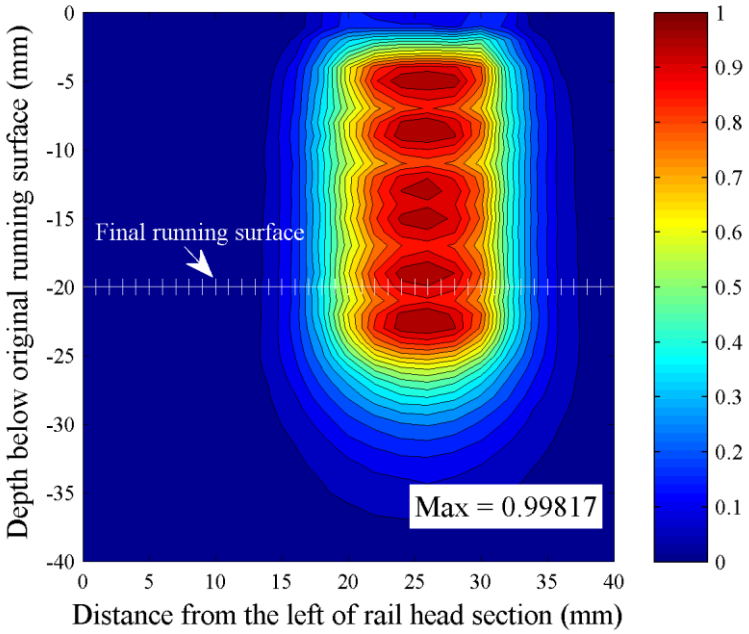

(b)

Fig. 5.18. For the best grinding schedule of 34.4 LU and 0.99817 maximum fatigue index with 8 grinding steps (from Group 3): (a) a schematic of grinding schedule, and (b) a contour of maximum fatigue index accumulation before failure.

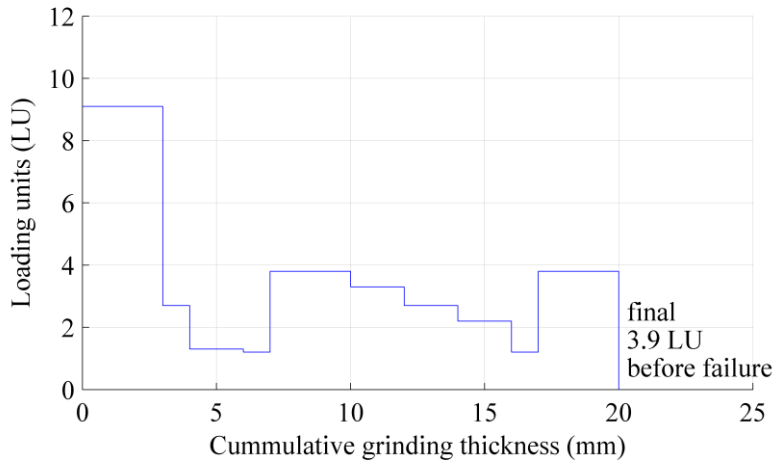

(a)

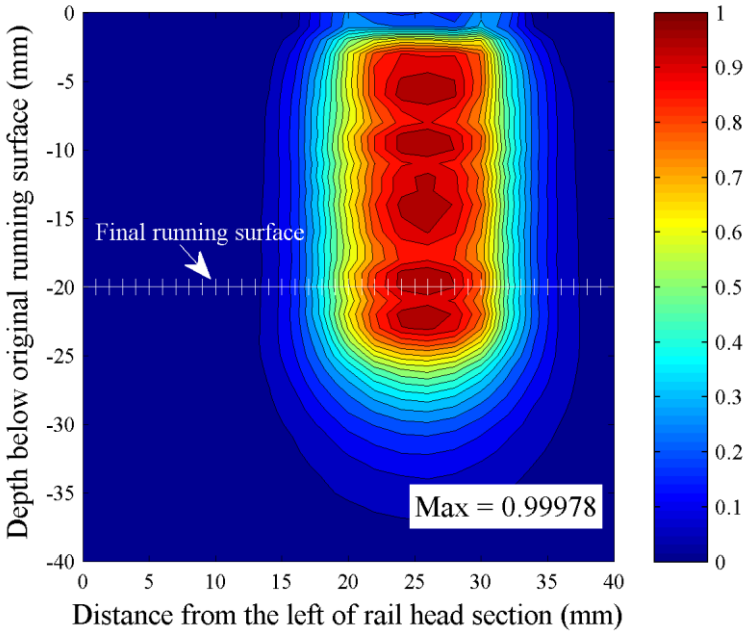

(b)

Fig. 5.19. For the best grinding schedule of 35.2 LU and 0.99978 maximum fatigue index with 10 grinding steps (from Group 2): (a) a schematic of grinding schedule, and (b) a contour of maximum fatigue index accumulation before failure.

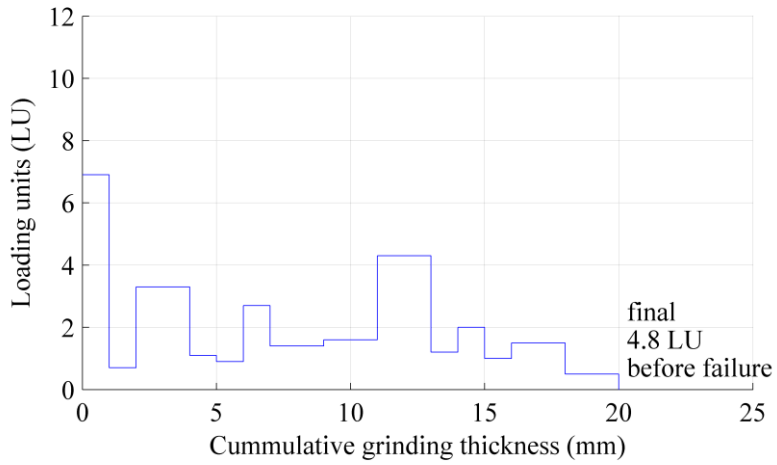

(a)

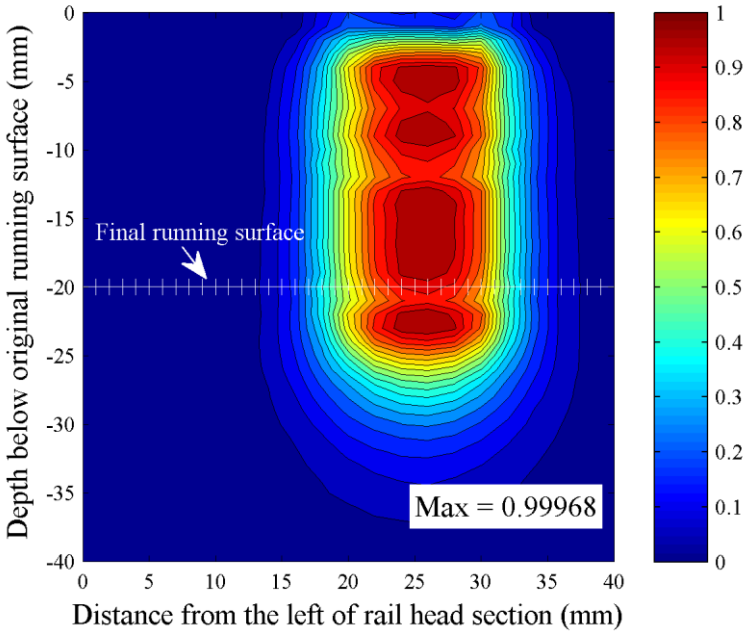

(b)

Fig. 5.20. For the best grinding schedule of 35.4 LU and 0.99968 maximum fatigue index with 15 grinding steps (from group 3): (a) a schematic of grinding schedule, and (b) a contour of maximum fatigue index accumulation before failure.

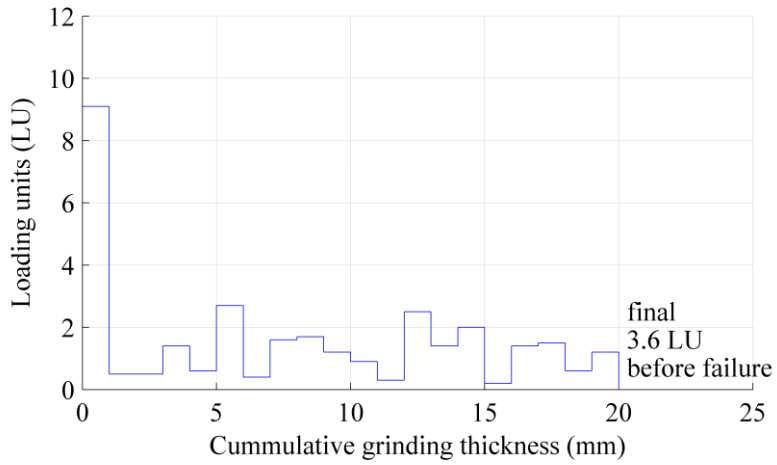

(a)

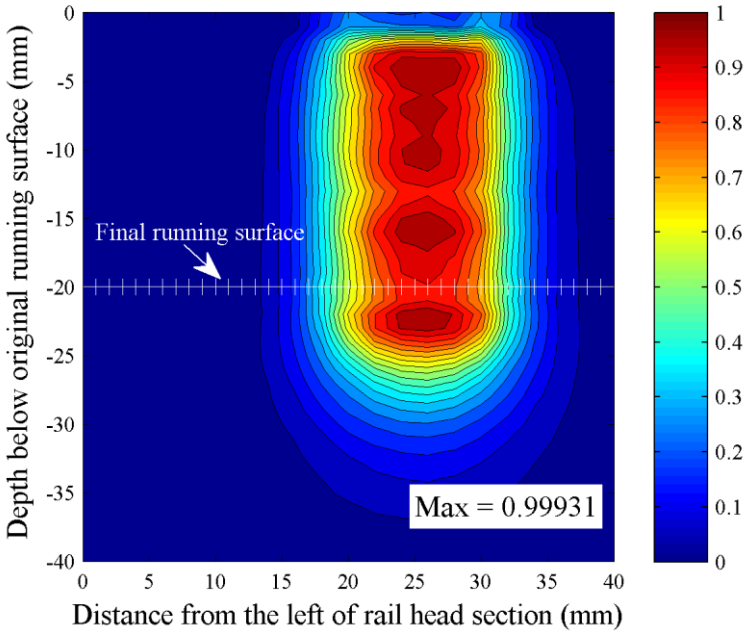

(b)

Fig. 5.21. For the best grinding schedule of 35.3 LU and 0.99931 maximum fatigue index with 20 grinding steps (from group 1): (a) a schematic of grinding schedule, and (b) a contour of maximum fatigue index accumulation before failure.

5.7 Conclusions

- The pure deterministic grinding schedules are able to increase fatigue life of rails about 200%.
- The optimizations with exploratory and local-search genetic algorithm (GA) are able to increase fatigue life of rails about 240%.
- For the current case of study, it is advantageous to use the deterministic (knowledge-based) starting population than the stochastic starting population because: 1) the exploratory optimization with GA runs twice as fast for the same degree of improvement, and 2) it gives rail grinding schedules that provide better fatigue life when local search GA is performed.
- The proposed optimization framework provides a set of rail grinding schedules that improve fatigue life of rail significantly, but they may not be the global optima. Performance of grinding schedule can be qualitatively measured through the continuity of fatigue index contour as proposed in this study.
- Different grinding strategies may be required for the situations different from this study, i.e. two-point wheel-rail contact, or different types of rail steel. With a new database of fatigue index, an updated grinding schedule could be optimized by the proposed optimization framework.
- Fatigue life predictions calculated in this chapter is conservative because the crack propagation period is neglected and the unchanged non-conformal wheel-rail contact is assumed. In actual application, life of crack propagations could be

significant, and wheel profiles tend to increasingly conform to rail profiles, thus decreasing stress localization, as number of rolling passages increases.

CHAPTER VI

CONCLUSIONS AND FUTURE WORK

6.1 Conclusions

- The finite element analysis of wheel-rail rolling contact with the Chaboche plasticity model is able to predict residual stresses and strains in a rail head that agree well with measurements.
- The Findley fatigue criterion, defined in terms of high-cycle fatigue, is able to predict subsurface crack nucleation and early growth – a process influenced strongly by tensile residual stresses. This model is not applicable to model surface cracking behavior, because surface cracking behavior is controlled by plasticity effects.
- The Fatemi-Socie fatigue criterion, which incorporates residual stresses and residual strains into a multi-axial fatigue damage analysis, indicates that the shear strain amplitude component dominates surface crack nucleation and early growth, while both shear strain amplitude and normal stress are found to promote subsurface crack nucleation and early growth.
- Subsurface cracks become an increasingly competitive mode of failure as wheel load and rail material hardness/brittleness increase.
- The deterministic grinding schedules with constantly-fixed loading unit (LU) and grinding thickness could increase fatigue life of rail by 200%.

- Optimization of grinding schedules with exploratory and local-search genetic algorithms indicates increases in rail fatigue life of 240%.
- A set of optimal grinding schedules proposed in this study are yet unlikely to be the global optima. They are subject to further improvement for a continuous contour of fatigue damage accumulation.

6.2 Suggestions for Future Work

More up-to-date fatigue test data of rail steels is needed in order to determine more accurate fatigue-life relationship and more accurate participation of normal stresses in the Fatemi-Socie fatigue criterion. Database of the natural wear from wheel-rail contact should be developed and incorporated into the proposed optimization framework for determining 'true' artificial wear required by rail grinding; this should be done together with a refinement of grinding resolution. A study of correlation between the fatigue life predicted in this study and the actual fatigue life from field tests should be performed; so the grinding schedules developed in this study can be extended to field grinding tests. A reliability study of material imperfections in rail head may be included in rail grinding analysis. The economical aspect of rail grinding may be additionally considered as another objective function, turning the problem into multi-objective optimization.

REFERENCES

[1] Esveld C. Modern railway track. Zaltbommel, The Netherlands: MRT-Productions; 2001.

[2] Rail defect manual. Sperry Rail Service, 1989

[3] Fry GT. A fatigue model for thermite rail welds. Ph.D. Thesis. University of Illinois at Urbana-Champaign; 1995.

[4] Sroba P, Magel E, Prahl F. Getting the most from rail grinding. Railway Track and Structures 2003;99:30-33.

[5] Grassie S, Nilsson P, Bjurstrom K, Frick A, Hansson LG. Alleviation of rolling contact fatigue on Sweden's heavy haul railway. Wear 2002;253:42-53.

[6] Smith R. The wheel-rail interface-some recent accidents. Fatigue Fract Eng Mater Struct 2003;26:901-907.

[7] Kapoor A. A re-evaluation of the life to rupture of ductile metals by cyclic plastic strain. Fatigue Fract Eng Mater Struct 1994;17:201-219.

[8] Cannon D, Edel K, Grassie S, Sawley K. Rail defects: an overview. Fatigue Fract Eng Mater Struct 2003;26:865-886.

[9] Jablonski DA, Pelloux RM. Effect of train load spectra on crack growth in rail steel. In: Orringer O, Orkisz J, Swiderski Z, editors. Residual Stress in Rails: Field experience and test results. Dordrecht, The Netherlands: Kluwer; 1992. p. 81–98.

[10] Tunna J, Sinclair J, Perez J. A review of wheel wear and rolling contact fatigue. IMechE, Part F, J. Rail Rapid Transit 2007;221:271-289.

[11] Ekberg A, Kabo E. Fatigue of railway wheels and rails under rolling contact and thermal loading—an overview. Wear 2005;258:1288-1300.

[12] Fry GT, Lawrence FV, Robinson AR. A model for fatigue defect nucleation in thermite rail welds. Fatigue Fract Eng Mater Struct 1996;19:655-668.

[13] Itoh T, Sakane M, Ohnami M, Socie D. Nonproportional low cycle fatigue criterion for type 304 stainless steel. J Eng Mater Technol, Trans ASME 1995;117:285-292.

[14] Socie DF. Critical plane approaches for multiaxial fatigue damage assessment. In: McDowell DL, Ellis R, editors. Advances in multiaxial fatigue, ASTM STP 1191. Ann Arbor, MI: American Society of Testing and Materials; 1993. p. 7–36.

[15] McDowell D. Stress state dependence of cyclic ratchetting behavior of two rail steels. Int J Plasticity 1995;11:397-421.

[16] Kang G, Gao Q. Uniaxial and non-proportionally multiaxial ratcheting of U71Mn rail steel: experiments and simulations. Mech Mater 2002;34:809-820.

[17] Johnson KL. Contact mechanics. Cambridge: Cambridge Univ Press; 1987.

[18] Sehitoglu H, Jiang Y. Residual stress analysis in rolling contact. In: Kalker JJ, Cannon DF, Orringer O, editors. Rail quality and maintenance for modern railway operation: International Conference on Rail Quality and Maintenance for Modern Railway Operation. Dordrecht, The Netherlands: Kluwer, 1993. p. 349-358.

[19] Jiang Y, Sehitoglu H. Rolling contact stress analysis with the application of a new plasticity model. Wear 1996;191:35-44.

[20] Frederick CO, Armstrong PJ. A mathematical representation of the multiaxial Bauschinger effect. Mater High Temp 2007;24:1-26.

[21] Lemaitre J, Chaboche JL. Mechanics of solid materials. Cambridge: Cambridge Univ Press; 1994.

[22] Chaboche JL. On some modifications of kinematic hardening to improve the description of ratchetting effects. Int J Plasticity 1991;7:661-678.

[23] Steele RK, Joerms MW. Users guide to PHOENIX 7L3: a three dimensional rail fatigue model. Report Number R-728, Association of American Railroads Technical Center, Chicago, IL; 1993.

[24] Bower AF, Cheesewright PR. Measurement of residual shear stresses near the surface of a rail head. Report Number CUED/C-Mech/TR.41, Department of Engineering, University of Cambridge, Cambridge, UK; 1987.

[25] Johansson A, Thorberntsson H. Elastoplastic material model with nonlinear kinematic hardening for rolling and sliding contact fatigue. Technical Report EX 1997:15, Department of Solid Mechanics, Chalmers University of Technology, Gothenburg, Sweden; 1997.

[26] Ekh M, Johansson A, Thorberntsson H, Josefson BL. Models for cyclic ratchetting plasticity - Integration and calibration. J Eng Mater Technol, Trans ASME 2000;122:49-55.

[27] Jiang Y. Three-dimensional elastic-plastic stress analysis of rolling contact. J Tribol, Trans ASME 2002;124:699-708.

[28] Ringsberg J, Bjarnehed H, Johansson A, Josefson B. Rolling contact fatigue of rails - finite element modelling of residual stresses, strains and crack initiation. IMechE, Part F, J. Rail Rapid Transit 2000;214:7-19.

[29] Ringsberg J, Josefson B. Finite element analyses of rolling contact fatigue crack initiation in railheads. IMechE, Part F, J. Rail Rapid Transit 2001;215:243-259.

[30] Jiang Y, Sehitoglu H. Modeling of cyclic ratchetting plasticity, Part I: Development of constitutive relations. J Appl Mech, Trans ASME 1996;63:720-725.

[31] Jiang Y, Sehitoglu H. Modeling of cyclic ratchetting plasticity, Part II: Comparison of model simulations with experiments. J Appl Mech, Trans ASME 1996;63:726-733.

[32] Kulkarni S, Hahn G, Rubin C, V B. Elastoplastic finite-element analysis of repeated 3-dimensional, elliptic rolling-contact with rail wheel properties. J Tribol, Trans ASME 1991;113:434-441.

[33] Bhargava V, Hahn G, Rubin C. Analysis of rolling contact with kinematic hardening for rail steel properties. Wear 1988;122:267-283.

[34] Liu YM, Stratman B, Mahadevan S. Fatigue crack initiation life prediction of railroad wheels. Int J Fatigue 2006;28:747-756.

[35] Telliskivi T, Olofsson U. Contact mechanics analysis of measured wheel-rail profiles using the finite element method. IMechE, Part F, J. Rail Rapid Transit 2001;215:65-72.

[36] Bower AF. Cyclic hardening properties of hard-drawn copper and rail steel. J Mech Phys Solids 1989;37:455-470.

[37] Bower AF, Johnson KL. Shakedown, residual stress and plastic flow in repeated wheel-rail contact. In: Kalker JJ, Cannon DF, Orringer O, editors. Rail quality and maintenance for modern railway operation: International Conference on Rail

Quality and Maintenance for Modern Railway Operation. Dordrecht, The Netherlands: Kluwer, 1992. p. 239-252.

[38] Khan A, Huang S. Continuum theory of plasticity. New York, NY: Wiley-Interscience; 1995.

[39] Chaboche J. A review of some plasticity and viscoplasticity constitutive theories. Int J Plasticity 2008;24:1642-1693.

[40] Jiang Y, Kurath P. Characteristics of the Armstrong-Frederick type plasticity models. Int J Plasticity 1996;12:387-416.

[41] Ohno N. Recent topics in constitutive modeling of cyclic plasticity and viscoplasticity. Appl Mech Rev 1990;43:283–295.

[42] Bari S, Hassan T. Anatomy of coupled constitutive models for ratcheting simulation. Int J Plasticity 2000;16:381-409.

[43] Ohno N. Constitutive modeling of cyclic plasticity with emphasis on ratchetting. Int J Mech Sci 1998;40:251-261.

[44] Bari S, Hassan T. An advancement in cyclic plasticity modeling for multiaxial ratcheting simulation. Int J Plasticity 2002;18:873-894.

[45] ABAQUS 6.7 user's manual. ABAQUS, Inc, 2007

[46] Shima M, Okada K, Kimura Y, Yamamoto T. Measurements of subsurface plastic flow in rolling contact. J JSLE Int Edn 1981;2:75–80.

[47] Hamilton GM. Plastic flow in rollers loaded above the yield point. Proc Inst Mech Eng 1963;177:667-675.

[48] Bannantine J, Comer J, Handrock J. Fundamentals of metal fatigue analysis. Upper Saddle River, NJ: Prentice Hall; 1990.

[49] Garud YS. Multiaxial fatigue- A survey of the state of the art. J Test Eval 1981;9:165-178.

[50] Socie DF, Marquis GB. Multiaxial fatigue. Warrendale, PA: Society of Automotive Engineers; 2000.

[51] Meggiolaro M, de Castro J, de Oliveira Miranda A. Evaluation of multiaxial stress-strain models and fatigue life prediction methods under proportional loading. In: da Costa Mattos HS, Alves M, editors. Mechanics of Solids in Brazil 2009. Rio de Janeiro, Brazil: Brazilian Society of Mechanical Sciences and Engineering; 2009. p. 365-384.

[52] Balthazar J, Malcher L. A review on the main approaches for determination of the multiaxial high cycle fatigue strength. In: Alves M, da Costa Mattos HS, editors. Mechanics of solids in Brazil 2007. Rio de Janeiro, Brazil: Brazilian Society of Mechanical Sciences and Engineering; 2007. p. 63-80.

[53] Karolczuk A, Macha E. A review of critical plane orientations in multiaxial fatigue failure criteria of metallic materials. Int J Fracture 2005;134:267-304.

[54] Jiang Y, Hertel O, Vormwald M. An experimental evaluation of three critical plane multiaxial fatigue criteria. Int J Fatigue 2007;29:1490-1502.

[55] Findley WN. A theory for the effect of mean stress on fatigue of metals under combined torsion and axial load or bending. J Engng Industry, Trans ASME 1959;81:301-306.

[56] Kaufman RP, Topper T. The influence of static mean stresses applied normal to the maximum shear planes in multiaxial fatigue. In: Carpinteri A, de Freitas M, Spagnoli A, editors. Biaxial/Multiaxial Fatigue and Fracture. Parma, Italy: Elsevier and ESIS; 2003. p. 123-143.

[57] Hayhurst DR, Leckie FA, McDowell DL. Damage growth under nonproportional loading. ASTM STP 1985;853:688-699.

[58] Mcdowell DL, Stahl DR, Stock SR, Antolovich SD. Biaxial path dependence of deformation substructure of type-304 stainless-steel. Metall trans A – Phys Metall Mater Sci 1988;19:1277-1293.

[59] Alfredsson B, Olsson M. Applying multiaxial fatigue criteria to standing contact fatigue. Int J Fatigue 2001;23:533-548.

[60] Scutti JJ, Pelloux RM, Fuquen-Moleno R. Fatigue behavior of a rail steel. Fatigue Fract Eng Mater Struct 2007;7:121-135.

[61] Iwafuchi K, Satoh Y, Toi Y, Hirose S. Fatigue property analysis of rail steel based on damage mechanics. Quarterly Report of RTRI 2004;45:203-209.

[62] Ahlström J, Karlsson B. Fatigue behaviour of rail steel--a comparison between strain and stress controlled loading. Wear 2005;258:1187-1193.

[63] Fry GT. Fatigue bending tests of rail steels (Internal communication); 2008.

[64] Stadlbauer W, Werner E. Zyklisch-plastisches Verhalten von un- und niedriglegierten Kohlenstoffstählen (in German). BHM Berg- und Hüttenmännische Monatshefte 1999;144:356-361.

[65] Park J, Nelson D. Evaluation of an energy-based approach and a critical plane approach for predicting constant amplitude multiaxial fatigue life. Int J Fatigue 2000;22:23-39.

[66] Fatemi A, Socie DF. A critical plane approach to multiaxial fatigue damage including out-of-phase loading. Fatigue Fract Eng Mater Struct 1988;11:149-165.

[67] Stephens RI, Fuchs HO, Fatemi A, Stephens RR. Metal fatigue in engineering, 2nd ed. New York, NY: Wiley-Interscience; 2000.

[68] Brown MW, Miller KJ. A theory for fatigue failure under multiaxial stress-strain conditions. Proc Inst Mech Engrs 1973;187:745-755.

[69] Fatemi A, Kurath P. Multiaxial fatigue life predictions under the influence of mean-stresses. J Eng Mater Technol, Trans ASME 1988;110:380-388.

[70] Smith KN, Topper TH, Watson P. A stress-strain function for the fatigue of metals. J Mater, JMLSA 1970;5(4):767-778.

[71] Eshelby JD. The determination of the elastic field of an ellipsoidal inclusion, and related problems. Proc R Soc Lond A 1957;241:376-396.

[72] Kalker JJ. Wheel-rail rolling contact theory. Wear 1991;144:243-261.

[73] Iwnicki S. Handbook of railway vehicle dynamics. Boca Raton, FL: Taylor & Francis; 2006.

[74] Clayton P, Hill DN. Rolling contact fatigue of a rail steel. Wear 1987;117:319-334.

[75] Vasic G, Franklin FJ, Fletcher DI, Kapoor A. Effect of traffic on crack initiation in rails. Journal of Mechanical Systems for Transportation and Logistics 2010;3:100-109.

[76] Olver AV. The mechanism of rolling contact fatigue: an update. Proc Inst Mech Eng Part J 2005;219:313-330.

[77] Frohling RD. Wheel/rail interface management in heavy haul railway operations - applying science and technology. Vehicle System Dynamics 2007;45:649-677.

[78] Grassie SL. Rolling contact fatigue on the British railway system: treatment. Wear 2005;258:1310-1318.

[79] Magel E, Roney M, Kalousek J, Sroba P. The blending of theory and practice in modern rail grinding. Fatigue Fract Eng Mater Struct 2003;26:921-929.

[80] Satoh Y, Iwafuchi K. Effect of rail grinding on rolling contact fatigue in railway rail used in conventional line in Japan. Wear 2008;265:1342-1348.

[81] Jones SL. An analytical study of rail grinding optimization for rail-head fatigue defect prevention. MS. Thesis. Texas A&M University; 1997.

[82] Kapoor A, Franklin FJ. Tribological layers and the wear of ductile materials. Wear 2000;245:204-215.

[83] Ishida M, Akama M, Kashiwaya K, Kapoor A. The current status of theory and practice on rail integrity in Japanese railways - rolling contact fatigue and corrugations. Fatigue Fract Eng Mater Struct 2003;26:909-919.

[84] Aarts E, Lenstra JK. Local search in combinatorial optimization. Princeton, NJ: Princeton Univ Press; 2003.

[85] Eiben A, Smith J. Introduction to evolutionary computing. Heidelberg: Springer Verlag; 2003.

[86] Mitchell M. An introduction to genetic algorithms. Cambridge, MA: The MIT press; 1998.

[87] Eiben AE, Hinterding R, Michalewicz Z. Parameter control in evolutionary algorithms. IEEE Trans. Evolutionary Comput 1999;3(2):124-141.

[88] Reed P, Minsker B, Goldberg DE. Designing a competent simple genetic algorithm for search and optimization. Water Resour Res 2000;36:3757-3761.

[89] Eiben AE, Schippers CA. On evolutionary exploration and exploitation. Fund Inform 1998;35:35-50.

[90] Persson I, Iwnicki SD. Optimization of railway wheel profiles using a genetic algorithm. Vehicle Syst Dyn 2004;41:517-526.

[91] Saravanan R, Asokan P, Sachidanandam M. A multi-objective genetic algorithm (GA) approach for optimization of surface grinding operations. Int J Machine Tools Manuf 2002;42:1327-1334.

[92] Asokan P, Baskar N, Babu K, Prabhaharan G, Saravanan R. Optimization of surface grinding operations using particle swarm optimization technique. Journal of manufacturing science and engineering 2005;127:885-892.

[93] Joy RB, Oliva DC, Otter DE, Doe BE, Uppal SA. FAST bridge tests. Association of American Railroads, Report number R-948, Transportation Technology Center, Inc, Pueblo, CO; 2001.

[94] M. Igor, Elliptic integrals and Jacobi's zeta function. <http://www.mathworks.com/matlabcentral/fileexchange/7123-elliptic-integrals-and-jacobis-zeta-function>. (accessed on 5/12/09)

APPENDIX A

FATIGUE DAMAGE IN A RAIL HEAD WITH SPHERICAL PORES

Using Findley fatigue criterion and Fatemi-Socie fatigue criterion , Fig. A.1 – A.4 are fatigue index contours when spherical pores are presented throughout the rail cross-section located between 12 to 40 mm below running surface. The calculations of rolling stresses due to spherical pores are given in Eshelby [71]. A Matlab code for the *elliptic integral* is created by Igor [90].

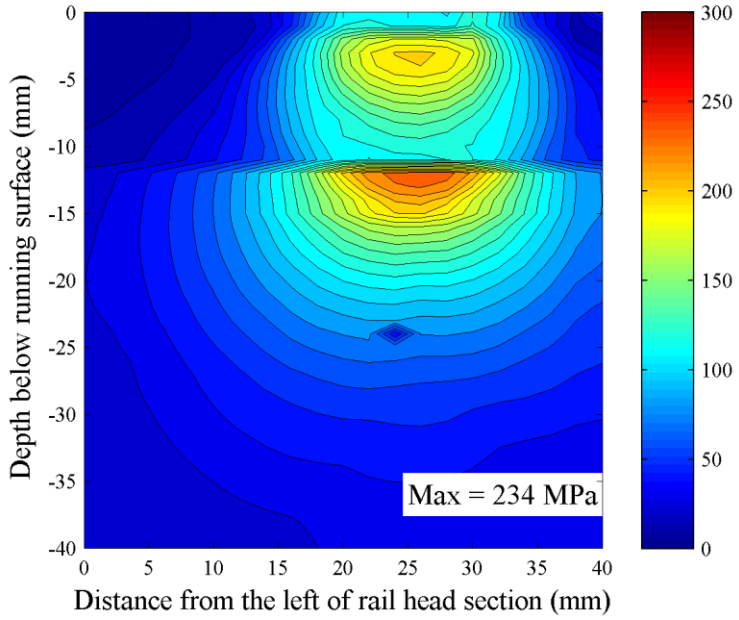

Fig. A.1. A maximum Findley fatigue index contour (κ = 0.3) of the 162 kN wheel load at the sixth loading cycle with spherical pores from 12-40 mm below running surface.

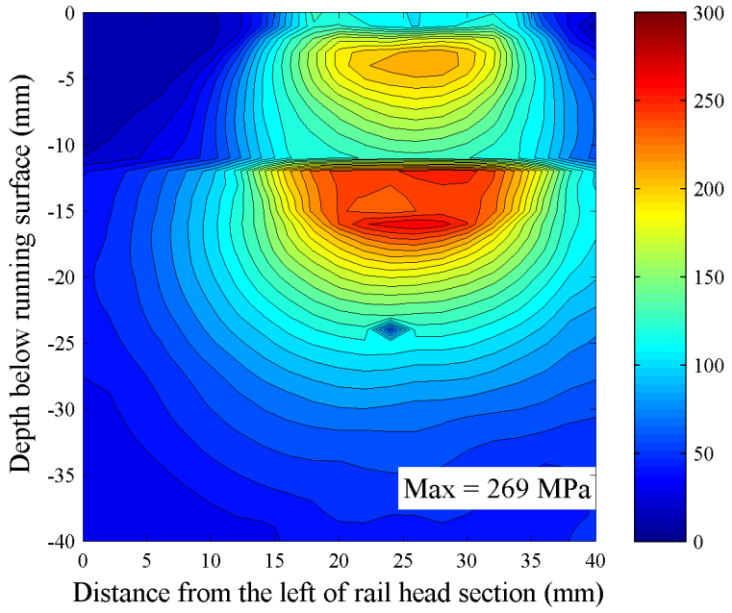

Fig. A.2. A maximum Findley fatigue index contour (κ = 0.3) of the 233 kN wheel load at the sixth loading cycle with spherical pores from 12-40 mm below running surface.

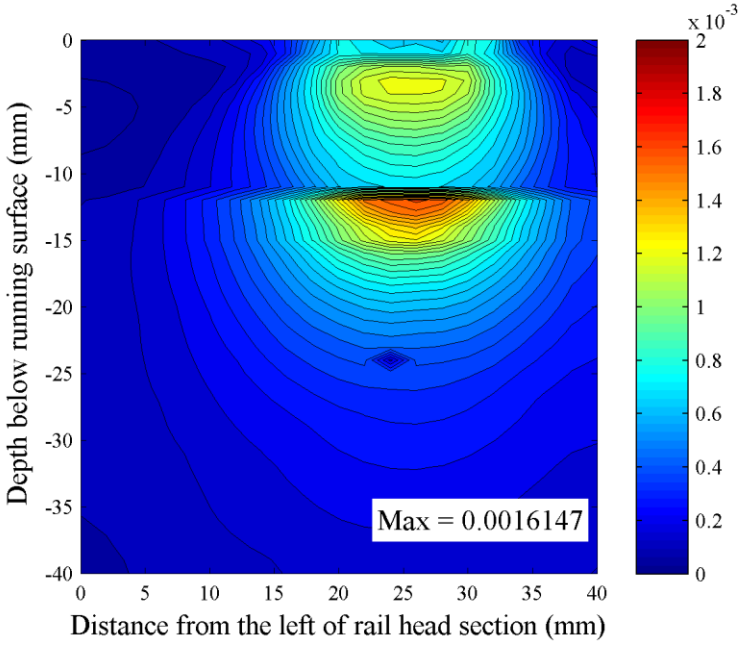

Fig. A.3. A maximum Fatemi-Socie fatigue index contour (η = 1) of the 162 kN wheel load at the sixth loading cycle with spherical pores from 12-40 mm below running surface.

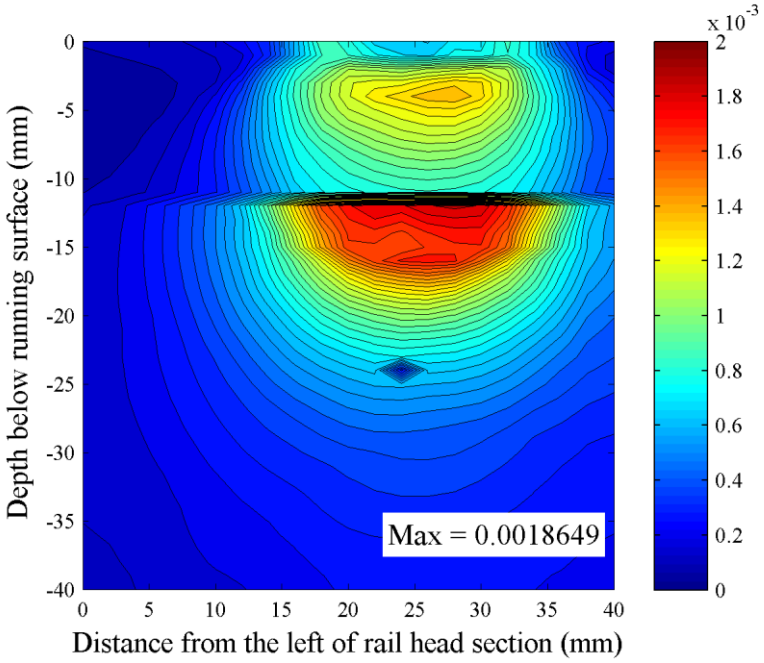

Fig. A.4. A maximum Fatemi-Socie fatigue index contour (η = 1) of the 233 kN wheel load at the sixth loading cycle with spherical pores from 12-40 mm below running surface.

APPENDIX B

STARTING POPULATIONS FOR OPTIMIZATION WITH GENETIC ALGORITHM

Table A.1

A set of starting individuals from a deterministic approach for grinding schedules with 4 steps

Max. Damage	Total LU	Crack depth (mm)	Individuals (LU | mm)								
0.40658	12.5	23	2.5	5	2.5	5	2.5	5	2.5	5	2.5
0.42284	13	23	2.6	5	2.6	5	2.6	5	2.6	5	2.6
0.43911	13.5	23	2.7	5	2.7	5	2.7	5	2.7	5	2.7
0.52042	16	23	3.2	5	3.2	5	3.2	5	3.2	5	3.2
0.53669	16.5	23	3.3	5	3.3	5	3.3	5	3.3	5	3.3
0.55295	17	23	3.4	5	3.4	5	3.4	5	3.4	5	3.4
0.56921	17.5	23	3.5	5	3.5	5	3.5	5	3.5	5	3.5
0.66679	20.5	23	4.1	5	4.1	5	4.1	5	4.1	5	4.1
0.68306	21	23	4.2	5	4.2	5	4.2	5	4.2	5	4.2
0.71558	22	23	4.4	5	4.4	5	4.4	5	4.4	5	4.4
0.73185	22.5	23	4.5	5	4.5	5	4.5	5	4.5	5	4.5
0.74811	23	23	4.6	5	4.6	5	4.6	5	4.6	5	4.6
0.76437	23.5	23	4.7	5	4.7	5	4.7	5	4.7	5	4.7
0.78064	24	23	4.8	5	4.8	5	4.8	5	4.8	5	4.8
0.79690	24.5	23	4.9	5	4.9	5	4.9	5	4.9	5	4.9
0.86195	26.5	23	5.3	5	5.3	5	5.3	5	5.3	5	5.3
0.87822	27	23	5.4	5	5.4	5	5.4	5	5.4	5	5.4
0.95953	29.5	23	5.9	5	5.9	5	5.9	5	5.9	5	5.9
0.97580	30	23	6	5	6	5	6	5	6	5	6
0.99206	30.5	23	6.1	5	6.1	5	6.1	5	6.1	5	6.1

Table A.2

A set of starting individuals from a deterministic approach for grinding schedules with 5 steps

Max. Damage	Total LU	Crack depth (mm)	Individuals (LU | mm)										
0.38325	12	23	2	4	2	4	2	4	2	4	2	4	2
0.40241	12.6	23	2.1	4	2.1	4	2.1	4	2.1	4	2.1	4	2.1
0.47906	15	23	2.5	4	2.5	4	2.5	4	2.5	4	2.5	4	2.5
0.55571	17.4	23	2.9	4	2.9	4	2.9	4	2.9	4	2.9	4	2.9
0.57487	18	23	3	4	3	4	3	4	3	4	3	4	3
0.59403	18.6	23	3.1	4	3.1	4	3.1	4	3.1	4	3.1	4	3.1
0.61320	19.2	23	3.2	4	3.2	4	3.2	4	3.2	4	3.2	4	3.2
0.63236	19.8	23	3.3	4	3.3	4	3.3	4	3.3	4	3.3	4	3.3
0.65152	20.4	23	3.4	4	3.4	4	3.4	4	3.4	4	3.4	4	3.4
0.72817	22.8	23	3.8	4	3.8	4	3.8	4	3.8	4	3.8	4	3.8
0.74733	23.4	23	3.9	4	3.9	4	3.9	4	3.9	4	3.9	4	3.9
0.78566	24.6	23	4.1	4	4.1	4	4.1	4	4.1	4	4.1	4	4.1
0.86231	27	23	4.5	4	4.5	4	4.5	4	4.5	4	4.5	4	4.5
0.88147	27.6	23	4.6	4	4.6	4	4.6	4	4.6	4	4.6	4	4.6
0.90063	28.2	23	4.7	4	4.7	4	4.7	4	4.7	4	4.7	4	4.7
0.91980	28.8	23	4.8	4	4.8	4	4.8	4	4.8	4	4.8	4	4.8
0.93896	29.4	23	4.9	4	4.9	4	4.9	4	4.9	4	4.9	4	4.9
0.95812	30	23	5	4	5	4	5	4	5	4	5	4	5
0.97728	30.6	23	5.1	4	5.1	4	5.1	4	5.1	4	5.1	4	5.1
0.99644	31.2	23	5.2	4	5.2	4	5.2	4	5.2	4	5.2	4	5.2

Table A.3

A set of starting individuals from a deterministic approach for grinding schedules with 10 steps

Max. Damage	Total LU	Crack depth (mm)	Individuals (LU | mm)										
0.35846	11	20	1	2	1	2	1	2	1	2	1	2	
			1	2	1	2	1	2	1	2	1	2	1
0.39430	12.1	20	1.1	2	1.1	2	1.1	2	1.1	2	1.1	2	
			1.1	2	1.1	2	1.1	2	1.1	2	1.1	2	1.1
0.43015	13.2	20	1.2	2	1.2	2	1.2	2	1.2	2	1.2	2	
			1.2	2	1.2	2	1.2	2	1.2	2	1.2	2	1.2
0.46599	14.3	20	1.3	2	1.3	2	1.3	2	1.3	2	1.3	2	
			1.3	2	1.3	2	1.3	2	1.3	2	1.3	2	1.3
0.50184	15.4	20	1.4	2	1.4	2	1.4	2	1.4	2	1.4	2	
			1.4	2	1.4	2	1.4	2	1.4	2	1.4	2	1.4
0.53768	16.5	20	1.5	2	1.5	2	1.5	2	1.5	2	1.5	2	
			1.5	2	1.5	2	1.5	2	1.5	2	1.5	2	1.5
0.57353	17.6	20	1.6	2	1.6	2	1.6	2	1.6	2	1.6	2	
			1.6	2	1.6	2	1.6	2	1.6	2	1.6	2	1.6
0.60938	18.7	20	1.7	2	1.7	2	1.7	2	1.7	2	1.7	2	
			1.7	2	1.7	2	1.7	2	1.7	2	1.7	2	1.7
0.64522	19.8	20	1.8	2	1.8	2	1.8	2	1.8	2	1.8	2	
			1.8	2	1.8	2	1.8	2	1.8	2	1.8	2	1.8
0.68107	20.9	20	1.9	2	1.9	2	1.9	2	1.9	2	1.9	2	
			1.9	2	1.9	2	1.9	2	1.9	2	1.9	2	1.9
0.71691	22	20	2	2	2	2	2	2	2	2	2	2	
			2	2	2	2	2	2	2	2	2	2	2
0.75276	23.1	20	2.1	2	2.1	2	2.1	2	2.1	2	2.1	2	
			2.1	2	2.1	2	2.1	2	2.1	2	2.1	2	2.1
0.78860	24.2	20	2.2	2	2.2	2	2.2	2	2.2	2	2.2	2	
			2.2	2	2.2	2	2.2	2	2.2	2	2.2	2	2.2
0.82445	25.3	20	2.3	2	2.3	2	2.3	2	2.3	2	2.3	2	
			2.3	2	2.3	2	2.3	2	2.3	2	2.3	2	2.3
0.86029	26.4	20	2.4	2	2.4	2	2.4	2	2.4	2	2.4	2	
			2.4	2	2.4	2	2.4	2	2.4	2	2.4	2	2.4
0.89614	27.5	20	2.5	2	2.5	2	2.5	2	2.5	2	2.5	2	
			2.5	2	2.5	2	2.5	2	2.5	2	2.5	2	2.5
0.93199	28.6	20	2.6	2	2.6	2	2.6	2	2.6	2	2.6	2	
			2.6	2	2.6	2	2.6	2	2.6	2	2.6	2	2.6
0.96783	29.7	20	2.7	2	2.7	2	2.7	2	2.7	2	2.7	2	
			2.7	2	2.7	2	2.7	2	2.7	2	2.7	2	2.7
0.67797	18.9	20	1.7	2	1.7	2	1.7	2	1.7	2	1.7	2	
			1.6	2	0.9	2	1.7	2	2.8	2	1.7	2	1.7
0.59185	16.1	22	1.5	2	0.5	2	1.5	2	1.5	2	1.5	2	
			1.5	2	1.5	2	1.5	2	1.5	2	2.1	2	1.5

Table A.4

A set of starting individuals from a deterministic approach for grinding schedules with 20 steps

Max. Damage	Total LU	Crack depth (mm)	Individuals (LU | mm)										
0.98837	29.4	20	1.4	1	1.4	1	1.4	1	1.4	1	1.4	1	
			1.4	1	1.4	1	1.4	1	1.4	1	1.4	1	
			1.4	1	1.4	1	1.4	1	1.4	1	1.4	1	
			1.4	1	1.4	1	1.4	1	1.4	1	1.4	1	1.4
0.35299	10.5	20	0.5	1	0.5	1	0.5	1	0.5	1	0.5	1	
			0.5	1	0.5	1	0.5	1	0.5	1	0.5	1	
			0.5	1	0.5	1	0.5	1	0.5	1	0.5	1	
			0.5	1	0.5	1	0.5	1	0.5	1	0.5	1	0.5
0.42359	12.6	20	0.6	1	0.6	1	0.6	1	0.6	1	0.6	1	
			0.6	1	0.6	1	0.6	1	0.6	1	0.6	1	
			0.6	1	0.6	1	0.6	1	0.6	1	0.6	1	
			0.6	1	0.6	1	0.6	1	0.6	1	0.6	1	0.6
0.49419	14.7	20	0.7	1	0.7	1	0.7	1	0.7	1	0.7	1	
			0.7	1	0.7	1	0.7	1	0.7	1	0.7	1	
			0.7	1	0.7	1	0.7	1	0.7	1	0.7	1	
			0.7	1	0.7	1	0.7	1	0.7	1	0.7	1	0.7
0.56478	16.8	20	0.8	1	0.8	1	0.8	1	0.8	1	0.8	1	
			0.8	1	0.8	1	0.8	1	0.8	1	0.8	1	
			0.8	1	0.8	1	0.8	1	0.8	1	0.8	1	
			0.8	1	0.8	1	0.8	1	0.8	1	0.8	1	0.8
0.63538	18.9	20	0.9	1	0.9	1	0.9	1	0.9	1	0.9	1	
			0.9	1	0.9	1	0.9	1	0.9	1	0.9	1	
			0.9	1	0.9	1	0.9	1	0.9	1	0.9	1	
			0.9	1	0.9	1	0.9	1	0.9	1	0.9	1	0.9
0.70598	21	20	1	1	1	1	1	1	1	1	1	1	
			1	1	1	1	1	1	1	1	1	1	
			1	1	1	1	1	1	1	1	1	1	
			1	1	1	1	1	1	1	1	1	1	1
0.77658	23.1	20	1.1	1	1.1	1	1.1	1	1.1	1	1.1	1	
			1.1	1	1.1	1	1.1	1	1.1	1	1.1	1	
			1.1	1	1.1	1	1.1	1	1.1	1	1.1	1	
			1.1	1	1.1	1	1.1	1	1.1	1	1.1	1	1.1
0.84718	25.2	20	1.2	1	1.2	1	1.2	1	1.2	1	1.2	1	
			1.2	1	1.2	1	1.2	1	1.2	1	1.2	1	
			1.2	1	1.2	1	1.2	1	1.2	1	1.2	1	
			1.2	1	1.2	1	1.2	1	1.2	1	1.2	1	1.2
0.97359	27.9	20	1.3	1	1.3	1	1.3	1	1.3	1	1.3	1	
			1.3	1	1.3	1	1.3	1	1.3	1	1.3	1	
			1.3	1	1.3	1	1.3	1	1.3	1	1.3	1	
			1.5	1	1.3	1	1.7	1	1.3	1	1.3	1	1.3

Table A.4

Continued

Max. Damage	Total LU	Crack depth (mm)	Individuals (LU | mm)										
0.77709	22.8	20	1.1	1	1.1	1	1.1	1	1.1	1	1.1	1	
			1.1	1	1.1	1	1.1	1	1.1	1	0.6	1	
			1.1	1	1.1	1	1.1	1	1.3	1	1.1	1	
			1.1	1	1.1	1	1.1	1	1.1	1	1.1	1	1.1
0.99727	31.1	20	1.4	1	3.3	1	0.8	1	1.4	1	1.4	1	
			1.4	1	1.4	1	2	1	1.4	1	1.2	1	
			1.4	1	1.4	1	1.4	1	1.4	1	1.4	1	
			1.4	1	1.4	1	1.4	1	1.4	1	1.4	1	1.4
0.98144	28.4	21	1.4	1	1.4	1	0.6	1	1.4	1	1.4	1	
			1.4	1	1.4	1	1.4	1	1.4	1	1.2	1	
			1.4	1	1.4	1	1.4	1	1.4	1	1.4	1	
			1.4	1	1.4	1	1.4	1	1.4	1	1.4	1	1.4
0.91777	27.3	20	1.3	1	1.3	1	1.3	1	1.3	1	1.3	1	
			1.3	1	1.3	1	1.3	1	1.3	1	1.3	1	
			1.3	1	1.3	1	1.3	1	1.3	1	1.3	1	
			1.3	1	1.3	1	1.3	1	1.3	1	1.3	1	1.3
0.86730	26.3	15	1.3	1	1.3	1	1.3	1	1.3	1	1.2	1	
			1.3	1	1.3	1	1.3	1	1.3	1	1.3	1	
			1.3	1	1.3	1	1.3	1	1.3	1	0.4	1	
			1.3	1	1.3	1	1.3	1	1.3	1	1.3	1	1.3
0.99866	31.1	20	1.4	1	3.3	1	0.8	1	1.4	1	1.4	1	
			1.4	1	1.4	1	2	1	1.4	1	1.2	1	
			1.2	1	1.6	1	1.4	1	1.4	1	1.4	1	
			1.4	1	1.4	1	1.4	1	1.4	1	1.4	1	1.4
0.70598	21	20	1	1	1	1	1	1	1	1	1	1	
			1	1	1	1	1	1	1	1	1	1	
			1	1	1	1	1	1	1	1	1	1	
			1	1	1	1	1	1	1	1	1	1	1
0.70129	20	20	1	1	1	1	1	1	0.4	1	1	1	
			1	1	1	1	1	1	1	1	1	1	
			1	1	1	1	1	1	1	1	1	1	
			1	1	1	1	1	1	1	1	1	1	0.6
0.56656	16.6	20	0.8	1	0.8	1	0.4	1	0.8	1	0.8	1	
			0.8	1	0.8	1	0.8	1	1	1	0.8	1	
			0.8	1	0.8	1	0.8	1	0.8	1	0.8	1	
			0.8	1	0.8	1	0.8	1	0.8	1	0.8	1	0.8
0.68287	19.7	20	1	1	1	1	1	1	0.4	1	1	1	
			1	1	1	1	1	1	1	1	1	1	
			1	1	1	1	1	1	0.8	1	1	1	
			1	1	1	1	1	1	0.9	1	1	1	0.6

Table A.5

A set of starting individuals from a stochastic approach for grinding schedules with 4 steps

Max. Damage	Total LU	Crack depth (mm)	Individuals (LU | mm)								
0.82467	13.4	16	1.7	5	1.2	7	7.3	2	1.1	6	2.1
0.98617	21.5	9	1.8	5	8.3	2	1.7	7	2.3	6	7.4
0.86695	17.5	15	2.6	6	1.9	6	7.9	6	1.6	2	3.5
0.43043	11.6	23	2.1	1	1.7	6	1.9	7	2.6	6	3.3
0.66793	10.6	6	1.6	1	2.2	2	3.8	16	1.3	1	1.7
0.57212	13.9	10	3	2	2.1	5	4.1	6	3.6	7	1.1
0.64722	12.2	22	2	4	3.3	14	3.5	1	1.8	1	1.6
0.70717	10.1	5	4	1	1.8	1	2	17	1.4	1	0.9
0.74397	14.2	6	3	2	3.3	1	2.2	16	2.2	1	3.5
0.69542	15.3	23	1.5	4	3.8	7	3.1	7	3.8	2	3.1
0.82861	15	10	1.6	7	8	6	2	2	1.5	5	1.9
0.51822	12.6	7	3.5	4	3.3	4	2.3	5	1.6	7	1.9
0.87324	16.3	8	2.1	5	8	6	3.4	5	0.9	4	1.9
0.76787	17	3	7.8	6	1.8	7	1.8	2	3.6	5	2
0.91430	19.2	8	1.9	5	8.5	7	3.4	1	2.4	7	3
0.77772	16.9	3	7.9	6	3.9	6	1.8	1	2.3	7	1
0.49346	12.7	12	2.9	2	1.9	7	4	6	1.9	5	2
0.69550	14.5	9	2.9	1	3.2	4	1.8	1	2.9	14	3.7
0.68912	18.6	3	7	6	3.8	6	1.9	7	3.1	1	2.8
0.98692	22.2	23	3.9	7	1.4	1	1.8	6	8.2	6	6.9

Table A.6

A set of starting individuals from a stochastic approach for grinding schedules with 5 steps

Max. Damage	Total LU	Crack depth (mm)	Individuals (LU | mm)										
0.85562	13.9	7	1.2	1	0.7	1	5.5	1	1.2	2	2.2	15	3.1
0.70458	11.9	6	0.9	2	1.2	1	5.4	4	1	11	1.2	2	2.2
0.98351	16.8	4	2.5	1	7.6	5	1.1	5	3.1	4	1.2	5	1.3
0.85648	20.6	3	8.7	5	1.7	3	0.9	1	1.2	6	0.7	5	7.4
0.67015	12.7	17	2.8	11	5.6	2	0.8	1	0.7	1	1.6	5	1.2
0.56034	10.4	17	3	5	0.7	6	1.6	2	2.9	1	1.4	6	0.8
0.80996	14.8	23	1.8	4	1.4	10	2.5	1	2.3	1	1.1	4	5.7
0.91582	15.1	23	2.3	2	1.4	1	1.5	13	1.4	3	1	1	7.5
0.85074	15.9	19	1.6	6	1.6	3	1.2	5	1.5	2	6.8	4	3.2
0.43903	10.8	23	0.9	4	3.1	3	1.6	6	1.3	6	1.2	1	2.7
0.79593	14.7	22	3	2	2.8	15	3.2	1	2.6	1	1.5	1	1.6
0.94596	22	23	2.6	1	5.6	1	1.3	4	3.2	13	1.1	1	8.2
0.98712	22.9	18	8.2	5	1.5	1	0.7	5	5.5	4	6.2	5	0.8
0.93357	20.3	23	1.9	3	1.3	6	1.4	1	2.9	4	6	6	6.8
0.82666	16.6	10	0.7	3	2.6	4	6.8	6	3.3	1	1.1	6	2.1
0.71865	14.4	3	7.3	5	0.9	1	1.6	5	1.6	3	1.6	6	1.4
0.79304	15.2	10	0.9	6	1.8	1	6.1	4	2	6	1.4	3	3
0.80780	17.6	12	3.1	2	1.5	1	2.6	6	6.4	5	1.7	6	2.3
0.44891	10.9	13	1.7	1	2.5	5	1	4	3.3	4	1.1	6	1.3
0.95253	17.5	18	2.7	13	1.6	1	5.9	1	2.4	4	1.7	1	3.2

Table A.7

A set of starting individuals from a stochastic approach for grinding schedules with 8 steps

Max. Damage	Total LU	Crack depth (mm)	Individuals (LU | mm)									
0.90907	24.7	22	4	4	4.5	3	1	2	0.7	1	4.8	3
			1.6	3	1.1	3	5.4	1	1.6			
0.84327	13.7	8	1	1	1.8	1	1.2	1	4.3	1	0.5	1
			0.6	1	2	13	1.4	1	0.9			
0.81788	17	7	1.6	1	6.7	3	1.2	1	1.9	2	1.9	2
			1.2	8	0.5	1	1.1	2	0.9			
0.70794	14	16	1.5	2	0.9	1	0.8	1	1.7	4	0.5	1
			1.5	4	5.5	4	1	3	0.6			
0.75053	14.7	15	1.8	1	0.5	1	0.5	4	1.2	1	0.7	1
			1.6	4	5.7	4	1.7	4	1			
0.88855	18.2	13	0.9	4	4.6	3	0.5	3	7	3	1.1	1
			1	4	1.2	1	0.6	1	1.3			
0.99983	29.1	4	1	1	9.2	8	6.3	1	0.9	4	3.9	1
			1	3	0.6	1	0.7	1	5.5			
0.57535	12.3	8	1.6	2	1.7	1	1.3	2	2.1	1	1	9
			1.6	1	0.8	2	1.6	2	0.6			
0.79823	16.8	22	1.6	2	4.7	1	0.8	10	0.9	1	1	1
			0.6	3	2	1	4.1	1	1.1			
0.68148	15.7	23	2	3	0.6	4	0.9	1	0.7	1	0.9	1
			1.5	4	3.6	3	1.1	3	4.4			
0.94949	19.5	23	3.4	1	1.5	1	0.6	3	0.6	8	3.5	2
			2	3	1	1	0.9	1	6			
0.88462	22.8	15	1.3	1	6.8	4	0.5	1	4	3	1	3
			5.8	4	1.3	3	0.6	1	1.5			
0.71295	11.8	20	0.7	9	1	2	0.6	1	0.9	1	1	3
			3.6	1	1.1	1	1.6	2	1.3			
0.94960	20.3	18	0.9	4	1.8	4	6.6	3	1.1	2	1.4	1
			0.9	1	4.9	4	0.8	1	1.9			
0.52739	12.3	21	1.2	1	0.9	3	1.1	1	1.2	9	4.8	3
			0.6	1	1.2	1	0.7	1	0.6			
0.90214	18.9	23	5	1	0.5	1	0.7	1	1.7	1	1	4
			0.9	10	0.9	1	1.1	1	7.1			
0.81703	14	7	1.3	1	5.2	1	0.8	1	0.7	1	1	1
			1.9	1	0.5	1	0.6	13	2			
0.79796	14.2	20	1.6	1	1	1	1.5	3	0.8	9	0.6	1
			1.5	1	1.6	1	4.6	3	1			
0.98758	16.6	20	0.9	4	1.1	1	2	1	0.9	7	0.9	1
			1.3	2	1.2	1	7	3	1.3			
0.99822	15.1	22	1	1	0.9	13	1.9	1	3.4	1	0.9	1
			0.9	1	1	1	4.6	1	0.5			

Table A.8

A set of starting individuals from a stochastic approach for grinding schedules with 10 steps

Max. Damage	Total LU	Crack depth (mm)	Individuals (LU | mm)										
0.65591	16.5	21	0.8	1	5	3	0.8	3	1.7	2	0.8	3	
			0.6	2	0.5	1	0.5	2	1.6	1	3.6	2	0.6
0.62632	15.8	22	4.9	1	0.9	10	0.5	1	0.9	1	1	2	
			3	1	0.5	1	1.4	1	0.6	1	0.6	1	1.5
0.76273	15.2	23	1	1	1.4	3	1.1	1	0.7	3	0.5	3	
			1.6	1	0.8	2	0.6	2	0.7	1	0.8	3	6
0.63252	12.8	8	0.7	1	0.9	1	0.8	1	1.6	1	0.7	1	
			3	10	1.6	2	0.7	1	0.7	1	1.3	1	0.8
0.98490	26.6	12	7.5	6	1.3	1	0.7	1	0.4	1	6.3	1	
			0.6	2	1.3	3	0.9	1	4.8	3	1.3	1	1.5
0.89024	18.1	14	0.4	3	0.6	1	4.5	3	0.7	2	0.7	1	
			1	1	4.9	1	1.1	6	2.8	1	0.8	1	0.6
0.97164	20.4	8	0.9	3	5.2	1	0.5	1	4.4	2	0.8	1	
			0.8	1	1	1	1.3	1	0.5	8	4.1	1	0.9
0.95727	25.9	23	3.5	1	4.6	1	1.4	1	0.8	3	0.7	1	
			1.2	2	0.8	6	6.2	3	0.7	1	1.6	1	4.4
0.90445	19.7	8	0.8	1	3.4	1	0.8	1	0.8	1	1.2	1	
			4.5	6	1.2	6	1.3	1	0.6	1	1.2	1	3.9
0.72893	16.9	13	0.4	1	0.6	2	1	1	3.6	1	0.4	2	
			0.8	1	1.3	2	3.2	1	0.8	1	0.6	8	4.2
0.88433	22.9	11	0.7	2	0.7	1	6.6	3	0.8	2	4.5	1	
			0.7	3	0.6	1	0.7	3	0.6	1	5.5	3	1.5
0.88348	16.3	6	0.6	1	1.4	1	6.1	1	0.7	1	0.9	10	
			2.7	1	0.6	2	1.4	1	0.7	1	0.6	1	0.6
0.71699	16.8	20	1	5	4.4	2	0.7	1	0.5	1	1.1	2	
			0.4	2	0.9	1	1.5	3	4.3	1	0.4	2	1.6
0.99569	24.1	9	0.7	1	4.8	1	2.9	2	0.4	1	1.4	1	
			3.8	1	0.8	2	0.5	9	5.6	1	1.6	1	1.6
0.81441	21.9	13	3.7	3	0.7	1	4.8	6	5.1	1	1.1	2	
			0.5	1	1.6	1	1	3	1.5	1	0.4	1	1.5
0.56580	14.5	14	3.7	3	1.4	1	0.6	3	0.7	1	1.5	3	
			3.3	2	0.4	3	0.6	1	0.6	2	0.9	1	0.8
0.87648	23.4	23	5.2	1	0.4	1	1.3	1	1.1	2	1.6	1	
			0.5	7	0.7	1	5.6	3	0.9	1	1.1	2	5
0.80882	18.5	22	1.2	1	0.8	3	1.6	7	4.9	1	1.2	1	
			1.5	2	1.5	2	0.9	1	0.9	1	2.9	1	1.1
0.67553	16.7	23	2.7	2	1.2	1	0.7	1	0.8	3	1.6	2	
			0.5	3	0.7	2	1.6	1	1.6	3	0.8	2	4.5
0.93511	21.5	11	0.5	1	1.7	3	6	1	0.8	1	0.7	2	
			4.1	2	1.5	3	4	3	0.7	1	0.8	3	0.7

Table A.9

A set of starting individuals from a stochastic approach for grinding schedules with 15 steps

Max. Damage	Total LU	Crack depth (mm)	Individuals (LU | mm)										
0.87840	23.7	22	0.5	1	5.1	1	0.5	1	1.1	2	0.5	1	
			1.1	1	0.4	1	2	2	0.5	2	0.3	1	
			0.5	1	3.7	1	2	2	0.8	2	4.1	1	0.6
0.76119	18.8	17	3.8	1	0.5	1	0.7	2	0.8	5	0.9	1	
			0.3	1	0.3	1	3.1	1	1	1	2.2	1	
			0.8	1	0.3	1	0.3	1	0.8	1	2.4	1	0.6
0.93287	20	8	3.8	1	0.5	1	3.4	1	0.3	1	0.8	1	
			3.7	1	0.3	1	0.8	1	0.4	1	0.6	6	
			0.9	1	0.5	1	0.5	1	2.2	1	0.7	1	0.6
0.97875	25.3	23	0.3	1	4.6	1	0.5	5	0.5	1	0.6	1	
			4	1	2.3	1	0.3	1	1	2	0.7	1	
			0.4	1	3.9	1	0.5	1	0.4	1	0.9	1	4.4
0.78341	18.2	15	1	1	0.5	2	3.4	1	0.4	1	0.5	1	
			0.3	1	0.5	1	4.3	2	0.9	1	1.1	1	
			0.9	1	1.9	2	0.3	2	0.7	2	0.8	1	0.7
0.89256	20	7	0.4	1	3.5	1	0.8	2	4.1	1	2.2	2	
			0.3	1	0.4	1	0.3	1	0.6	1	0.4	1	
			0.5	2	0.9	2	3.8	2	0.9	1	0.5	1	0.4
0.72374	17.5	8	0.6	2	3.5	1	0.9	1	0.9	1	2.8	2	
			0.8	1	0.9	1	0.6	1	1.9	1	0.3	2	
			0.8	2	0.7	2	0.7	1	0.4	1	0.8	1	0.9
0.91224	22.8	6	3.5	1	2.5	2	3.8	1	1.1	1	0.4	2	
			0.6	1	0.5	1	4.2	1	0.7	1	0.5	2	
			1.1	2	0.7	1	0.9	1	0.4	1	0.9	2	1
0.93838	24.8	10	0.5	1	2.8	1	3.9	1	0.5	1	0.3	1	
			3.4	2	0.5	1	3.8	2	0.4	1	2.6	1	
			0.9	2	0.5	1	0.8	1	3	2	0.3	2	0.6
0.81000	21.9	18	1	1	2.7	1	2.7	1	0.5	2	3.1	2	
			0.5	2	3.5	1	0.3	1	0.4	2	0.3	1	
			0.6	1	4.3	1	0.5	1	0.6	1	0.4	2	0.5
0.99818	27.1	13	3.4	2	0.8	1	4.1	1	0.6	1	1.1	1	
			3	1	0.3	1	0.8	2	4.3	1	1	2	
			0.7	2	0.6	1	0.9	1	1.1	2	0.5	1	3.9
0.83303	19.3	4	3.4	1	4.8	1	0.4	1	0.5	2	0.8	1	
			0.6	1	0.5	2	0.5	1	0.7	4	0.4	1	
			3	1	0.3	1	0.8	1	0.9	1	1.1	1	0.6
0.87329	23.2	22	0.5	1	0.3	2	0.4	1	4.4	1	0.7	1	
			0.8	1	0.6	2	1.1	2	0.9	1	3.7	1	
			0.6	1	2.1	2	0.6	2	2	1	1	1	3.5
0.92164	22.9	15	0.4	2	0.8	1	3.4	1	0.4	2	0.3	1	
			0.6	1	0.6	2	4.8	1	0.6	1	2.4	1	
			0.9	2	0.7	2	3.3	1	0.6	1	1	1	2.1

Table A.9

Continued

Max. Damage	Total LU	Crack depth (mm)	Individuals (LU | mm)										
0.80269	19.7	22	0.3	1	0.4	1	0.7	2	2.9	1	0.4	1	
			0.6	1	0.5	1	0.9	1	0.6	1	0.6	2	
			2.9	2	2.2	2	0.4	1	0.5	1	3.2	2	2.6
0.83609	25.3	19	3.4	1	0.8	1	3.6	1	0.6	2	0.6	1	
			0.5	2	3	1	0.4	1	3.2	2	0.5	1	
			0.5	2	0.5	1	4.5	1	0.6	2	0.7	1	1.9
0.98169	24.3	21	0.8	1	1.1	1	0.4	2	5.7	1	0.4	1	
			0.4	1	0.3	1	0.8	2	3.1	2	0.5	1	
			0.5	1	3.5	1	0.5	1	0.8	2	5.2	2	0.3
0.78983	19.4	16	0.6	2	0.6	1	3.2	2	0.8	1	0.5	1	
			0.5	1	2.1	1	0.4	2	0.4	1	3.9	1	
			0.8	1	1	1	0.3	2	0.5	2	3	1	0.8
0.99596	27.4	11	0.6	1	4.3	1	1.1	1	4	1	0.3	1	
			1.1	1	0.5	2	5.2	2	0.6	1	0.4	1	
			0.4	2	4.2	2	0.5	1	1	1	2.7	2	0.5
0.82152	18.3	21	0.9	1	0.5	1	0.8	2	2.8	1	0.8	1	
			0.4	1	0.3	1	0.3	1	0.7	1	0.5	2	
			2	1	0.6	1	0.4	2	2.5	2	4.3	2	0.5

Table A.10

A set of starting individuals from a stochastic approach for grinding schedules with 20 steps

Max. Damage	Total LU	Crack depth (mm)	Individuals (LU | mm)										
0.67039	15.6	20	0.6	1	0.4	1	0.4	1	0.7	1	0.2	1	
			0.2	1	0.5	1	0.8	1	0.5	1	0.9	1	
			2.2	1	0.3	1	0.2	1	2.2	1	0.8	1	
			0.7	1	1.4	1	0.3	1	1.7	1	0.3	1	0.3
0.99590	26.2	17	2.1	1	0.7	1	2	1	3.1	1	0.3	1	
			0.5	1	0.2	1	0.3	1	1.4	1	0.3	1	
			0.5	1	2	1	0.4	1	3.3	1	2.5	1	
			0.7	1	0.7	1	0.5	1	0.2	1	0.2	1	4.3
0.93269	23.7	21	0.5	1	1.4	1	0.2	1	0.5	1	2.3	1	
			0.5	1	2.6	1	0.8	1	0.3	1	2	1	
			0.3	1	0.7	1	1.9	1	1.6	1	0.4	1	
			0.3	1	0.4	1	4	1	0.3	1	2.3	1	0.4
0.72551	17.4	23	0.4	1	0.8	1	0.5	1	0.3	1	0.3	1	
			2.7	1	1.9	1	0.2	1	0.4	1	0.3	1	
			0.6	1	0.5	1	0.4	1	0.5	1	0.7	1	
			0.4	1	0.3	1	0.4	1	0.3	1	1.8	1	3.7
0.98582	25.9	16	2.5	1	1.5	1	0.7	1	0.4	1	0.4	1	
			3	1	2.8	1	1.8	1	0.3	1	0.9	1	
			0.6	1	2.7	1	0.3	1	1.6	1	2.8	1	
			0.3	1	0.2	1	1.8	1	0.9	1	0.2	1	0.2
0.97479	24.7	17	0.4	1	0.3	1	2.8	1	1.6	1	0.4	1	
			0.4	1	0.4	1	0.8	1	2.5	1	0.4	1	
			2	1	1.5	1	0.3	1	3.1	1	0.5	1	
			2.4	1	0.4	1	0.3	1	1.8	1	0.4	1	2
0.79403	20.8	9	4.6	1	0.3	1	2.8	1	0.7	1	0.3	1	
			0.4	1	3	1	0.8	1	0.2	1	0.4	1	
			0.4	1	0.3	1	0.4	1	0.7	1	0.6	1	
			2.3	1	0.2	1	0.5	1	0.8	1	0.8	1	0.3
0.99355	29.7	21	2.3	1	3.2	1	2.6	1	0.7	1	1.8	1	
			2.3	1	0.4	1	0.4	1	0.4	1	0.5	1	
			2.4	1	0.3	1	0.4	1	0.5	1	3.2	1	
			2.3	1	0.3	1	0.7	1	1.8	1	2.8	1	0.4
0.77909	22	13	0.3	1	4	1	0.4	1	0.7	1	0.2	1	
			3	1	1.6	1	0.6	1	0.3	1	0.4	1	
			3.1	1	0.4	1	0.4	1	0.7	1	0.4	1	
			0.4	1	1.8	1	0.3	1	0.3	1	2.5	1	0.2
0.92854	28.2	12	2.7	1	0.3	1	2.9	1	1.4	1	0.6	1	
			2.3	1	0.4	1	0.7	1	2.4	1	1.4	1	
			1.8	1	0.3	1	0.4	1	2.1	1	1.7	1	
			0.9	1	0.8	1	0.4	1	0.4	1	0.5	1	3.8

Table A.10

Continued

Max. Damage	Total LU	Crack depth (mm)	Individuals (LU | mm)										
0.70810	15	11	1.4	1	0.3	1	0.5	1	0.2	1	0.7	1	
			2	1	3.2	1	0.4	1	0.3	1	1.6	1	
			0.6	1	0.3	1	0.2	1	0.7	1	0.5	1	
			0.3	1	0.5	1	0.5	1	0.3	1	0.2	1	0.3
0.91688	24.4	21	0.4	1	0.8	1	3.2	1	0.6	1	1.6	1	
			0.4	1	0.6	1	0.3	1	3.2	1	0.3	1	
			2.7	1	0.5	1	0.8	1	0.3	1	1.4	1	
			0.3	1	0.5	1	3.2	1	2.3	1	0.3	1	0.7
0.85868	23	15	2.1	1	0.6	1	0.4	1	0.8	1	3.1	1	
			0.2	1	0.3	1	0.7	1	2.7	1	0.3	1	
			0.3	1	3	1	0.2	1	2.5	1	0.3	1	
			0.3	1	0.8	1	0.4	1	3.1	1	0.6	1	0.3
0.95397	24.5	8	0.2	1	2.6	1	0.7	1	0.3	1	0.5	1	
			6.3	1	0.8	1	0.3	1	0.3	1	0.6	1	
			0.7	1	0.8	1	3.2	1	0.4	1	0.3	1	
			1.4	1	0.7	1	0.8	1	0.5	1	0.4	1	2.7
0.92380	22.1	14	0.4	1	0.8	1	0.4	1	1.8	1	0.8	1	
			1.4	1	2.1	1	0.5	1	2.6	1	0.7	1	
			1.9	1	0.4	1	2.8	1	0.3	1	0.3	1	
			0.5	1	0.5	1	0.6	1	0.2	1	2.6	1	0.5
0.85189	21.5	8	0.3	1	3.2	1	0.6	1	0.4	1	3.1	1	
			2.6	1	0.3	1	0.4	1	0.4	1	0.6	1	
			0.3	1	0.6	1	0.9	1	0.8	1	0.8	1	
			3.6	1	0.5	1	0.7	1	0.3	1	0.4	1	0.7
0.62529	18.2	15	3.1	1	0.4	1	0.2	1	2.1	1	0.3	1	
			0.4	1	0.7	1	0.5	1	1.8	1	0.3	1	
			0.3	1	1.8	1	0.5	1	1.4	1	0.5	1	
			0.3	1	0.4	1	2.2	1	0.4	1	0.3	1	0.3
0.91837	20.9	17	0.2	1	0.3	1	0.4	1	0.4	1	2.1	1	
			2.6	1	0.8	1	1.6	1	0.4	1	0.7	1	
			1.5	1	0.4	1	0.7	1	2.4	1	2.9	1	
			0.3	1	0.5	1	1.7	1	0.3	1	0.3	1	0.4
0.82672	19.6	18	0.7	1	0.8	1	0.4	1	0.4	1	0.8	1	
			0.4	1	1.7	1	0.6	1	0.6	1	1.8	1	
			0.8	1	0.7	1	0.7	1	0.4	1	0.6	1	
			4.4	1	0.3	1	0.4	1	0.5	1	2.2	1	0.4
0.64307	19.6	7	2.5	1	1.5	1	2	1	0.8	1	0.4	1	
			1.4	1	0.6	1	0.3	1	1.8	1	0.4	1	
			0.7	1	0.8	1	0.2	1	0.5	1	0.4	1	
			0.3	1	2	1	0.3	1	2.1	1	0.2	1	0.4

APPENDIX C

OPTIMIZATION PARAMETERS

Parameters used in the first step of optimization with genetic algorithm (GA)

Probability of mutating LU	= 50%
Probability of mutating grinding thickness	= 50%
Minimum improvement rate	= 0.3%
Allowable mutation for each evolution	= 30
LU mutation mode	= linearly random
Number of LU components to be mutated	= 2 - 11
LU mutation rate	= 10 – 100%
Grinding thickness mutation mode	= linearly random
Number of grinding thickness components to be mutated	= 2 – 4
Grinding thickness mutation rate	= [1 2 3 4] mm
Number of mutations allowed without improvement	= 50

Parameters used in the optimization local search using genetic algorithm (GA)

Probability of mutating LU	= 50%
Probability of mutating grinding thickness	= 50%
Minimum improvement	= 1 LU
Allowable mutation for each evolution	= 30
LU mutation mode	= linearly random

Number of LU components to be mutated	= 1
LU mutation step	= 0.1 LU
Grinding thickness mutation mode	= linearly random
Number of grinding thickness components to be mutated	= 2
Grinding thickness mutation rate	= 1 mm
Number of mutations allowed without improvement	= 50

VITA

Potchara Tangtragulwong was born in Bangkok, Thailand. He graduated from Wat Nuan Noradit School in May 1998. He received his B.Eng. degree in Mechanical Engineering from Chulalongkorn University, Bangkok, Thailand in 2002. After graduation, he spent fifteen months working as a production/industrialization engineer with Michelin, Thailand.

He continued his graduate studies at Texas A&M University and received his M.Eng. degree in Mechanical Engineering in 2006. He earned a Ph.D. degree in Civil Engineering at Texas A&M University in 2010. He may be reached through Dr. Gary Fry, Zachry Department of Civil Engineering, Texas A&M University, College Station, TX, 77843. His email address is potchara_t@yahoo.com.